Freie Universität Berlin

Detection and analysis of seismicity in the Eastern Alps using waveform based methods

Dissertation
zur Erlangung des Grades eines
Doktors der Naturwissenschaften
(doctor rerum naturalium)

am Fachbereich Geowissenschaften
der Freie Universität Berlin

Vorgelegt von:
Laurens Jan Hofman

Berlin 2024

Erstgutachter: Prof. Dr. Serge A. Shapiro
Zweitgutachter: Prof. Dr. Frederik Tilmann

Tag der Disputation: 29. November 2024

Ich erkläre hiermit an Eides statt, dass ich die vorliegende Dissertation selbstständig und nur unter Verwendung der angegebenen Quellen und Hilfsmittel angefertigt habe.

Berlin, 5. September 2024

It is not the mountain we conquer, but ourselves.

— Sir Edmund Hillary

Abstract

The Eastern Alps are subject to routine seismic monitoring by several national and regional agencies. However, the station density of the permanent local networks varies significantly, which has hindered the development of a high-resolution uniformly processed regional earthquake catalogue. The recent deployment of the temporary AlpArray Swath-D network has provided unparalleled station coverage for a two-year period, creating a unique opportunity for the detailed analysis of the seismicity of the Eastern Alps.

By utilising data from this network, I established a highly effective workflow for the detection, phase-picking, and localisation of low-magnitude seismicity using waveform based methods. This unique workflow yielded a high-resolution regional earthquake catalogue comprising $6,053$ events and a completeness magnitude of M_L -1.0. It is contingent on an efficient template matching code, which enabled me to integrate and expand upon existing earthquake catalogues from the well-established regional networks. Innovative picking methods were applied to automatically pick phase-arrivals based on a selection of manually picked events. These were then used to accurately localise the events within a recent local 3D velocity model. As a consequence of the high population density and industrialisation of the Eastern Alps, a considerable amount of anthropogenic signals are recorded continually in conjunction with the seismic events. I identified these signals with high confidence through the analysis of temporal signatures and satellite imagery. This is essential for an accurate interpretation of the spatial and temporal distribution of the earthquakes in the catalogue.

The obtained distribution of the earthquakes is largely consistent with known deformation patterns in the region observed through long-term seismic monitoring. A systematic variation of the b-values of the frequency-magnitude distribution indicates high differential stress in the area where previous GPS studies have identified the highest crustal deformation rates, and low differential stress in an area that is characterised by high uplift rates. To further expand the analysis of small-magnitude seismicity clusters, I applied techniques derived from graph theory. This enabled me to differentiate closely located earthquakes into sub-clusters associated with distinct faults. The relative relocalisation of events based on S-P differential travel-time inversion then allowed me to resolve the orientations of these faults, which exhibit a close correlation to fault plane solutions for moment tensor inversions of individual events within these sub-clusters.

The methodology that I present in this thesis has been demonstrated to be very effective for the detection of small earthquakes in low signal-to-noise recordings, resulting in an unprecedented image of the seismicity in the Eastern Alps over the two-year recording period of the AlpArray Swath-D network.

Zusammenfassung

Die Ostalpen werden von verschiedenen nationalen und regionalen Institutionen routinemäßig seismisch überwacht. Die Stationsdichte der permanenten, lokalen Netzwerke ist jedoch sehr variabel. Dies erschwert die Erstellung eines hochauflösenden, einheitlich verarbeiteten regionalen Erdbebenkatalogs. Durch die Installation des temporären AlpArray Swath-D Netzwerks wurde eine einzigartige Stationsabdeckung für einen Zeitraum von zwei Jahren geschaffen. Dies ermöglicht eine detaillierte Analyse der Seismizität der Ostalpen.

Unter Verwendung der Daten dieses Netzwerks habe ich einen hocheffektiven Arbeitsablauf für die Detektion, die Identifikation seismischer Phasen und die Lokalisierung von Seismizität niedriger Magnitude mittels wellenformbasierter Methoden entwickelt. Dieser einzigartige Arbeitsablauf resultierte in einem hochauflösenden regionalen Erdbebenkatalog mit 6.053 Ereignissen und einer Vollständigkeitsmagnitude von $M_L - 1,0$. Er basiert auf einem effizienten *Template Matching* Algorithmus. Dieser ermöglichte es mir, bestehende Erdbebenkataloge aus den etablierten regionalen Netzwerken zu integrieren und zu erweitern. Es wurden innovative Methoden angewandt, um auf der Grundlage einer Auswahl von manuell identifizierten Phasen automatisch neue Phasenankünfte zu ermitteln. Diese wurden daraufhin verwendet, um die Ereignisse innerhalb eines aktuellen lokalen 3D-Geschwindigkeitsmodells genau zu lokalisieren. Infolge der hohen Bevölkerungsdichte sowie der Industrialisierung der Ostalpen werden neben seismischen Ereignissen viele anthropogene Signale aufgezeichnet. Durch die Analyse von zeitlichen Signaturen und Satellitenbildern habe ich diese mit hoher Sicherheit identifiziert. Dieser Schritt ist eine wichtige Voraussetzung für die richtige Interpretation der räumlichen und zeitlichen Verteilung der Erdbeben im Katalog.

Die ermittelte Verteilung der Erdbeben stimmt weitgehend überein mit bekannten Deformationsmustern in der Region, die durch langfristige seismische Überwachung beobachtet wurden. Eine systematische Variation der b-Werte der Magnituden-Häufigskeitsverteilung deutet auf eine hohe differentielle Spannung in dem Gebiet hin, in dem frühere GPS-Studien die höchsten Krustenverformungsraten festgestellt haben. In einem Gebiet, das durch hohe Hebungsraten charakterisiert ist, deutet sie dahingegen auf eine geringe differentielle Spannung hin. Um die Analyse von Seismizitätsclustern geringer Magnitude weiter auszubauen, habe ich Methoden aus der Graphentheorie angewandt. Diese ermöglichten es mir, nah beieinander liegende Erdbeben in Untergruppen zu unterteilen, die mit bestimmten Verwerfungen assoziiert werden können. Die relative Relokalisierung von Ereignissen auf Grundlage der differentiellen S-P Laufzeitinversion ermöglichte es mir schließlich, die Orientierungen dieser Verwerfungen zu bestimmen. Die Resultate zeigen eine sehr gute Übereinstimmung mit den Lösungen der Momententensorinversionen einzelner Ereignisse innerhalb dieser Untergruppen.

Die Methodik, die ich in dieser Arbeit vorstelle, hat sich als sehr effektiv für die Erkennung kleiner Erdbeben in Aufzeichnungen mit geringem Signal-Rausch-Verhältnis erwiesen. Das Resultat ist ein bislang einzigartiges Bild der Seismizität in den Ostalpen während der zweijährigen Aufzeichnungszeit des AlpArray Swath-D Netzwerks.

Contents

1 Introduction **1**
- 1.1 Tectonic setting 1
- 1.2 Recent geophysical studies 3
- 1.3 Historical and instrumental seismicity 3
- 1.4 Motivation and outline 6

2 The AlpArray initiative **7**
- 2.1 The AlpArray backbone network 7
- 2.2 The AlpArray Swath-D network 8

3 Waveform based methods **13**
- 3.1 Template matching 14
- 3.2 Semi automated phase-picking 25
- 3.3 Event localisation 32

4 Event classification **37**
- 4.1 Classification based on waveform attributes 38
- 4.2 Spatio-temporal event classification 40

5 Event magnitudes **45**
- 5.1 Introduction 45
- 5.2 Calculation of local magnitudes 46
- 5.3 Magnitude frequency distribution and scaling with M_w 48

6 A seismicity catalogue for the Eastern Alps **51**
- 6.1 Spatial and temporal patterns in seismicity 51
- 6.2 Spatial variation of the b-value 59

6.3 Sensitivity of template matching to low-magnitude seismicity . . . 63

7 Analysis of seismicity clusters . . . 65
7.1 Application of Graph Theory . . . 66
7.2 High precision relative relocalisation . . . 69
7.3 Spatio-temporal analysis of clustered seismicity . . . 76

8 Conclusions . . . 93

9 Outlook . . . 95

Appendices . . . 97
A Additional figures and data . . . 97
B: Fitting the GR to the FMD . . . 123

Bibliography . . . 125

Acknowledgements . . . 139

Curriculum Vitae . . . 141

Publications and Conference Abstracts . . . 145

CHAPTER 1

Introduction

1.1 Tectonic setting

The European Alps are embedded within the Alpine-Himalayan orogenic belt, which extends from the Atlas Mountains in the west to the Himalayas in the east. Mountain building started with the opening of the Atlantic Ocean during the Mesozoic Era after the breakup of the supercontinent Pangaea. The northward motion of the African, Arabian, and Indian plates relative to the Eurasian plate facilitated the closure of the Tethys Ocean, as well as the formation of mountain chains along the convergent plate interfaces. The existence of numerous microcontinents situated between the larger plates caused the Tethys Ocean to be divided into multiple oceanic basins. Continental crust from these microcontinents was subsequently accreted onto the overriding plate during subduction of the oceanic lithosphere. The more rigid crustal parts obstructed the north-south compression of the larger plates, resulting in the formation of a complex network of compressional, extensional, and transform plate interfaces (Dewey et al., 1973).

In the Alps, the prevailing tectonic setting is largely controlled by the Adriatic microplate, which exhibits a counter-clockwise rotation as it has been thrust northward onto the Eurasian plate by Africa for the last 35 Ma (Handy, Schmid, et al., 2010). As illustrated in the simplified tectonic map in Figure 1.1, there is a notable difference between the geologic units of the Western and Eastern Alps.

In contrast to the Western Alps, which are predominantly composed of accreted European crust and oceanic crust, the Eastern Alps are characterised by units of Adriatic origin (Schmid, Fügenschuh, et al., 2004). East of the transition between these two regimes, which happens at about $10°15'E$ longitude, parts of the underlying European plate are found mainly in two windows: the Engadine Window and the Tauern Window. A large system of right lateral strike-slip faults, collectively called the Periadriatic Line, crosses the central part of the Alps. It is offset by the Giudicarie Line at around $11°E$ longitude. This line marks the western and northern boundary of the Adriatic indenter – a rigid part of the Adriatic microplate that shows little internal deformation. At its western boundary, the Adriatic indenter caused NWN-driven thrust faulting, whereas in the Eastern Alps, north-south convergence was compensated by continental escape towards the east (Ratschbacher et al., 1989).

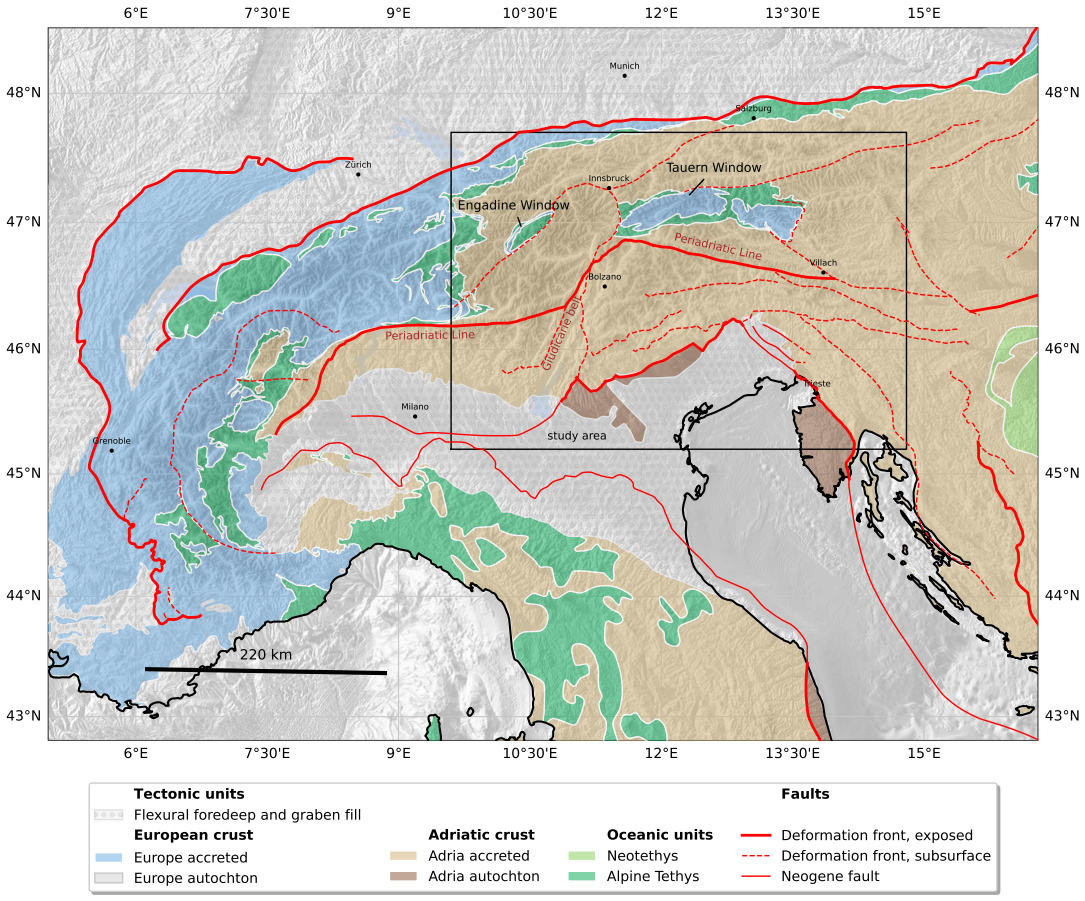

Figure 1.1. Simplified tectonic map of the Alps showing the tectonic units grouped by their origin, and the major Alpine faults. The tectonic units and lineaments in this map were compiled by M.R. Handy and are based on maps in Schmid, Fügenschuh, et al. (2004), Schmid, Bernoulli, et al. (2008), Handy, Schmid, et al. (2010), Handy, Ustaszewski, et al. (2015), Handy, Giese, et al. (2019), Bigi et al. (1990), Froitzheim et al. (1996), and Bousquet et al. (2012).

1.2 Recent geophysical studies

Several large scale geological-geophysical studies have been conducted along transects throughout the Alps. From west to east, these include CIFALPS (Malusà et al., 2021); ECORS-CROP (Nicolas, Hirn, et al., 1990); NFP-20 (west and east) (Pfiffner et al., 1990); TRANSALP (TRANSALP Working Group et al., 2002; Schmid, Fügenschuh, et al., 2004); EASI (AlpArray Working Group, 2014); and ALP 2002 (Brückl et al., 2007). Interpretations from the transects in the Western Alps between $6°E$ and $8°E$ (ECORS-CROP; Nicolas, Hirn, et al. (1990) and NFP-20 west; Pfiffner et al. (1990)) agree on a subduction of the European lithosphere with subduction directions varying from ENE in the southern part of the Western Alps, to ESE in the northern part of the Western Alps, with backthrusting occurring within the European crust. The European Moho deepens towards the central part of the Alps, whereas the Adriatic Moho rises. In the Central and Eastern Alps (NFP-20 East ($9.3°E$); Pfiffner et al. (1990), TRANSALP ($12°E$); TRANSALP Working Group et al. (2002) and Kummerow et al. (2004)) the European Moho, and to a lesser degree the Adriatic Moho were found to be dipping towards the centre of the orogen. Conclusions from studies based on the EASI transect further east ($13.3°E$) vary from a northward subducting Adriatic crust (Hetényi, Plomerová, et al., 2018) to a southwards subducting European crust (Mroczek et al., 2023), to indecisive (Bianchi et al., 2021). The complexity of the crustal structure beneath the Eastern Alps is also revealed by the variation in results from local, teleseismic, and ambient-noise tomography studies (e.g. Piromallo and Morelli, 2003; Lippitsch et al., 2003; Bleibinhaus and Gebrande, 2006; Diehl et al., 2009; Zhao et al., 2015; Hua et al., 2017; Kissling and Schlunegger, 2018; Kästle, El-Sharkawy, et al., 2018; Kästle, Rosenberg, et al., 2020; Lu et al., 2020; Qorbani et al., 2020; Nouibat et al., 2021; Paffrath et al., 2021; Jozi Najafabadi, Haberland, Le Breton, et al., 2022; Paul, 2022). Ongoing discussions surround the suggestion of a gap between the European and Adriatic Moho (Bleibinhaus and Gebrande, 2006; Spada et al., 2013; Mroczek et al., 2023), and the possibility of a northwards dipping Adriatic crust beneath the Eastern Alps, which would imply a switch in the subduction polarity. These controversies arise mainly from differences between receiver function studies and seismic tomography (Lippitsch et al., 2003; Schmid, Fügenschuh, et al., 2004; Handy, Schmid, et al., 2010; Mitterbauer et al., 2011; Hetényi, Plomerová, et al., 2018; Mroczek et al., 2023).

1.3 Historical and instrumental seismicity

The Friuli area, located at the north-eastern tip of the Adriatic indenter, is seismically the most active region of the Alps (e.g. Slejko, 2018; Rovida et al., 2022;

Grünthal and Wahlström, 2012). The apex of the seismicity coincides with the transition from a system of ENE-WSW striking thrust faults (i.e. the Montello-Friuli thrust belt), to a system of NW-SE trending dextral stike-slip faults in western Slovenia. A map showing the historical and instrumental seismicity in the Eastern Alps is presented in Figure 1.2. The data in this map were compiled by Rovida et al. (2022) from numerous macroseismic and instrumental catalogues. It can be observed that all major earthquakes in the Eastern Alps within the last millennium have occurred roughly on the southern border of the AlpArray Swath-D network. These include the Veronese M_w 6.5 earthquake in 1117, the Alpi Giulie M_w 6.6 earthquake in 1348 (Caracciolo et al., 2021), the 1511 M_w 6.3 earthquake on the Friulian-Slovenian border, the 1690 M_w 6.2 earthquake in Villach, the 1695 M_w 6.4 Asolana earthquake, the Alpago-Cansiglio earthquakes (M_w 6.3 in 1873 and M_w 6.1 in 1936), the 1928 M_w 6.0 earthquake in Carnia, and finally the M_w 6.4 Friuli earthquake on 6 May 1976. The 1976 earthquake was the last major earthquake in the Alps. Two strong aftershocks occurred four months later, resulting in in the loss of almost one-thousand lives and extensive structural damage to numerous villages (Slejko, 2018, and references therein). In the wake of these devastating earthquakes, awareness of the importance of seismic risk mitigation among the population and the local government was raised, and seismic networks were developed and extended (Santulin et al., 2018). Cheloni et al. (2014) estimate the maximum magnitude for an earthquake in the Eastern Alps at $M \sim 7.5$, with the recurrence time for earthquakes with magnitude $M_w > 6.7$ being larger than 1000 years.

Since the onset of routine seismic monitoring, seismicity catalogues for the Eastern Alps have been made publicly available by several national agencies (Istituto Nazionale di Oceanografia e di Geofisica Sperimentale (OGS), 2016; INGV Seismological Data Centre, 2006; Swiss Seismological Service (SED) at ETH Zurich, 1983; ZAMG-Zentralanstalt Für Meterologie Und Geodynamik, 1987). Recent studies of the seismicity of the Alps include Nicolas, Bethoux, et al. (1998), Bethoux et al. (1998), Reinecker and Lenhardt (1999), Chiarabba et al. (2005), Ustaszewski and Pfiffner (2008), Anselmi et al. (2011), Bressan et al. (2012), Viganò et al. (2015), Reiter et al. (2018), Beaucé et al. (2019), Jozi Najafabadi, Haberland, Ryberg, et al. (2021), and Saraò et al. (2021). In general, seismicity in the Eastern Alps is moderate (e.g. Slejko et al., 1998; Reiter et al., 2018), and no $M_w > 6$ earthquakes have occurred since the Friuli earthquake in 1976. Although depth estimates are usually not available for macroseismic event locations, instrumental seismicity shows that the earthquakes are strongly concentrated in the upper crust.

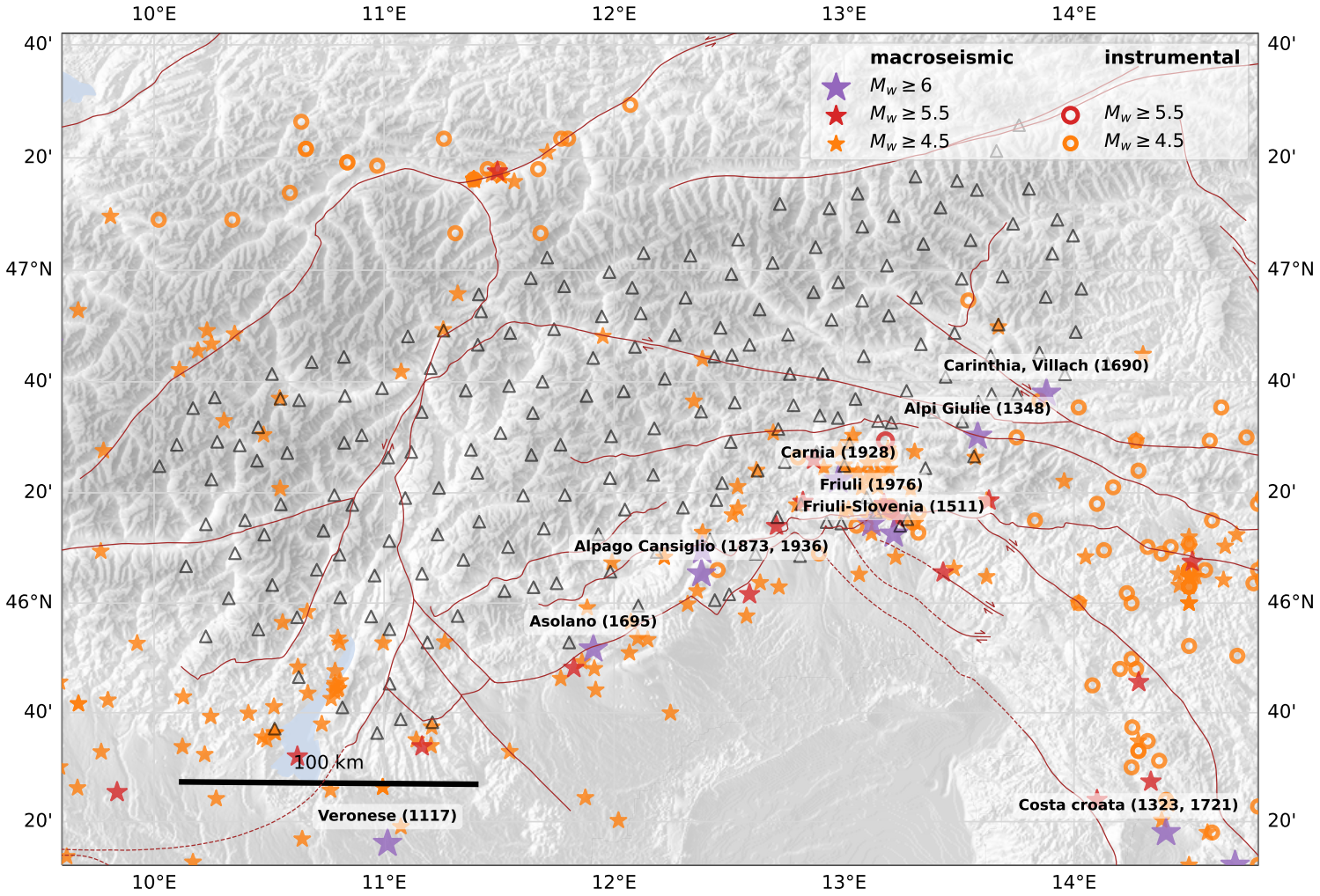

Figure 1.2. Seismicity in the Eastern Alps between 1000 - 2020 from Rovida et al. (2022). Locations derived from macroseismic data are marked as stars, instrumental seismicity is shown as circles. All events with $M_w \geq 6$ are marked with a label showing the region name and year, these locations are all derived from macroseismic data. The triangles represent seismic stations (see Chapter 2).

1.4 Motivation and outline

The analysis of the spatio-temporal distribution of seismicity offers valuable insights into the deformation and stress patterns that characterise the region. Despite the fact that the region is subject to routine seismic monitoring by several local agencies, a comprehensive, uniformly processed earthquake catalogue has yet to be produced for the Eastern Alps. Also, the spacing of permanent seismic stations in the region varies considerably. Because moderately sized earthquakes are rare in the Eastern Alps, the detection threshold must be as low as possible to include low-magnitude seismicity. This requires both a dense and uniform station network, as well as highly specialised and fine-tuned methods.

The recent AlpArray Swath-D network, active from late 2017 to late 2019 (Chapter 2), provided a unique opportunity to build a comprehensive seismicity catalogue for the Eastern Alps. I developed a workflow for the waveform-based detection and relocation of seismic events, which I describe in detail in Chapter 3. Anthropogenic events are frequently recorded in addition to seismic activity due to the high population density and heavy industrialisation in much of the study area. For a correct interpretation of the seismicity, the anthropogenic events (e.g. quarry and mine blasts) need to be identified. This is the focus of Chapter 4, where I discuss two distinct approaches. In Chapter 5, I describe the methods used to calculate magnitudes for the events in the earthquake catalogue and analyse the results for different parts of the study area. The complete seismicity catalogue is presented in Chapter 6. Chapter 7 provides a detailed analysis of the most active seismicity clusters in the catalogue. Finally, the conclusions of this thesis and an outlook are presented in Chapters 8 and 9, respectively.

CHAPTER 2

The AlpArray initiative

2.1 The AlpArray backbone network

AlpArray is a dense array of temporary broadband seismological stations that covers the wider alpine region (Hetényi, Molinari, et al., 2018). The array was planned to fill the gaps between 352 existing permanent stations and thereby achieve a homogeneous coverage with a spacing of around 50 km. In the period from March 2015 to July 2017, a total of 276 temporary stations were installed for this purpose. These temporary stations were active until the latter half of 2022. Data from the AlpArray seismic network is available through the European Integrated Data Archive (EIDA). The temporary stations are identified by the network code Z3, permanent stations included in the AlpArray network were not renamed, but the complete collection of permanent and temporary stations can be accessed through the virtual network code _ALPARRAY. All stations from the AlpArray network that were used in this work, are included on the map in Figure 2.1. These comprise stations from the networks BW, operated by the Department Of Earth And Environmental Sciences, Geophysical Observatory, University Of München (2001); CH, operated by the Swiss Seismological Service (SED) at ETH Zurich (1983); IV, NI (in collaboration with the OGS), RF, SI, and ST, operated by the INGV Seismological Data Centre (2006); OE, operated by the ZAMG-Zentralanstalt Für Meterologie Und Geodynamik (1987) (now GeoSphere Austria); and OX, operated by Istituto Nazionale di Oceanografia e di Geofisica Sperimentale (OGS) (2016) in collaboration with the INGV.

2.2 The AlpArray Swath-D network

Beside the AlpArray backbone stations, additional experiments were carried out on more local scales. The AlpArray Swath-D network (Heit et al., 2021) (Figure 2.1), which has been the main focus of my research, was one of these AlpArray complementary experiments. Its main purpose was to further densify the station coverage in a part of the Alps that is of particular geological and geophysical interest. It is the location of the postulated Moho gap and subduction polarity reversal. In addition, the Eastern Alps show some of the highest deformation rates in the Alpine orogen, for example in the Montello-Friuli thrust belt in north-eastern Italy, next to areas that show very little active deformation, such as the Tauern Window. The AlpArray backbone network was expected to be too sparse to resolve these relatively small-scale local structures.

Swath-D consists of a total of 163 broadband stations, with network code ZS. Its station codes start with the letter D, followed by a three digit number from 001 to 163. The initial network consisted of 151 stations provided by the Geophysical Instrument Pool Potsdam (GIPP) of the GeoForschungsZentrum Potsdam (GFZ). The majority of these 147 stations were installed in the fall of 2017. Four stations, D030 and D142 through 144, were added in the summer of 2018. In late 2018, the network was extended towards the east with ten additional stations provided by the Ludwig-Maximilians Universität München (LMU). These stations, with station codes D154 though D163, are part of the Deutsches Seismologisches Breitband Array (DSEBRA) (Schlömer et al., 2022). All Swath-D stations were dismantled by the end of 2019.

2.2.1 Technical specifications

Three different configurations of equipment were used for the initial 151 stations in the Swath-D network. About half of the stations (76 to be precise) were transmitting data back in real-time. These stations were usually placed indoors where they could be connected to mains in areas with cellular network reception, preferably in a basement or outhouse. The seismometer on these stations was a Güralp CMG-3ESP 60s, combined with an EarthData EDR-210 datalogger. A backup battery was installed in case of power outages. On locations without access to mains or cellular network, stations were equipped autonomously. In this case the sensor was usually buried while placed on a cemented marble plate, with an inverted insulated bucket placed over the top for protection. These stations used a Nanometric Trillium Compact 120s seismometer in combination with a DiGOS Omnirecs DATA-CUBE type 2 datalogger. For power, they relied on two zinc-air batteries that were either buried in a plastic bag or placed in a box on the surface, in both cases allowing airflow using a hose. The third station setup was

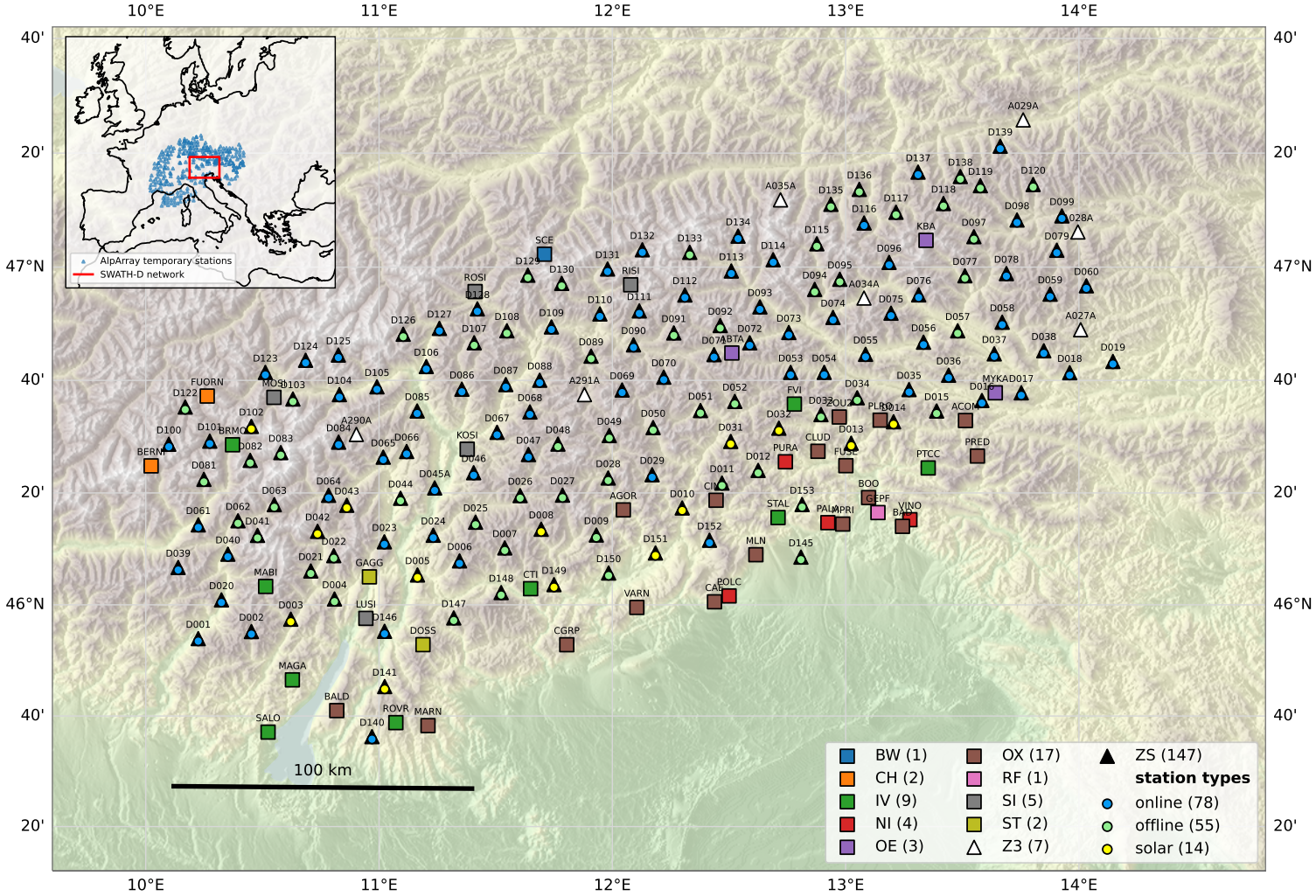

Figure 2.1. Map showing the station distribution of stations used in this work: the Swath-D network (black triangles), temporary stations of the AlpArray backbone network (white triangles), and permanent AlpArray stations (squares coloured by network code).

a solar-powered autonomous station. This setup was used on 14 stations where there was no access to mains, but an unobstructed view of the sky towards the south. These stations consisted of a Güralp CMG-3ESP 60s, combined with an EarthData PR6-24 datalogger. Two solar panels were erected at an angle close to vertical on a simple metal frame to avoid the buildup of snow, and connected to a pair of gel-batteries through a solar charger for power. Data from the autonomous stations had to be collected manually from the hard-drives during service trips. Examples of the deployment of each of the three station types in the field are shown in Figure 2.2. The technical specifications are summarised in Table 2.1. A map of the Swath-D network layout including the different station types is presented in Figure 2.1.

Equipment	**online**	**offline**	**solar**
Sensor	Güralp CMG-3ESP 60s	Nanometric Trillium Comp. 120s	Güralp CMG-3ESP 60s
Datalogger	EarthData EDR-210	DiGOS Omnirecs DATA-CUBE 2	EarthData PR6-24
Power	Mains + backup gel-battery	2 9V zinc-air batteries	2 solar panels + 2 gel-batteries
Real-time data	yes	no	no

Table 2.1. Equipment used for the stations of the Swath-D network.

Figure 2.2. Examples of the deployment of different station types in the field. Online station (left), offline station (center), solar-powered station (right). All pictures were taken by me.

2.2.2 Station performance

An overview of the data availability for the period from 1 November 2017 to 1 November 2019 is shown in Figure 2.3. The DSEBRA stations are not included in this figure because data from these stations were not used. During the first year of deployment, a notable decline in the number of available stations was

observed starting from mid-November 2017. By April 2018, approximately half of the autonomous stations ceased to function due to loss of power. During the service trips in the spring of 2018, we learned that the stations where the batteries were left on the surface exhibited significantly longer battery performance compared to stations with batteries buried in a plastic bag. It became evident that the ventilation hoses were not functioning as anticipated, while low surface temperatures turned out to be a less significant issue. In preparation for the second winter, all batteries for the autonomous stations were left in boxes on the surface, which resulted in a more reliable performance. The performance of the real-time (online) stations was found to be quite stable during the entirety of the experiment. However, in early August 2019, problems arose with data transmission. Due to a concurrent software issue, the data were not stored locally as is normally the case. This unfortunate coincidence resulted in significant loss of data on numerous online stations for a period of a few days.

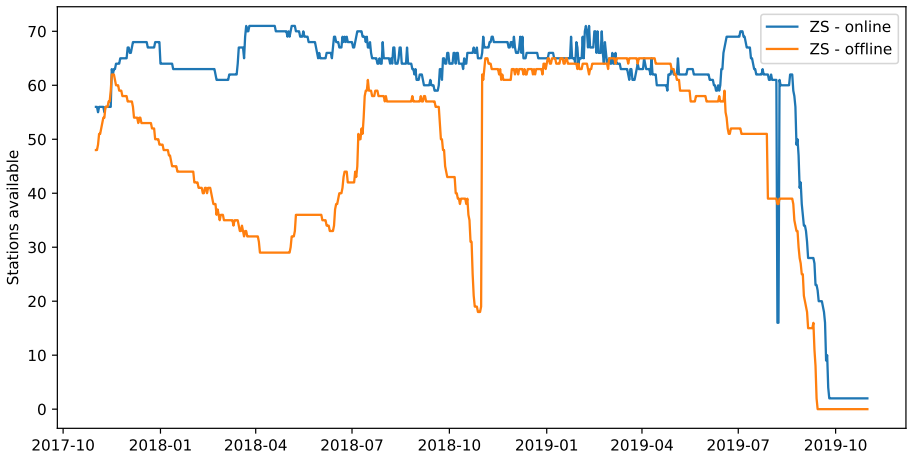

Figure 2.3. Station availability for the Swath-D network between 1 November 2017 and 1 November 2019. In this graph, a station is considered available for a specific day if it has any amount of data on any number of channels. It should be noted that this does not imply completeness of the data. The DSEBRA stations (D154-D163) are not included.

An assessment of the data quality of the Swath-D stations, as well as the AlpArray backbone stations was made by Petersen, Cesca, Kriegerowski, et al. (2019), providing relative gain factors, sensor orientation corrections, and reliable frequency bands. A data example for the entire station selection for a relatively large earthquake of magnitude M_w 3.7 that took place near the village of Tolmezzo in Friuli, Italy on 14 June 2019 is shown in Figure 2.4. For the purpose of comparison, appendix Figures A1-A3 show the same event using exclusively data from the online Swath-D stations, data from the offline Swath-D stations, and data from permanent stations respectively.

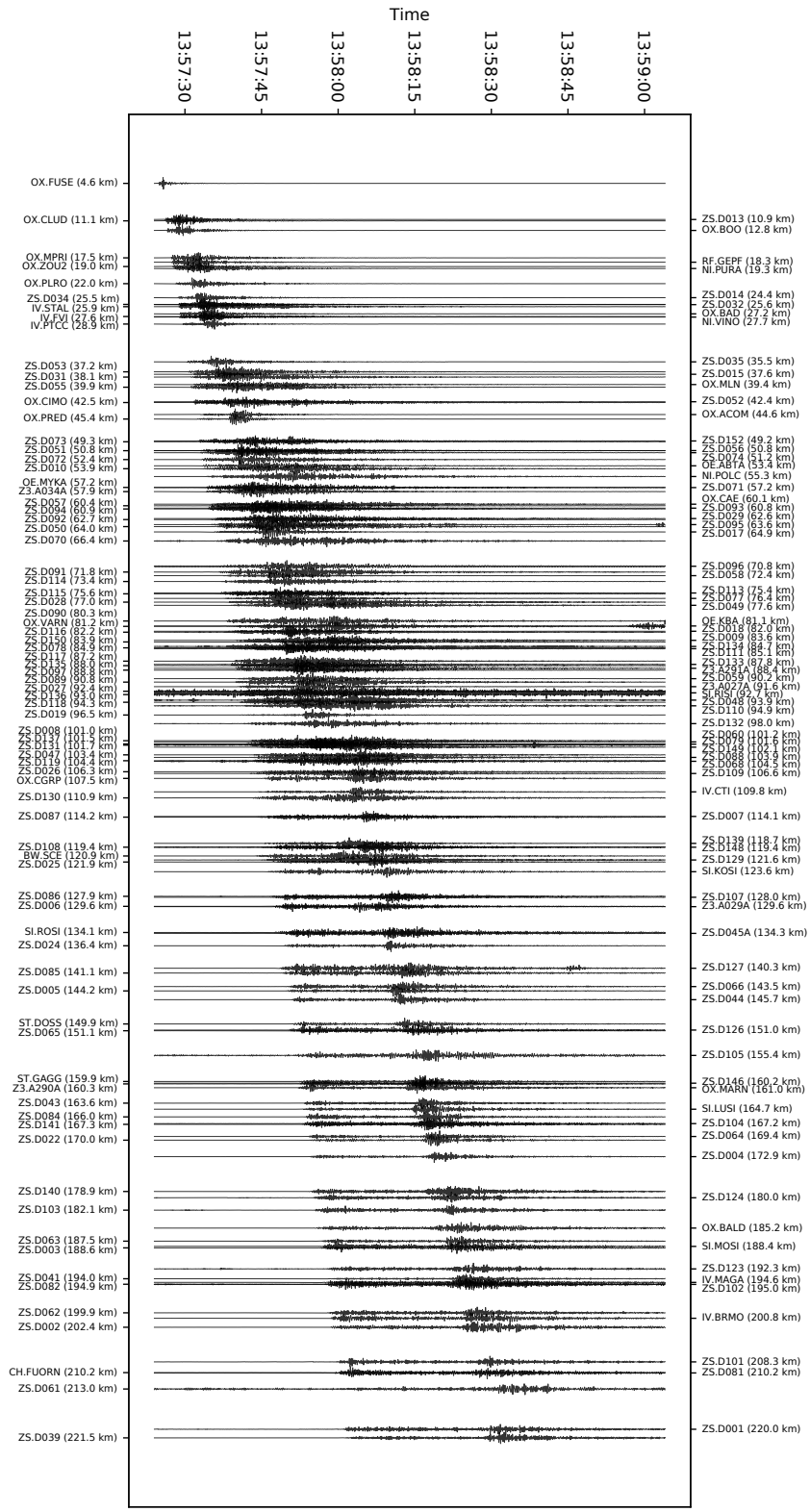

Figure 2.4. Vertical channel event waveforms for a relatively large earthquake of magnitude M_w 3.7 that took place near the village of Tolmezzo in Friuli, Italy on 14 June 2019 at 13:57:24 (UTC). Stations are sorted by distance from left to right. The waveform data is band-pass-filtered between $2 - 8$ Hz.

CHAPTER 3

Waveform based methods

The following chapter presents the methods that I have used and developed for the detection, phase-picking, and location of earthquakes using data from the Swath-D network in the Eastern Alps (Section 2.2). The workflow is centred on *template matching* (Section 3.1) and is illustrated in Figure 3.1. Template matching is a technique that requires a-priori knowledge about the locations and occurrence times of an initial subset of earthquakes in the region. This information is publicly available thanks to the local earthquake services. However, each of these catalogues covers only part of the region, and the station coverage prior to the deployment of the Swath-D network was quite inhomogeneous. To prevent a detection bias, I applied an energy-based detection algorithm to supplement the catalogues with events detected using data from the Swath-D network. These steps are described in Section 3.1.2. Finally, I developed an automated workflow to pick and locate the events, which I present in Sections 3.2 and 3.3. Precise phase-picks are essential for accurately locating the detected events. This workflow was published in Hofman, Kummerow, and Cesca (2023). The resulting seismicity catalogue including a classification of the detected events (Chapter 4) and earthquake magnitudes (Chapter 5) is presented in Chapter 6.

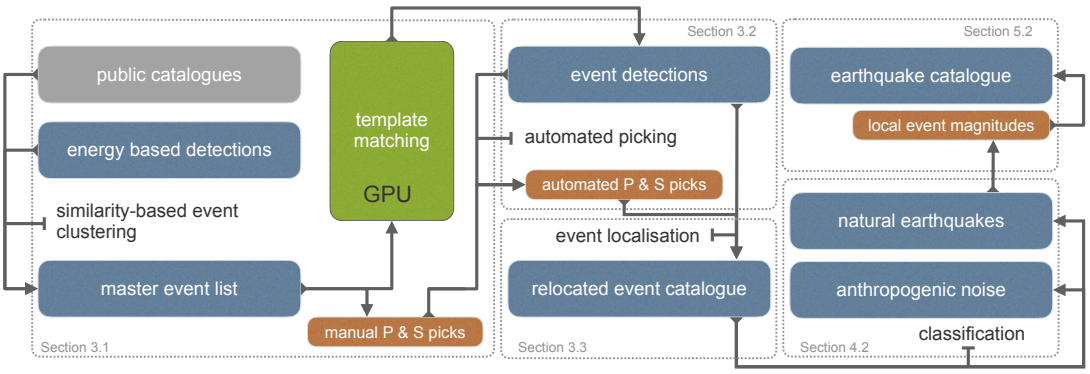

Figure 3.1. Schematic overview of the workflow presented in this chapter. The three columns in this figure represent the three main sections in this chapter, where the methods involved are explained in detail.

3.1 Template matching

3.1.1 Introduction

Template matching – also referred to as *matched filter* – is a signal processing technique with the aim to detect patterns in data based on examples. The example pattern is called the *template*, and can be either synthetic or a slice of the actual data where a known signal occurs (see Section 3.1.2). This template is then compared to longer sections of data in terms of waveform similarity. If the template signal repeats itself in the data, the repeating occurrences will be revealed by a high waveform similarity. The similarity of two time-signals can be measured by cross-correlation using the correlation function. This function is equivalent to convolution, but without the folding of one of both signals. The cross-correlation of two real-valued, discrete time signals $f(t)$ and $g(t)$ can conceptualised as sliding the two signals past one another and taking the area under their product. The amount of offset between the signals is called *lag* and is often expressed by the symbol τ. For two discrete, real-valued functions $f(t)$ and $g(t)$, the cross-covariance σ_{fg} as a function of lag τ can be expressed as

$$\sigma_{fg}(\tau) = \lim_{N\to\infty} \frac{1}{2N+1} \sum_{t=-N}^{N} (f_t - \mu_f)(g_{t+\tau} - \mu_g) \tag{3.1}$$

where μ_f is the mean of $f(t)$, and μ_g is the mean of $g(t)$. The cross-correlation r_{fg} as a function of τ is then defined as

$$r_{fg}(\tau) = \frac{\sigma_{fg}(\tau)}{\sqrt{\sigma_{ff}(0)\sigma_{gg}(0)}} \tag{3.2}$$

where σ_{ff} and σ_{gg} are the variances of $f(t)$ and $g(t)$. This means that the cross-correlation is normalised by the standard deviations of both functions and remains within the domain [-1, 1], where a value of 1 means that both functions are exactly equal, and a value of -1 means that both functions are exactly opposite. In both cases, however, they may also be a scalar multiple of each other as a result of the normalisation term.

In the typical seismological use case, the template signal is a recorded earthquake signal – either a single phase (e.g. Ross et al., 2019) or a complete earthquake waveform (e.g. Beaucé et al., 2019), which is cross-correlated against a longer section of data recorded by the same instrument. This way, a detection can be thought of as a signal from an earthquake similar to the earthquake from which the template signal originated in terms of hypocentre location, source-time function, and mechanism. This method has demonstrated its effectiveness in many studies, especially for the detection of low magnitude earthquakes (e.g. Gibbons and Ringdal, 2006; Skoumal et al., 2015; Vuan et al., 2018; Ross et al., 2019; Beaucé et al., 2019). Applying the correct normalisation is very important for the application in seismology, as it implies that the amplitude of the data signal does not have to be the same as the template amplitude. In fact, earthquake signals vary over many orders of magnitude. Figure 3.2 shows an example of earthquake signals detected with this method. Among the detections is a signal with a maximum amplitude that is 50 times lower than the template amplitude, as well as a signal with a maximum amplitude that is 160 times greater, though both detections have roughly the same normalised correlation coefficient (0.66 and 0.64).

Because the cross-covariance is basically a convolution with one function folded in time, the convolution theorem can be applied. This implies that the numerator of the cross-correlation function can be calculated in the frequency domain as the point-wise multiplication of the Fourier transform of the two signals. This is important because it allows for a faster computation using a fast Fourier transform (FFT). If the two signals are not of equal length, which is typically the case with template matching, the shorter signal has to be lengthened by appending zeros.

The implementation of the template matching method for my use case posed three main challenges: (1) the relatively large data volume (198 stations, 100 Hz sampling rate, 24 month-recording time), (2) the low magnitude of the seismic events, and (3) variable data availability. I developed a highly efficient template-matching code in Python, that was able to process the complete dataset in about two weeks time without the use of high-performance computing power. The main

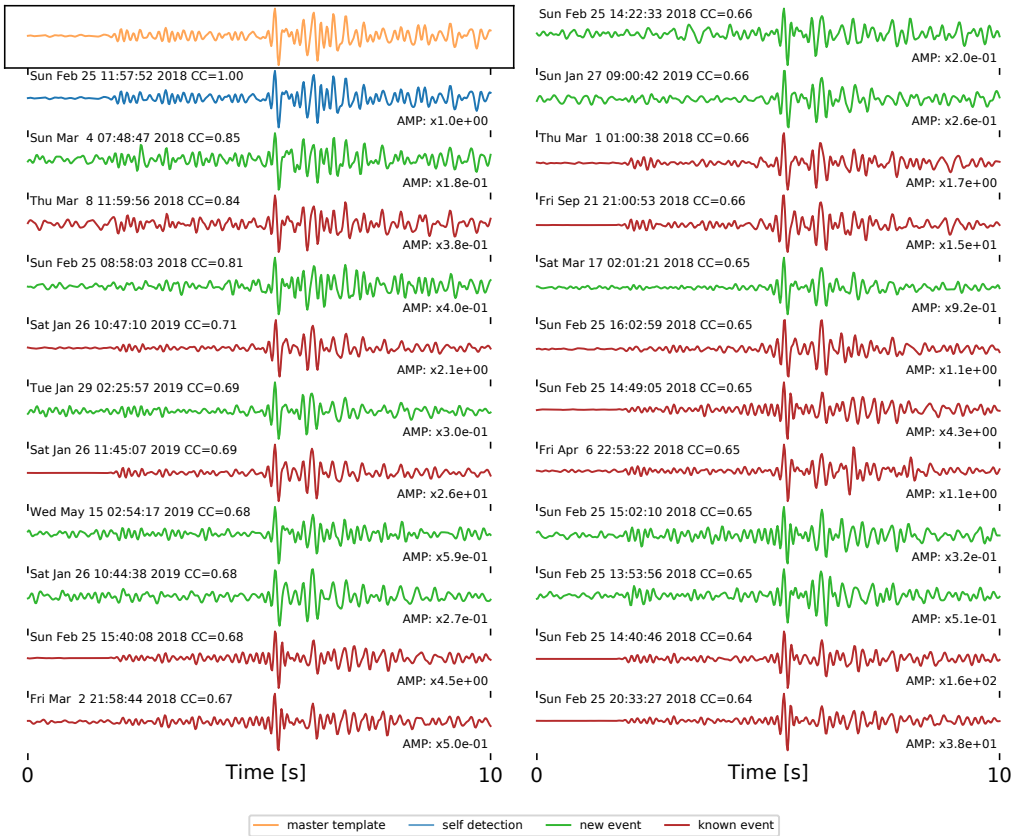

Figure 3.2. Example of template detections from a single template waveform from station D152. The first waveform is the *template* (orange), followed by its detections sorted by similarity from high to low. The first detection is the self-detection of the template waveform in the continuous data (blue), with a maximum cross-correlation coefficient of 1. Other detections can be separated into known events that can be found in the public catalogues (red), and unique detections (green).

processing steps including the calculation of the cross-correlation functions, were performed on a *Nvidia GV100* graphics processing unit (GPU) with $8,192$ cores.

Instead of using individual-phase templates, I decided to use the full event waveforms including the first P- and S-wave arrivals. This greatly reduces the number of false detections because the template windows that need to be matched are much longer (10 seconds). It also limits the source volume for detected events, by requiring the S-P traveltime to be very similar to the template event, reducing the need for stacking or beamforming of cross-correlation functions. This choice also provides the opportunity to process the data channel-wise, instead of template-wise, which allowed me to make the code much more efficient.

3.1.2 Selection of template events

In order to compile a list of candidate templates, I used a combination of events from the local earthquake monitoring agencies, and energy-based detections. Events located at a distance of more than 50 km from the nearest Swath-D station were excluded. Given the dense station spacing of the network, this affects only events outside of the network that would otherwise be impossible to locate. Double entries were removed by allowing only one event within a spatiotemporal window of 50 km and 15 s. In the case of overlapping events, the catalogued events were given precedence over the energy-based detections.

Local earthquake catalogues

The area of the AlpArray Swath-D network is covered partly by several national and regional earthquake agencies and institutions. These are the Istituto Nazionale di Oceanografia e di Geofisica Sperimentale (OGS) (2016) and INGV Seismological Data Centre (2006), GeoSphere Austria (previously ZAMG-Zentralanstalt Für Meterologie Und Geodynamik, 1987) and the Swiss Seismological Service (SED) at ETH Zurich (1983). Catalogues from these agencies were downloaded using the FDSN-webservices for a period of two years from November 2017 to October 2019. All events with a distance larger that 50 km to the nearest Swath-D station were excluded. The events that were considered as template candidates are shown in Figure 3.3.

Energy-based detection

A common method for detecting earthquakes involves examining data recordings to search for transient signals. This is typically accomplished through the utilisation of a trigger function, such as the ratio of the short-term average (STA) to the long-term average (LTA) of the signal's energy within a sliding window. The appearance of a transient signal will result in a rapid increase in the short-term average, while the long-term average will remain relatively unaffected, leading to an increase in the STA/LTA ratio. Other trigger functions use for example the analytic envelope of the signal, or z-statistics. An overview of the classical trigger functions is provided in Withers et al. (1998).

To distinguish a local noise signal from an earthquake signal, trigger functions from multiple stations need to be combined. The simplest way is to define a minimum number of stations within a network that need to be triggered simultaneously, a coincidence trigger. This reduces the chance of false positives, but provides little information about the origin of the source. A more advanced ap-

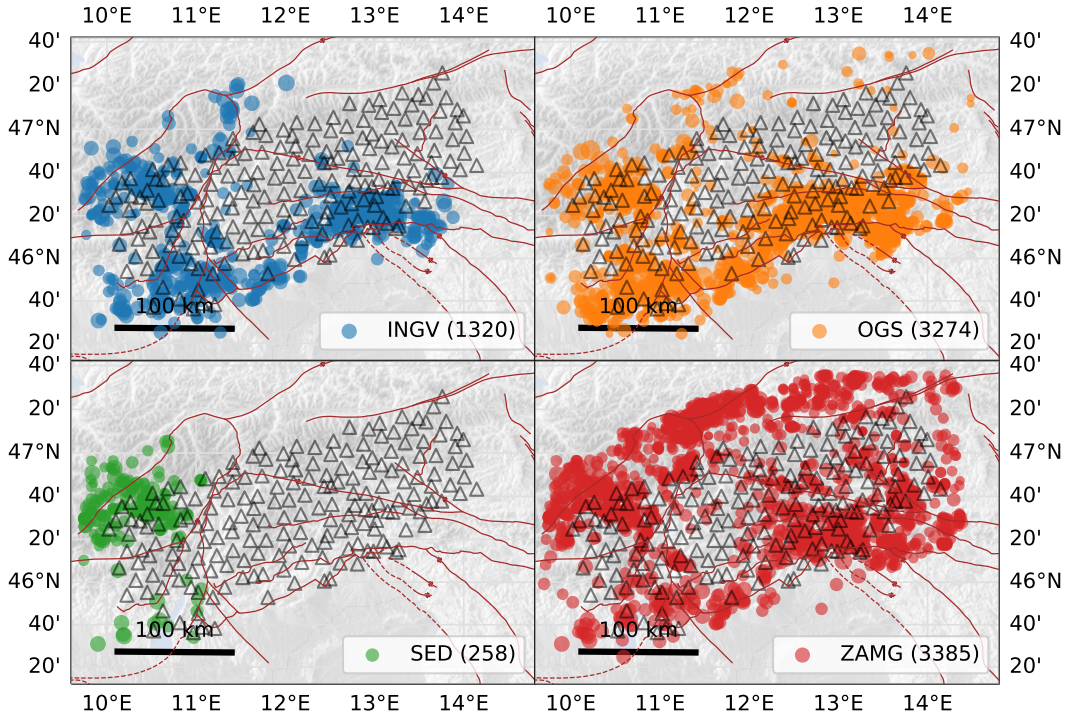

Figure 3.3. All publicly available earthquake catalogues used in this work (INGV Seismological Data Centre (2006) and Istituto Nazionale di Oceanografia e di Geofisica Sperimentale (OGS) (2016), the Swiss Seismological Service (SED) at ETH Zurich (1983), and GeoSphere Austria (previously ZAMG-Zentralanstalt Für Meterologie Und Geodynamik, 1987).) Whereas the SED catalogue covers only the western part, the INGV, OGS, and ZAMG catalogues cover the entire region.

proach is implemented in the earthquake detection algorithm *Lassie* (Heimann et al., 2017). Here, the trigger functions are shifted along a predefined slowness and backazimuth grid and stacked to create an image function – a technique known as *beamforming*. If a seismic signal actuates the trigger functions, the stack matching the node point that is closest to the actual source of the signal is expected to have the highest peak value. This gives an approximate source location and time of the signal. An example of such a detection is provided in Figure 3.4.

In the original implementation, trigger functions from all stations in the network contribute to the image at each node point. For the small magnitude seismicity within the Swath-D network however, seismic energy reaches only a limited number of stations before it falls below the noise level. By stacking trigger functions from all stations, the signal would therefore be completely outweighed by noise. To overcome this problem, I developed a station weighting scheme that allows a

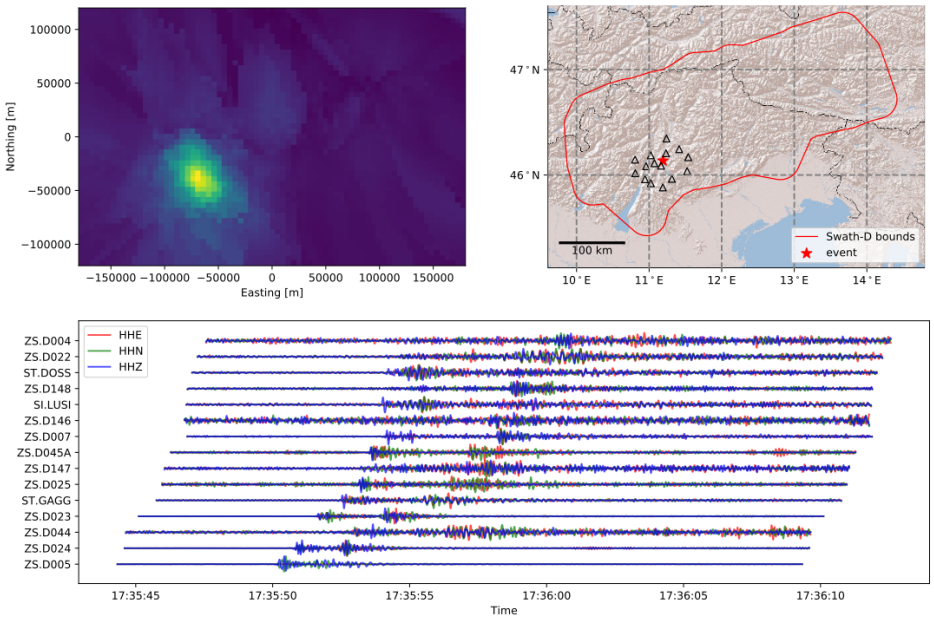

Figure 3.4. Example of an event detected using *Lassie* (Heimann et al., 2017). The upper left panel shows the image function (stacked trigger functions) at the time of the detection. The upper right panel shows the approximate epicenter location (red star), as well as the stations that contributed to the image function at the corresponding grid node. The waveforms from these stations are shown in the lower panel.

`StationLimit` to be set. The value of this parameter defines the number of stations contributing to the stack. For each node, only the closest `StationLimit` stations will be used. I implemented this option, that is available on the `weighting` branch of the git page, together with Sebastian Heimann (GFZ), the main developer of Lassie.

The entire dataset was scanned with Lassie to search for earthquakes and compensate for a possible detection bias in the local earthquake catalogues. A two-dimensional search grid of 360 km east-west and 240 km north-south, with 5 km node spacing was used. The source depth was fixed to 15 km. The `StationLimit` parameter was set to 15. Using these settings, 3,511 events were detected. The vast majority of these detections could be correlated with earthquakes in the local earthquake catalogues (see also Section 3.1.2). From the remaining part, 592 events could be located and were included in the final catalogue. 306 of these events are classified as anthropogenic noise (see Chapter 4 for details on the classification), leaving 286 potential new earthquake detections. These events are shown in Figure 3.5. The relatively low number of newly detected earthquakes

using the energy-based method demonstrates the quality of the local earthquake catalogues. These newly detected events are spread throughout the network, and their distribution resembles the general event density patterns from the public earthquake catalogues illustrated in Figure 3.3. The majority of the detections are located in the Friuli region and the Engadine and in the Ortler Alps, but a smaller amount of events have also been detected in the Dolomite Indenter and Tauern Window regions.

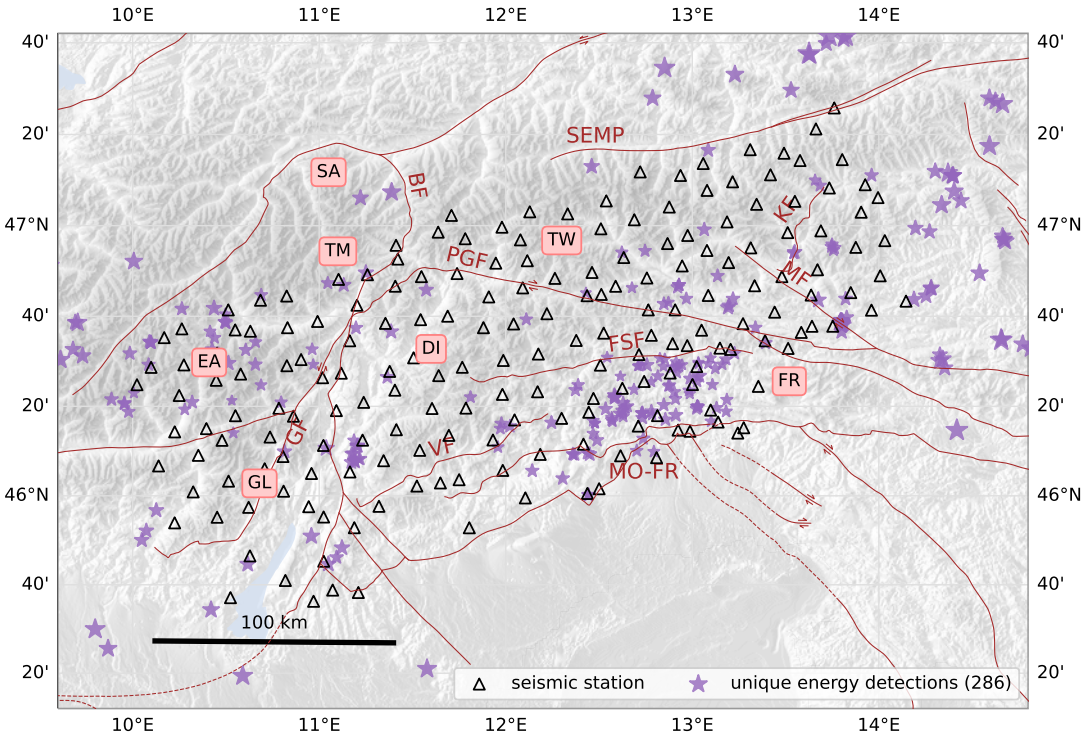

Figure 3.5. All energy-based event detections using Lassie (Heimann et al., 2017) that were not found in any of the public earthquake catalogues (Figure 3.3) and were not marked as quarry blasts (see Chapter 4). This figure shows the final locations of these events (see Section 3.3).

Template extraction

For the resulting set of events, template waveforms are extracted from the continuous data on the vertical channel on the 15 stations closest to the event epicentre. By assuming a constant seismic velocity and straight ray-path, the first P-wave onset can be estimated accurately enough to define a 10 s window that includes both the first P-wave, as well as the S-wave onset. An example of the selection windows for an event in the Swiss Alps is illustrated in Figure 3.6.

The signal to noise ratio (SNR) is calculated to ensure that a signal is captured

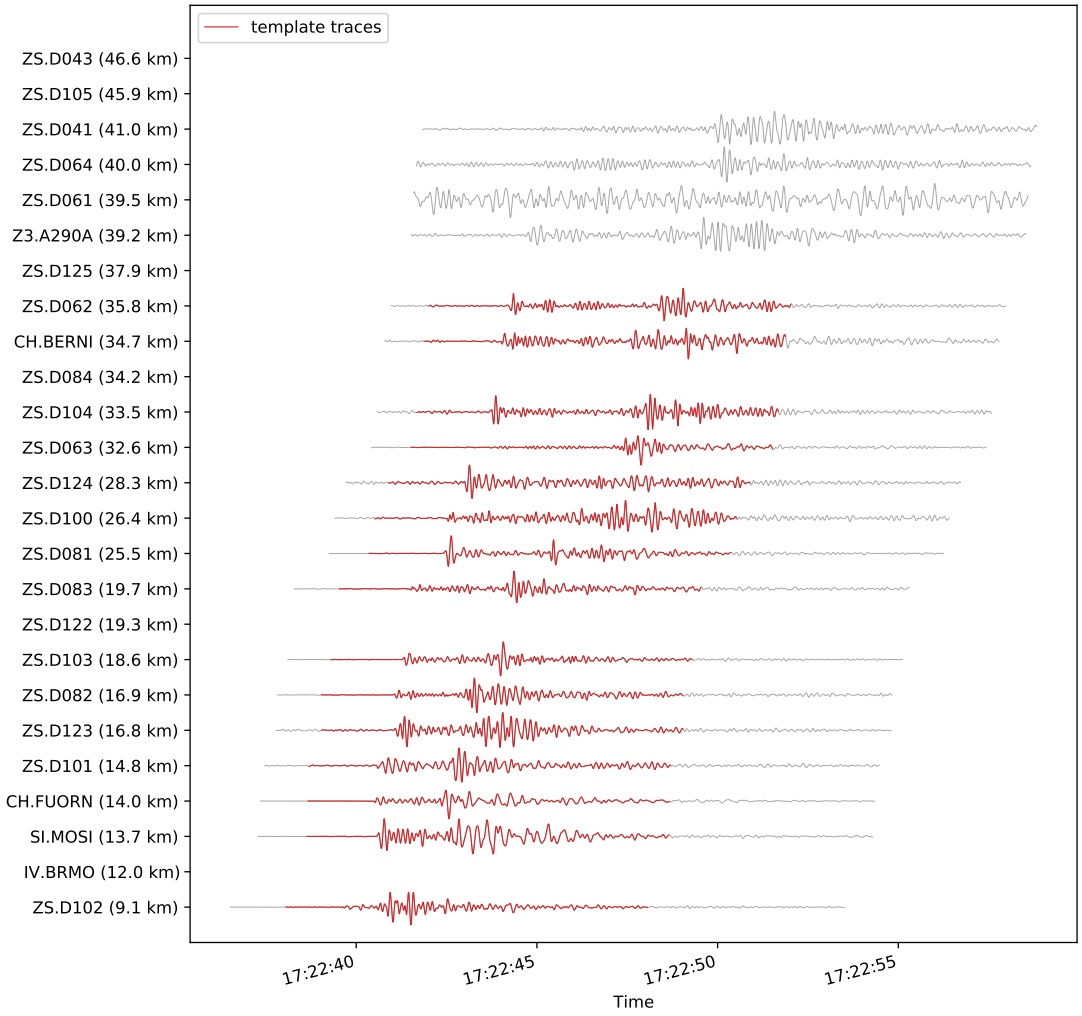

Figure 3.6. This example illustrates the extraction of template waveforms for an event occurring on 2 February 2019 at 17:22:38 (UTC) in the vicinity of the Münstertal valley in the Swiss Alps (in the north-western part of the Swath-D network). Note that stations BRMO, D122, D084, D125, D105, and D043 have no data available for the event. Nevertheless, 15 template waveforms with adequate signal-to-noise ratios could be extracted for the remaining stations.

within the window, where the root mean square (RMS) of a sliding .1 s window is required to exceed the RMS of an adjacent 1 s window by more than 5 times at least once. Once these template waveforms have been extracted, highly similar events are clustered and redundant templates are removed. This reduces the computational load and prevents unnecessary duplicate detections. Events are considered highly similar when the median of the three highest cross-correlation values exceeds a threshold of 0.7. In this case, the event with the highest number of matches among the template events is retained, whereas the other template event is removed from the selection. This criterion is more stringent than the general template matching criterion (see Section 3.1), thus ensuring that the removed template event will be re-detected by the template event that is retained. Ultimately, this yielded a list of 28, 207 template waveforms for a selection of 2, 036 template events (also referred to as *master events* in the subsequent chapters).

3.1.3 Technical implementation

The template matching code has been developed completely by me in the programming language Python (Van Rossum and Drake Jr, 1995). Beside its broad standard library, Python offers an enormous amount of third-party packages for a wide range of applications, including scientific computing. The most important packages that I have used include: ObsPy (Beyreuther et al., 2010) for reading, writing and processing of seismological data; NumPy (Harris et al., 2020) for efficient array operations; and CuPy (Okuta et al., 2017) for GPU processing.

The data is processed channel by channel. First, all template waveforms and continuous data files are gathered for a specific channel. Depending on the size of the GPU memory, the first N_{temp} template files and N_{data} continuous data files (24-hour traces) are read and preprocessed in parallel on the CPU by using a separate process for each file. Preprocessing includes detrending, band-pass-filtering between $2-8$ Hz, and downsampling to 50 Hz. Zeros are appended to the template traces to match the length of the longest data trace, as well as to any shorter data trace, while keeping track of the original lengths. The preprocessed data is then moved to a template-array and a data-array on GPU. Whilst on the GPU, I calculate the energy of the template waveforms, as well as the energy of the data traces in a sliding window corresponding to the template length. This is done efficiently using array operations. Next, all data is converted to the frequency domain using the fast Fourier Transform (FFT) in Cupy. The cross-variances of all template-data combinations are then calculated simultaneously with a single matrix multiplication, converted back to the time-domain, and normalised using the energy of the template traces and the windowed energy of the data traces to obtain the fully normalised cross-correlation tensor (Equation 3.3). Now, we read the next N_{temp} template files, while the first N_{data} data FFTs ares still loaded on the GPU. Since the template waveforms are already preprocessed, we only

have to calculate their energy, load them onto the GPU and convert them to the frequency domain, before we can calculate the next $N_{temp} \times N_{data}$ cross-correlation functions. Once we have looped through all of the template files for the channel, we skip to the next N_{data} continuous data files and start again with the first N_{temp} templates. For each iteration, I define the cross-correlation tensor R as

$$R_{ijk} = \frac{\mathcal{F}^{-1}\{\sum_{\xi} \mathcal{F}\{temp_i\}(-\xi)\mathcal{F}\{data_j\}(\xi)\}}{\sqrt{\sum_{l=0}^{N} temp_{il}^2 \sum_{l=k}^{k+N} data_{jl}^2}} \tag{3.3}$$

where R_{ijk} represents the fully normalised cross-correlation coefficient of template i with data trace j shifted by k samples. The multiplication of k with the sampling interval yields the time lag τ from Equation 3.2. The vector R_{ij} has a length of M - N + *1* samples, M being number of samples in data trace j, and N the number of samples in the template trace i. Symbols $\mathcal{F}$ and $\mathcal{F}^{-1}$ denote the Fast Fourier Transform operator and its inverse, respectively. An efficient algorithm searches for all peaks in the cross-correlation functions that are above the threshold (0.5), which are appended to separate files for each template. Assuming that a potential detection is co-located with the master event used for the template extraction, the origin time of the detected event can be estimated by subtracting the time difference between the master event origin and the start of the template window from the cross-correlation lag time. This implies that the station travel-time for the detected event is equal to the travel-time for the master event. After all template waveforms are cross-correlated, the detections from individual template waveforms are combined. A match is then defined when three template waveforms belonging to the same master event exceed the cross-correlation threshold of 0.5, and the estimated origin-times are within 5 s distance. The detected event is then incorporated into the *template family* of the master event. In case multiple master events detect the same event, for the sake of further processing it is added to the template family of the master event with which it has the highest degree of similarity. The similarity is defined as the median of the three highest maximum cross-correlation coefficients. An example of an event detection by combining the matches from different template waveforms is shown in Figure 3.7. More examples are shown in appendix Figures A4-A7.

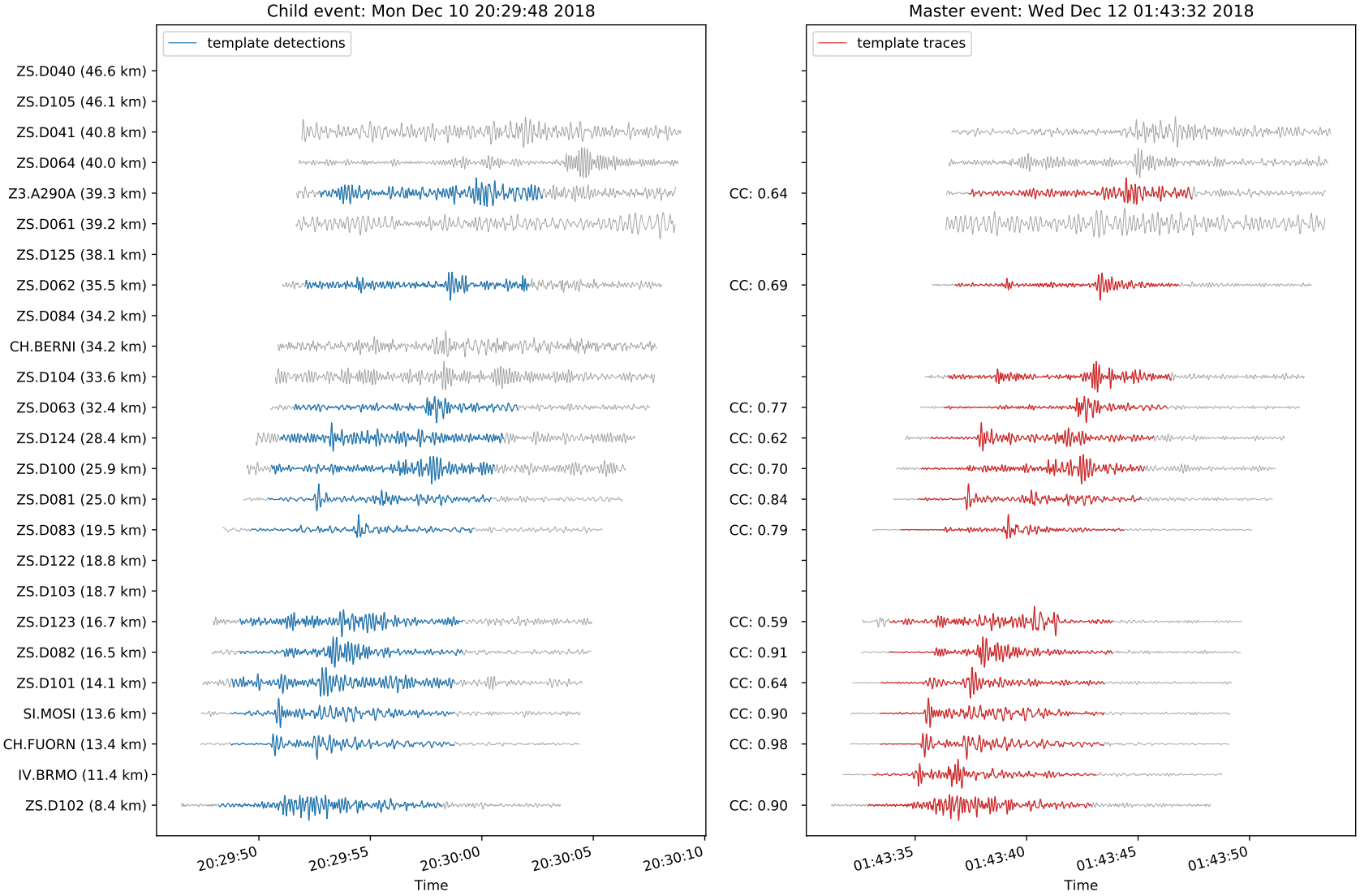

Figure 3.7. Example of an event detection by template matching with very similar waveforms for many different stations. These events are closely co-located. The master event is of magnitude $M_L = -0.7$, the detected event is of magnitude $M_L = -0.8$.

The template search yielded a total of 15,155 unique detections. This figure incorporates the self-detections of the master events, as well as anthropogenic noise signals (predominantly from quarry blasts). Lowering the threshold increases the number of detections, but may also result in the introduction false positives. While there is a potential for detecting more earthquakes, the SNR for these additional events will most likely be insufficient for picking and localisation. This is illustrated in Figure 3.8, which demonstrates that only a portion of the detected seismicity could be relocated. Nevertheless, the final catalogue comprises extremely small earthquakes, down to a completeness magnitude of -1.0 M_L, which is not typically achieved using conventional methods. This highlights the effectiveness of the workflow.

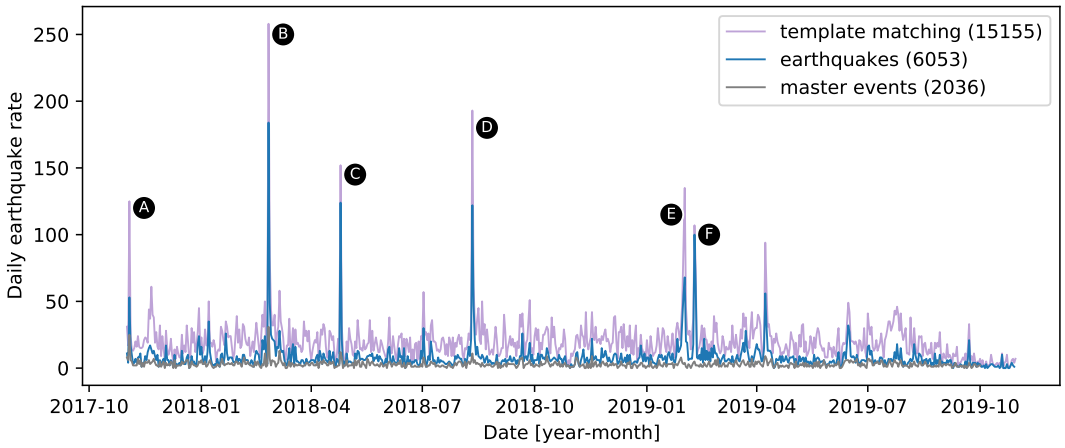

Figure 3.8. Daily event rate for the subset of master events (grey), all events detected by template matching (purple), and all earthquakes in the final catalogue (blue). Symbols $A - F$ mark event clusters with over 100 events in a single day. The locations of these clusters are indicated in Figure 6.1. This Figure appeared in Hofman, Kummerow, and Cesca (2023).

3.2 Semi automated phase-picking

Perhaps even more challenging than the detection of low SNR seismicity in a large dataset is the accurate detection of phase onsets needed for locating the detected events. Because the master event list is compiled from mixed sources (Section 3.1.2), my first step was to hand-pick these events and perform a first location iteration. This homogenises the starting catalogue and provides a basis for the automated picking method described in Section 3.2.2. The final set of P- and S- picks is then used to determine the hypocenter locations and origin times in a 3-D model of the seismic velocity.

3.2.1 Manual phase picking of master events

Using ObsPyck, a seismic phase picker from the developers of ObsPy (Beyreuther et al., 2010), I picked the onsets of the first P-wave and S-wave arrivals for all master events. For the purpose of picking, the waveforms were band-pass-filtered between $1 - 20\,\mathrm{Hz}$. The P-wave onsets were picked preferably on the vertical channel, whereas the S-wave onsets were usually picked on either of the horizontal channels, when available. This resulted in a set of $23,426$ picks, that I refer to as *master picks* in the next section. Using these picks, I performed a first location search using the probabilistic NonLinLoc software (Lomax et al., 2000). The origin times and locations of these master events then provided a starting point for the automated picks of the detected seismicity.

3.2.2 Automated phase-picking methods

The assumption that underlies my template matching approach is that the detected events are approximately co-located to their respective master events. This is enforced by requiring simultaneous detections on three different stations that imply a similar S-P differential travel-time. Building on this assumption, we can roughly predict the time windows for the phase arrivals of the detected events within each event cluster, by adding the travel-times from the master events to the estimated origin times of each of the detected events.

Cross-correlation of the master picks with data windows around the estimated phase arrivals for a detected event allows for a similarity-based automatic picking. However, this method has a few downsides. Firstly, only channels and phases with a master pick can be picked. Due to the variable station availability over time (see Section 2.2.2), it often happens that the subset of operational stations is different between the detected event and the master event. Secondly, the cross-correlation function is quite sensitive to noise, especially when a short wavelet is used. As a result of the normalisation (Equation 3.2), the side-lobes of the cross-correlation function are amplified, potentially causing an inaccurate phase-pick. This is illustrated in Figure 3.9. A classical STA/LTA trigger is very useful for roughly detecting a phase onset, but lacks the precision required for the subsequent localisation of the event. Combining the strength of both the cross-correlation function and the STA/LTA trigger, I developed a picking algorithm that uses a multiplication of these two functions, the maximum of which is used to determine the final pick. An example of this method is depicted in Figure 3.9.

The STA/LTA trigger is defined as in Earle and Shearer (1994), where the short-term average is calculated from the current sample forward in time, and the long-term average is calculated from a time window up to the current sample. Using

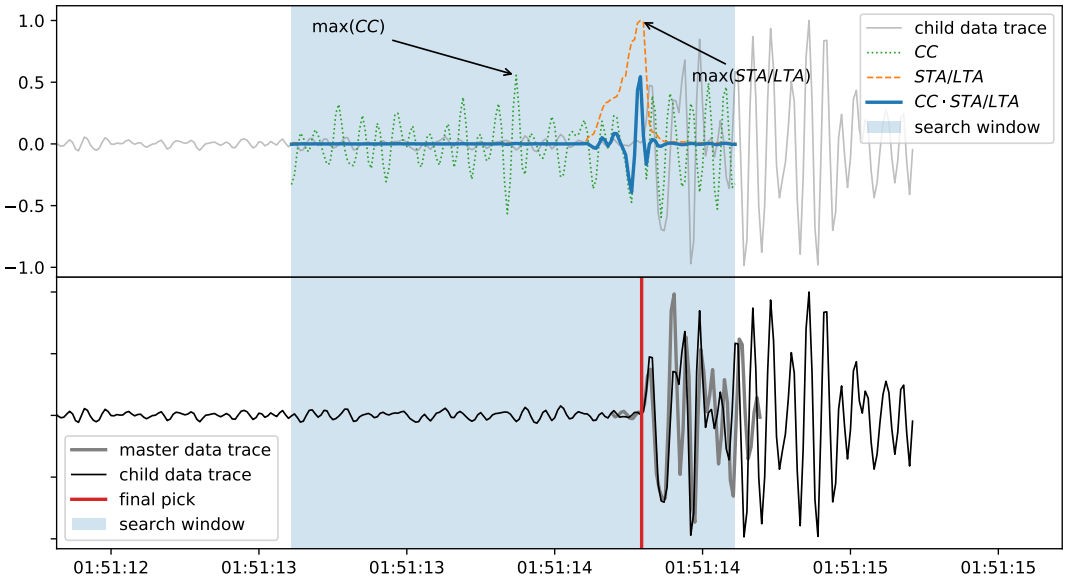

Figure 3.9. Example of the automated picking algorithm using a master pick. The final pick is based on the maximum of the product of the cross-correlation function, and an STA/LTA trigger. Note that the maximum of the cross-correlation is misaligned, and would lead to an inaccurate pick.

this definition, the maximum of the STA/LTA ratio forms a high plateau around the onset of the phase arrival, given that the window lengths are chosen correctly. When multiplied, the STA/LTA suppresses the side-lobes of the cross-correlation function and this yields a trigger function with a clear maximum, that is much less noisy than the original cross-correlation function. I use the index of this peak to evaluate the original cross-correlation function, to which the threshold (0.4) is then applied. Figure 3.9 illustrates this method, showing that the maximum of the original cross-correlation does not align with the phase-arrival. In the case of a very noisy search window, the influence of the STA/LTA diminishes because the function becomes flat. For channels without a master pick, the maximum of the STA/LTA is used as a standalone trigger. In that case, a threshold is set for the absolute value of the STA/LTA ratio. All important parameters used in this method are shown in Table 3.1. Three more examples to illustrate the method are shown in appendix Figures A8-A10.

Parameter	**P-phase**	**S-phase**
Band-pass filter window	[1 Hz, 20 Hz]	[1 Hz, 12 Hz]
STA & LTA length	0.2 s / 0.6 s	0.2 s / 0.8 s
STA/LTA threshold	10	10
Cross-correlation threshold	0.4	0.4
Correlation window relative to pick	[-0.2 s, 0.3 s]	[-0.2 s, 1.3 s]

Table 3.1. Parameter settings for the automated phase-picking.

The application of this workflow to the events detected by template-matching yielded an additional 95-thousand automated picks for 9-thousand events, not including events with fewer than 6 picks. Figure 3.10 illustrates the distributions of the picks in relation to the methods outlined in this section, the seismic network contributions (number of picks within each network), and the ratio of P- versus S-picks. The ratio of automated picks to manual picks is arguably dependent on the extent of the dataset. It is likely to increase when a longer time period is analysed by increasing the size of the template families, or when a smaller spatial volume is used by reducing the number of template families. Nevertheless, the number of automated picks is considerable, and manual picking such a large number of traces would be extremely time consuming for any seismologist, particularly given the low SNR of the majority of the data. The network contributions chart emphasises the importance of the Swath-D stations in the establishment of the event catalogue. Finally, the ratio of P-picks to S-picks demonstrates that the workflow is optimised for both P- and S-phase processing.

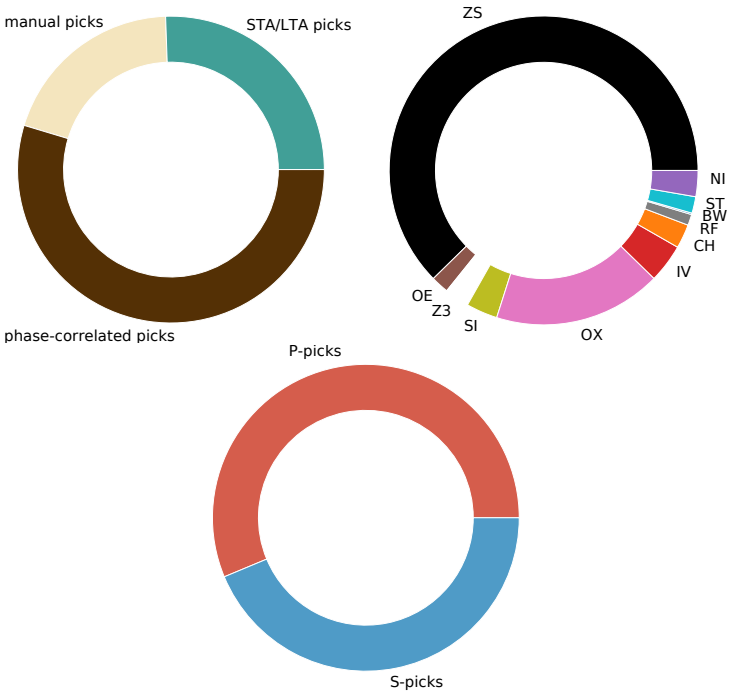

Figure 3.10. Number of picks made using the different methods outlined in this section (top left), number of picks attributed to each of the contributing networks (see Chapter 2) (top right), and the number of P- versus S-picks (lower).

Additional statistics for each individual station including the number of event contributions as well as the number of P- and S-picks with the associated errors are provided in appendix Table A1. An illustrative example is also provided in Figure 3.11, where my workflow using a combination of manual picks and automated picks is demonstrated for an event pair in the Engadine Alps in Switzerland.

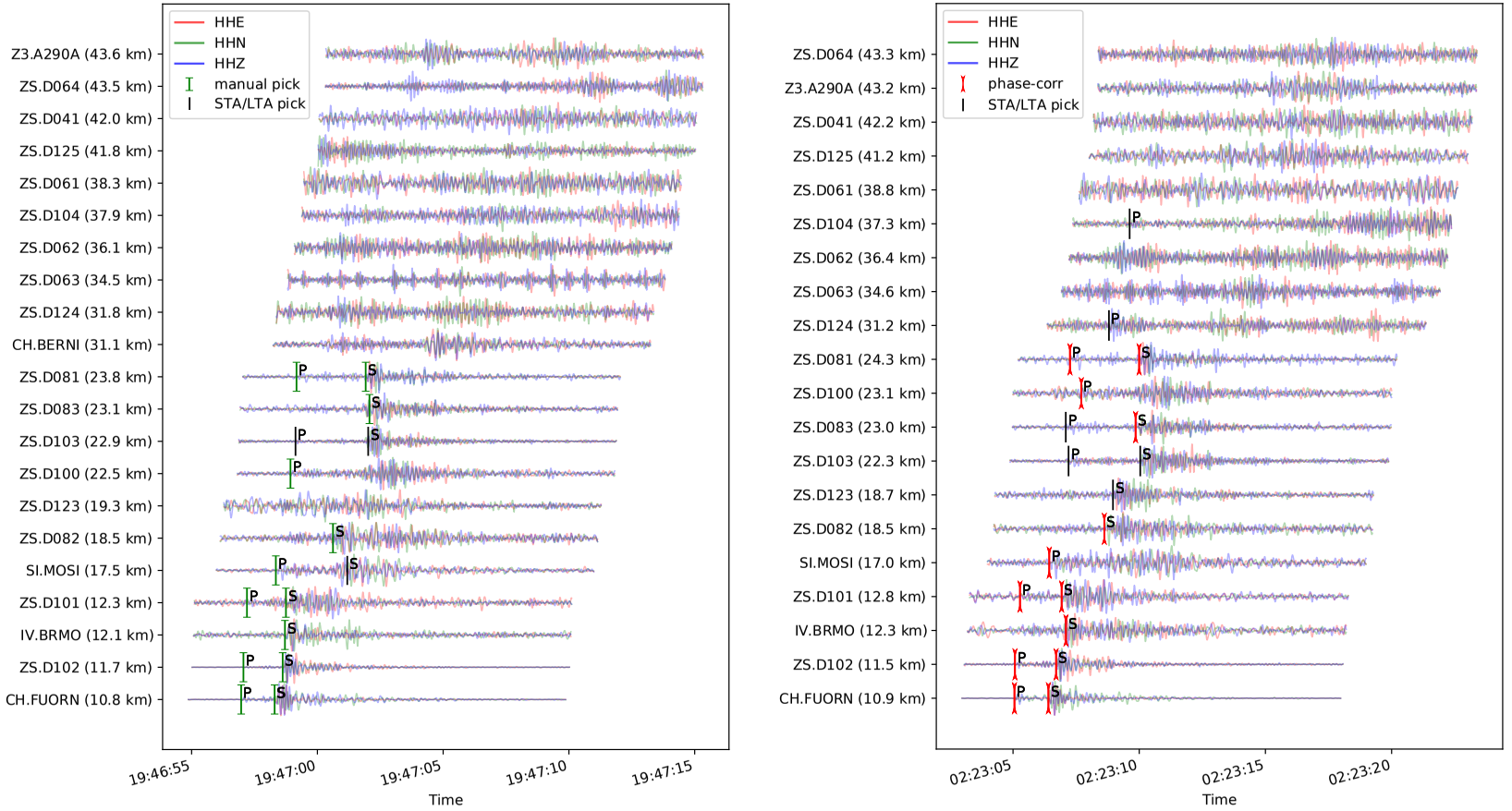

Figure 3.11. Example of the picking workflow described in this section. The left panel depicts the master event for a certain template family that was preliminarily located using 13 manual phase-picks. The right panel depicts an events from the template family containing phase-correlated picks for each of the master picks. Finally, both events contain additional STA/LTA based picks for channels with no available hand-pick. These events are located in the Münstertal valley in the Swiss Engadine Alps. The master event (-0.77 M_L) occurred on 24 February 2019 at 19:46:55 (UTC), the detected event (-0.87 M_L) occurred on 18 February 2019 at 02:23:02 (UTC).

3.2.3 Correlation based pick refinement

To further improve the precision of both the P- and S-picks, I implemented a technique described by Shearer (1997). It uses cross-correlation based differential times as well as absolute picks to invert for an optimised set of picks. Because a combination of picking methods was used, this eliminates systematic picking biases from the final set of picks. Whereas Shearer (1997) uses 3 s windows for both P- and S-picks and a 10 Hz low-pass filter, I decided to use the windows and band-pass filters shown in 3.1. The waveforms are resampled at 500 Hz to allow for a sub-sample precision of the cross-correlation function. Instead of cross-correlating all combinations of events, I used only onsets that were already picked.

Differential travel-times obtained from the cross-correlation lag times dt_{ij} and absolute phase-picks t_i within each template family are used to find an optimal set of picks T_i. The principle behind the optimisation is that for two phase-onsets T_1 and T_2, ideally we want T_1 to equal t_1, T_2 to equal t_2, and we also want dt_{12} to equal $T_2 - T_1$. This is an over-determined problem, because we have three equations to solve for two variables. For an event family with N events (if $N \geq 3$), we can rewrite the set of linear equations in the form of $\mathbf{d} = \mathbf{Gm}$ for each station-phase combination (Equation 3.4).

$$
\begin{pmatrix}
t_1 \\ t_2 \\ t_3 \\ \vdots \\ t_N \\ wcc_{12}\, dt_{12} \\ wcc_{13}\, dt_{13} \\ \vdots \\ wcc_{1N}\, dt_{1N} \\ wcc_{23}\, dt_{23} \\ \vdots \\ wcc_{(N-1)N}\, dt_{(N-1)N}
\end{pmatrix}
=
\begin{pmatrix}
1 & 0 & 0 & \cdots & & 0 \\
0 & 1 & 0 & & & \vdots \\
0 & 0 & 1 & & & \\
\vdots & & & \ddots & & \\
0 & & & & & 1 \\
wcc_{12} & -wcc_{12} & 0 & \cdots & & 0 \\
wcc_{13} & 0 & -wcc_{13} & & & \vdots \\
\vdots & & & \ddots & & \\
wcc_{1N} & 0 & \cdots & & & -wcc_{1N} \\
0 & wcc_{23} & -wcc_{23} & & & 0 \\
\vdots & \vdots & & \ddots & & \vdots \\
0 & \cdots & & & wcc_{(N-1)N} & -wcc_{(N-1)N}
\end{pmatrix}
\begin{pmatrix}
T_1 \\ T_2 \\ T_3 \\ \vdots \\ T_{N-1} \\ T_N
\end{pmatrix}
\tag{3.4}
$$

Where wcc_{ij} is a weighting factor. The least-squares solution to this set of equations can be approximated using an iterative solver, such as implemented in SciPy (Virtanen et al., 2020). After a solution has been found, the absolute phase-picks t_i are substituted by T_i. This changes the cross-correlation windows and hence the lag times. By iterating this process, t_i and T_i converge. I used a maximum of

15 iterations, exiting when the difference between t_i and T_i falls below the sample interval. To avoid using large numbers in the inversion, the absolute picks t_i are measured relative to the origin time of event i, and the cross-correlation lag times dt_{ij} are corrected for the origin time difference between event i and j.

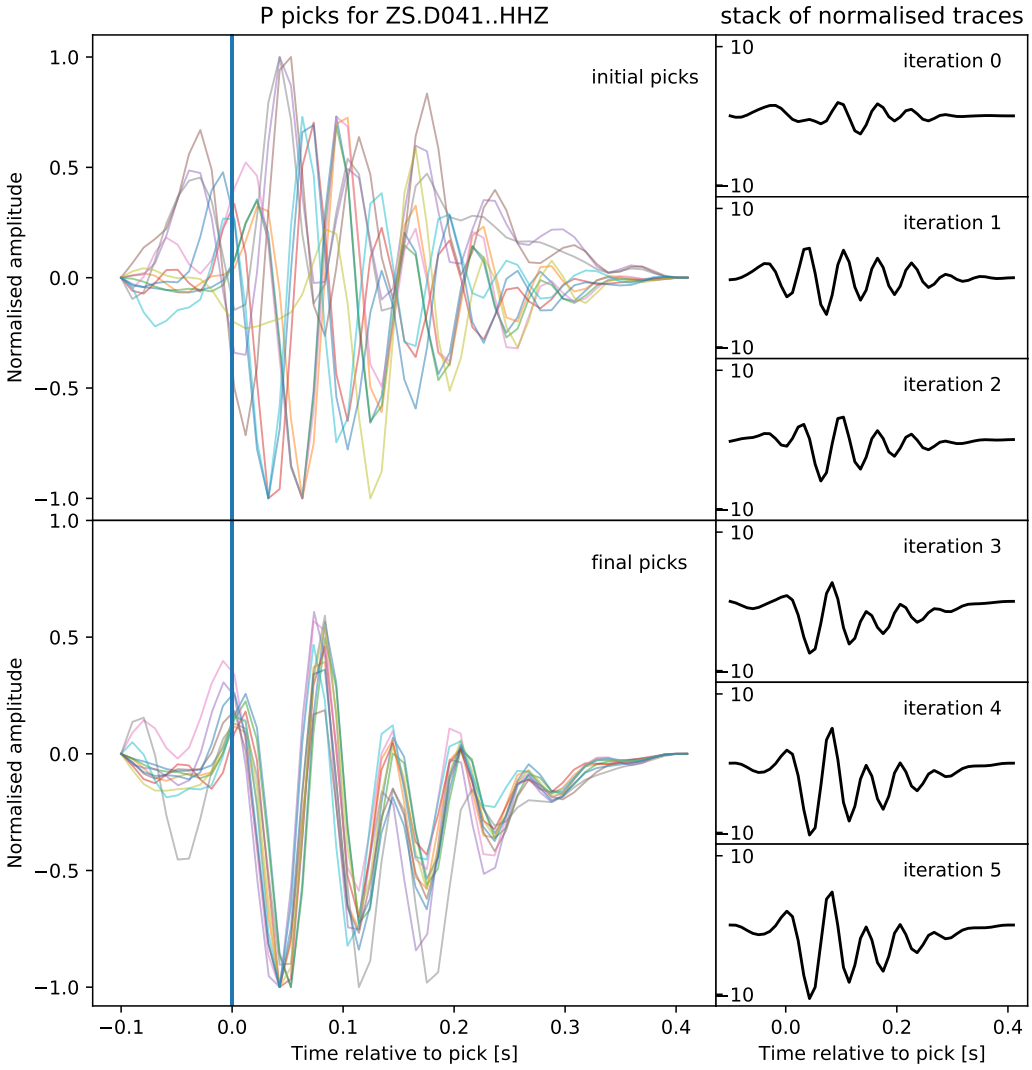

Figure 3.12. Demonstration of the pick-optimisation method described in this section. Waveforms in the upper panel are aligned by the original P-picks t_i, waveforms in the lower panel are aligned by the optimal set of P-picks T_i. The improvement can be seen visually and will result in more precise and consistent event locations.

The use of cross-correlation lag times for poorly correlated phases should be avoided. I therefore implemented a weighting factor wcc_{ij} that is either 1 if $cc_{ij} \geq 0.7$ or else 0.

For each event family, station and seismic phase (both P- and S), we repeat

the inversion for a maximum of 15 times, or until the solution converges, and obtain collectively a more consistent set of P- & S-arrival time picks. The effect of the method is illustrated exemplarily for one event family and one station in Figure 3.12. Examples of event waveforms with picks are provided in appendix Figures A11-A14, where Figures A11 and A13 are examples of relatively large earthquakes within the studied time window (magnitudes 1.3 M_L and 1.1 M_L respectively), and Figures A12 and A14 show very small magnitude earthquakes near the detection limit (both have a magnitude of -1.1 M_L).

3.3 Event localisation

3.3.1 Location inversion

The final set of P- and S-picks is then inverted for event locations and origin times within a local 3-D seismic velocity model by Jozi Najafabadi, Haberland, Le Breton, et al. (2022) using NonLinLoc (Lomax et al., 2000). Three longitudinal profiles of the velocity model are shown in Figure 3.13.

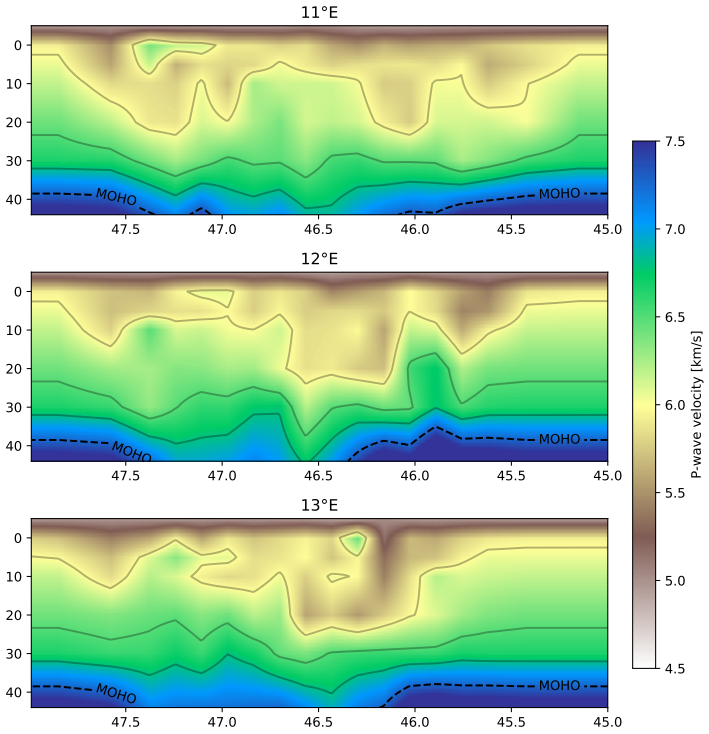

Figure 3.13. Three longitudinal profiles of the 3-D seismic P-wave velocity model by Jozi Najafabadi, Haberland, Le Breton, et al. (2022) that was used for the location inversion.

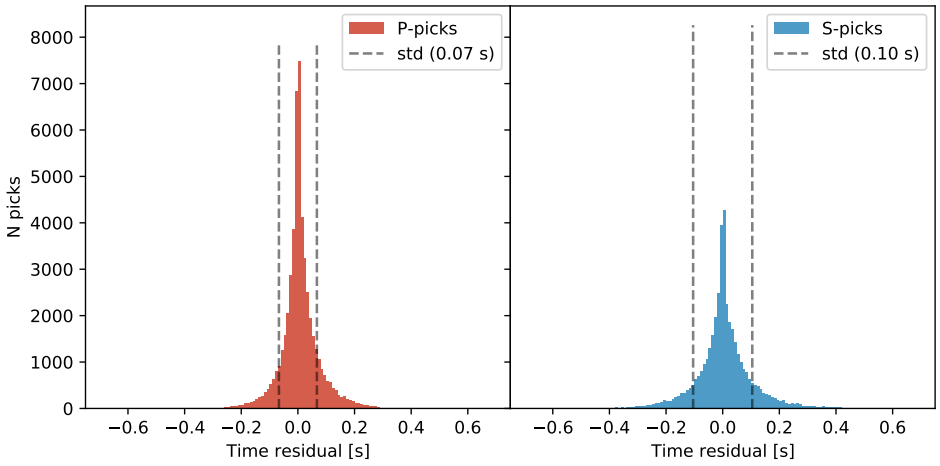

Figure 3.14. Residuals for all picks in the final catalogue.

To achieve optimal results, the inversion process is carried out in multiple decisive steps. Anomalous picks are promptly removed from the catalogue based on the residuals after each step. A maximum absolute residual of 300 ms with respect to the mean station residual is allowed for each individual pick. For an event, the RMS of the residuals is limited to 250 ms, and a minimum of 6 picks is required. These criteria reduce the number of events in the catalogue, but improve the quality of the locations. The final catalogue contains 93,576 picks for 7,756 events. The residuals (shown in Figure 3.14) are normally distributed with standard deviations of 0.07 s and 0.10 s for P- and S-picks respectively.

For each template family, I calculated the horizontal and vertical distance from the master event hypocentre to all other hypocentres. The result is shown as a function of the cross-correlation coefficient (CC) in Figure 3.15, where CC is defined as the median of the three highest cross-correlation coefficients of the event pair.

This result confirms the assumption that the waveform similarity is inversely related to the inter-event distance within template families. Whereas event pairs with $CC \geq 0.5$ may have horizontal inter-event distances of up to 10 km, event pairs with $CC \geq 0.9$ are located mostly within 1 km horizontal and 1.5 km vertical distance from the master events. Appendix Figures A5 and A6 show examples of both cases: the event pair in Figure A5 ($CC = 0.53$) has an inter-event distance of 5.91 km, whereas the event pair in Figure A6 ($CC = 0.99$) has an inter-event distance of 0.05 km. If we assert that all $CC \geq 0.9$ event pairs should in fact be exactly co-located, we can interpret the upper bound for the location uncertainty to be about 1 km horizontally and 1.5 km vertically.

To further assess the location uncertainties, I analysed the directionality of all of the event offsets with respect to the master events. Figure 3.16 depicts a

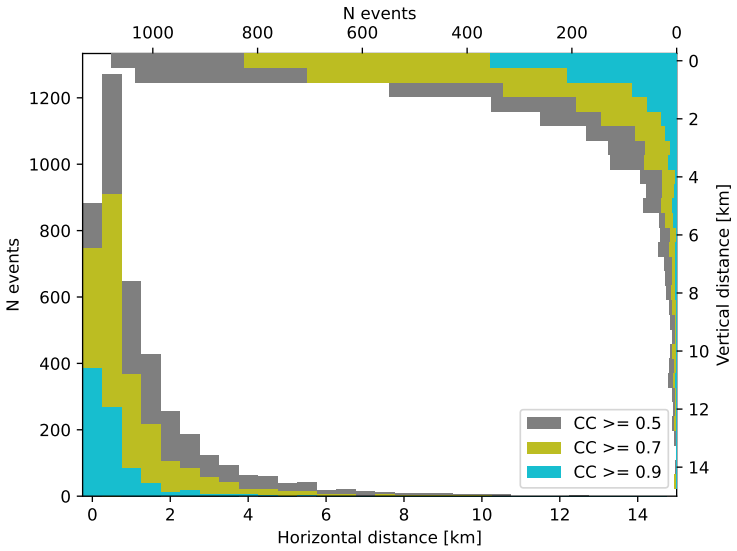

Figure 3.15. Horizontal and vertical distance of all events relative to their master events. The CC value is defined as the median of the three highest maximum cross-correlation coefficients of the 15 stations closest to each event pair. This figure appeared in Hofman, Kummerow, and Cesca (2023).

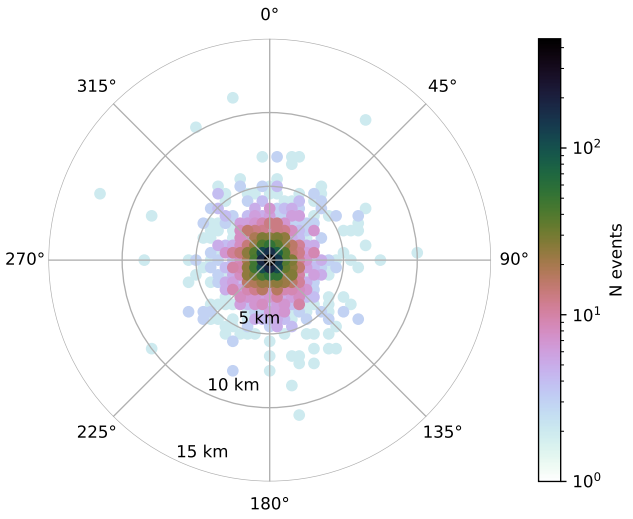

Figure 3.16. Event offsets with respect to the master events in polar coordinates. The hypocentral distance is calculated in 3D. This figure appeared in Hofman, Kummerow, and Cesca (2023).

histogram in polar coordinates illustrating the azimuth and hypocentral distance of the detected events relative to the master events. This result shows that there is no preferential direction of scattering, which could indicate a bias in the localisation workflow. The events scatter equally in all directions, and the majority of the events are located within a 1 km radius from the master event. Events located farther than 5 km from their master event are very rare, and events farther than 10 km are most probably erroneously located.

CHAPTER 4

Event classification

A known challenge with the detection of low magnitude seismicity is the concurrent recording of anthropogenic signals. If such events are mistaken for earthquakes, this could lead to wrong interpretations of the seismicity. One common example is that anthropogenic events skew the magnitude frequency distribution. Because the signals are often repetitive and of the same (low) magnitude, the b-value of the Gutenberg-Richter relation (Gutenberg and Richter, 1944) will be overestimated. The Eastern Alps are especially sensitive to this problem because of the high population density and industrial activity, in combination with the shallow, low-magnitude seismicity (Peruzza et al., 2015).

The differentiation of anthropogenic signals from earthquakes is not trivial, as explosion signals such as quarry and mine blasts can be hard to distinguish from earthquake signals. In theory, explosion signals can be recognised from their waveform recordings because they show a positive P-phase onset in all azimuthal directions. In practice, however, the signal to noise ratio is often insufficient to clearly determine the first onset, and the station availability does not always allow a complete azimuthal coverage. Automatic classification of seismic events or even discrimination into two groups based on waveform attributes proves to be a difficult challenge to date (e.g. Mousavi et al., 2016; Reynen and Audet, 2017). I performed a feasibility study on the automatic classification of events based on waveform attributes and principal component analysis (PCA), which I describe in Section 4.1. I finally adopted a more straightforward method using the origin time distributions as described in Section 4.2.

4.1 Classification based on waveform attributes

Several studies have shown the applicability of machine learning based classifiers to discriminate between small earthquakes and quarry blasts (e.g. Kuyuk et al., 2011; Mousavi et al., 2016; Reynen and Audet, 2017; Shang et al., 2017). To test the feasibility of applying such an approach, I created three small labelled datasets containing tectonic earthquakes and quarry blasts. For a selection of events, three-component waveforms with a length of 10 s were extracted on nearby stations. A number of attributes (also features) were calculated from these waveforms both in the time-domain, as well as using the continuous wavelet transform (CWT) as defined in Kristeková et al. (2009). A selection of the features tested can be found in Table 4.1. The three datasets are defined as follows: **dataset 1** contains events from a single earthquake cluster and events from a single quarry. Waveforms are extracted for a single station in each of the two event classes; **dataset 2** contains events from a single earthquake cluster and events from a single quarry. Waveforms are extracted for multiple stations in each of the two event classes; **dataset 3** contains events from multiple earthquake clusters and events from multiple quarries. Waveforms are extracted for multiple stations in each of the two event classes.

Feature #	**Description**	**Components**
$[1, 5, 9]$	Maximum absolute amplitude	$[N, Z, E]$
$[2, 6, 10]$	Peak frequency	$[N, Z, E]$
$[3, 7, 11]$	Spectral width (sum of normalised spectrum)	$[N, Z, E]$
$[13]$	N. of sidelobes in the autocorrelation function	$[Z]$
$[14]$	Skewness of the autocorrelation function	$[Z]$
$[15]$	Incidence angle, first motion polarisation	$[N + Z + E]$

Table 4.1. Selection of waveform attributes calculated for each dataset. The attributes for all waveforms in dataset 1 are shown in Figure 4.1.

A scatter matrix of a selection of waveform attributes for dataset 1 is shown in Figure 4.1. The attributes listed in Table 4.1 are represented as rows and columns, so that each off-diagonal subfigure shows the values of one attribute plotted against one other attribute. The diagonal shows the distribution of the values for each individual attribute. This representation helps to identify attributes that work well to separate the classes, as well as to recognise the dependencies of attributes. For example the features numbered 5 and 9 show a clear linear dependency, which is not surprising because the maximum amplitude on the different channels are obviously not completely independent. It can also be seen that multiple attributes, for example 2, 10, and 13, separate the classes very well.

One can imagine looking at this feature space and finding the combination of the two attributes that separates the data best. This information could then

be used to classify events. Unfortunately, this would require dismissing a lot of attributes, and losing valuable information. A more optimal strategy is to reduce the dimensionality of the feature space, also known as principal component analysis (PCA). Rather than creating 15 x 15 subfigures, imagine combining all attributes into a single point cloud with 15 dimensions. We then search for the vector within this space, along which our cloud is best separated. Mathematically, this vector is an eigenvector of the covariance matrix that corresponds to the largest eigenvalue. This vector will be the first principal component. We can search for the next best vector that is orthogonal to the previous one to find any number of principal components up to the initial number of dimensions. As in most machine learning applications, all attributes must be scaled beforehand to ensure that they are weighed more or less equally. This is done by removing the mean and normalising to unit variance. Both the scaling and the PCA are conveniently implemented in Python using the Scikit-Learn package (Pedregosa et al., 2011).

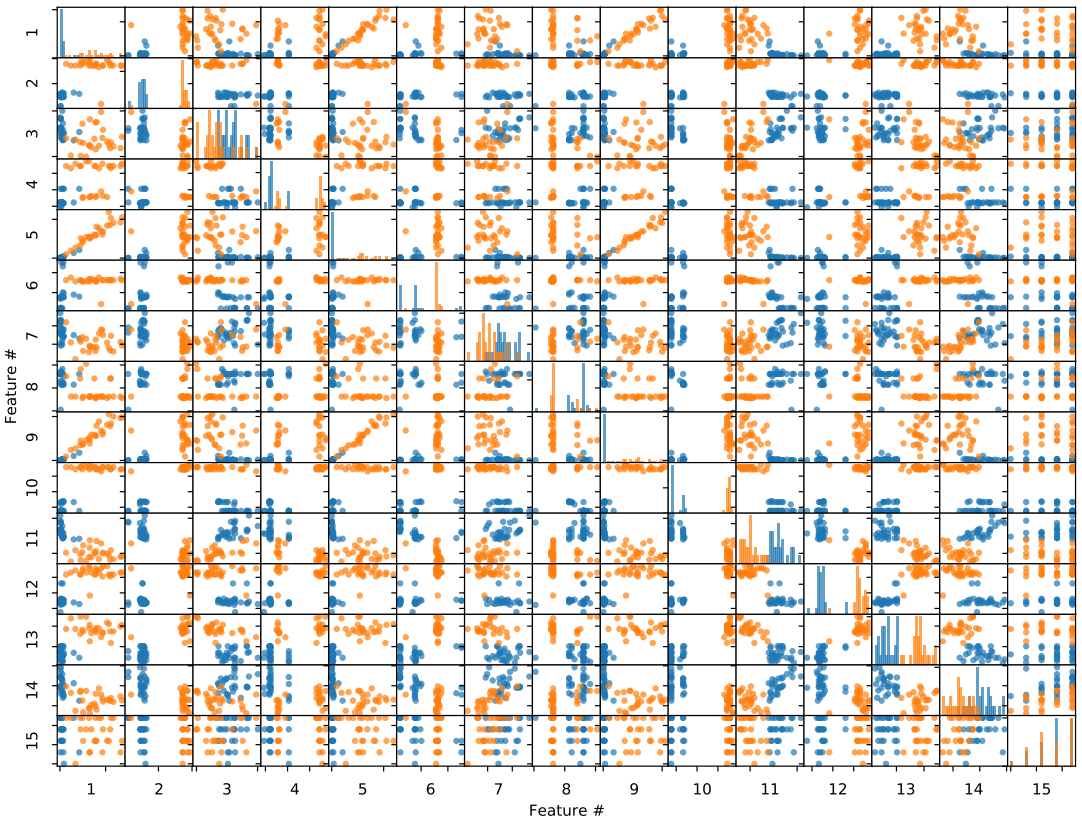

Figure 4.1. Scatter matrix of a selection of waveform attributes for a labelled set of seismic events. On the off-diagonal subfigures, the row attribute i is plotted against the column attribute j, the diagonal subfigures show a histogram of the distribution for attribute i. The attribute numbers are explained in Table 4.1. Tectonic earthquakes are shown in blue, quarry blasts are shown in orange.

Figure 4.2 shows the results of the PCA for the three datasets described in this section. It can be seen that for dataset 1, the first principal component perfectly separates the two classes, confirming that the selected attributes are very well suited to discriminate between the two event types. In dataset 2, part of this effect remains, as the centre of mass for both classes are still separated, but there is a significant overlap. In dataset 3, the first two principal components do not separate the classes at all. The result from dataset 1 shows that there is a potential for using this technique to classify seismic events based on waveform attributes. As the complexity of the dataset is increased by introducing multiple stations (dataset 2), and multiple sources (dataset 3), the separation effect fades. This indicates that the difference in the selected waveform attributes between both classes is not a first order effect, and that the variation between stations and source locations is greater. These principal components can be used as input variables to train an artificial neural network (ANN) to distinguish between the classes, as shown for example by Reynen and Audet (2017) and Shang et al. (2017). However, this would require much larger labelled datasets that can be split into training and test data, implying that some other method has to be applied to classify the events before the model can be trained.

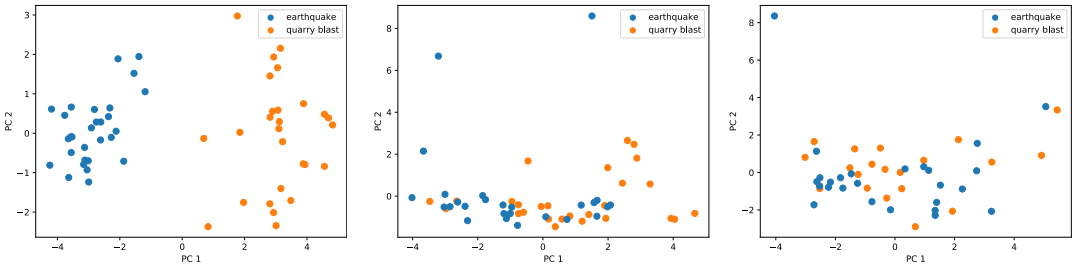

Figure 4.2. Reduced feature space of the principal component analysis (PCA) of waveform attribute for three different labelled dataset of tectonic earthquakes (blue) and quarry blasts (orange). The left panel shows the result for dataset 1, the middle panel show the result for dataset 2, and the right panel shows the result for dataset 3.

4.2 Spatio-temporal event classification

A completely different way of identifying quarry and mine blasts in a seismicity catalogue was proposed by Wiemer and Baer (2000). The authors identify areas that suffer from quarry contamination by mapping the ratio of daytime to nighttime events. This makes use of the fact that explosions are set off during daytime hours, whereas tectonic earthquakes should be equally distributed over day- and nighttime hours. The authors then proceed to remove all daytime events in areas that have a high probability of quarry contamination. Although very effective,

this method has a few downsides: (1) all tectonic earthquakes during daytime hours in the affected area are removed; (2) aftershock series or earthquake swarms during daytime hours can lead to false positives; and (3) the sensitivity depends on the background seismic rate.

My workflow for the detection of quarry and mine blasts makes use of the additional information that is provided by the template matching algorithm (see Section 3.1). Because detections are co-located with their template event and also have a similar source mechanism, they are very likely to be of the same event type. If a quarry blast event is used as a template, its detections will also be quarry blasts. By analysing the temporal patterns within each template family, these can easily be identified. Most indicative is the distribution of event origin times over the days of the week, as well as their distribution over the hours of the day. Quarry blasts set off exclusively during daytime hours, mostly on weekdays –never on Sundays. In most quarries, explosions are detonated at predetermined times, often twice per day, once around noon and once in the afternoon. One example of such a template family is shown in Figure 4.3. The origin times should be converted to the local time zone to correctly interpret daytime and nighttime hours. I also analysed the dates of all events in each template family. If all events occur on a single day, the possibility of an earthquake swarm or aftershock series should be considered. Finally, since accurate event locations are available for the catalogue, I plotted the event locations over a satellite image to see if the presence of a quarry or mine could be confirmed.

Although some manual work was required, this workflow allowed me to accurately classify the events in the seismicity catalogue. Figure 4.4 shows the temporal patterns for all anthropogenic events, as well as for the remaining set of tectonic events. A clear anti-correlation can be seen between both sets, indicating that the sensitivity to small magnitude earthquakes decreases during the daytime hours as noise levels from anthropogenic activity increase. This effect can also be seen when comparing the weekdays to weekend days. Despite the majority of quarries performing detonations at predefined hours, such as in the example in Figure 4.3, there is no discernible pattern of increased explosions at either full or half-hour intervals. The monthly rate of anthropogenic events shows a seasonal variation, with slightly more activity in the summer months compared to the winter months. The monthly earthquake rate is mainly dominated by a few large earthquake clusters, as can also bee seen in Figure 3.8.

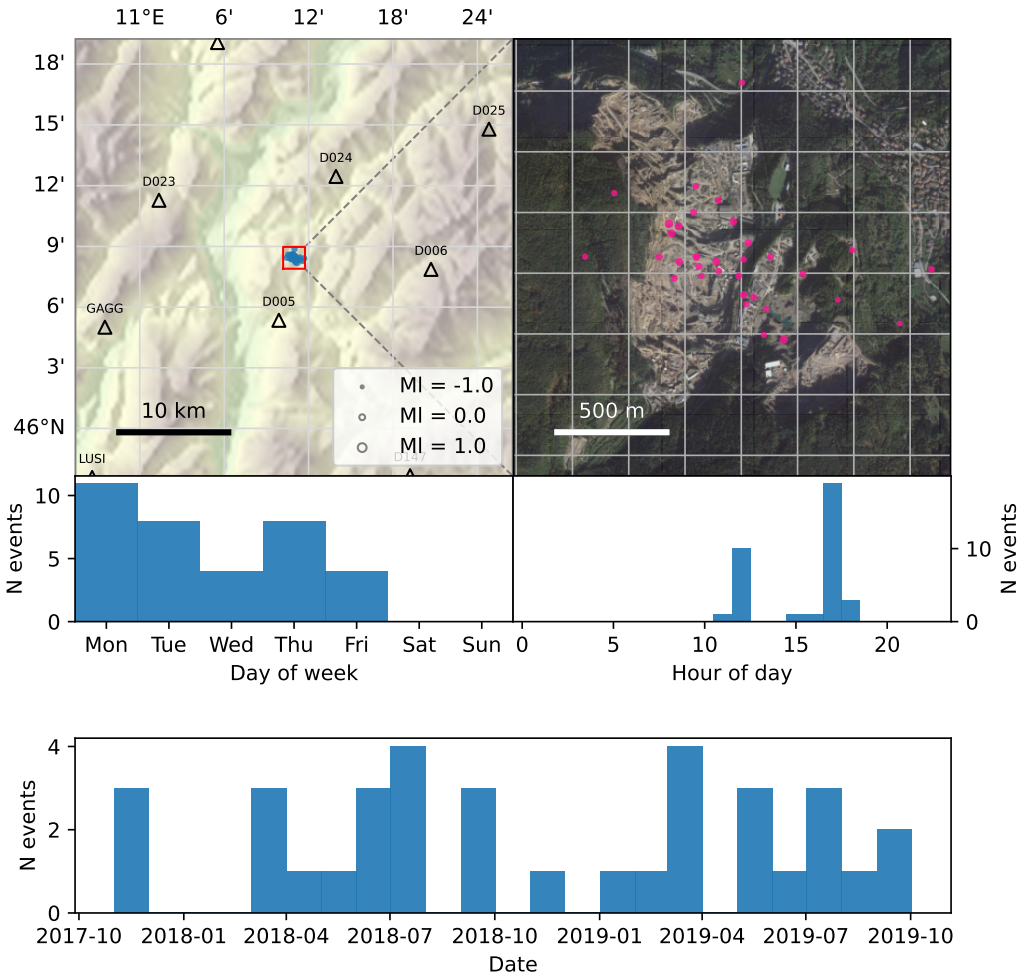

Figure 4.3. Example of a positive identification of quarry blast events in the Trentino Porphyry Quarry District in Albiano, Italy. The upper half of the figure shows a map view of the event locations with an overview of the area (upper left), and a zoomed-in view with a satellite image as background (Google, ©2023 Maxar Technologies) (upper right). The lower half of the figure is dedicated to the most important temporal signatures, showing histograms of the weekdays, time of day, and a monthly event rate over the entire recording period.

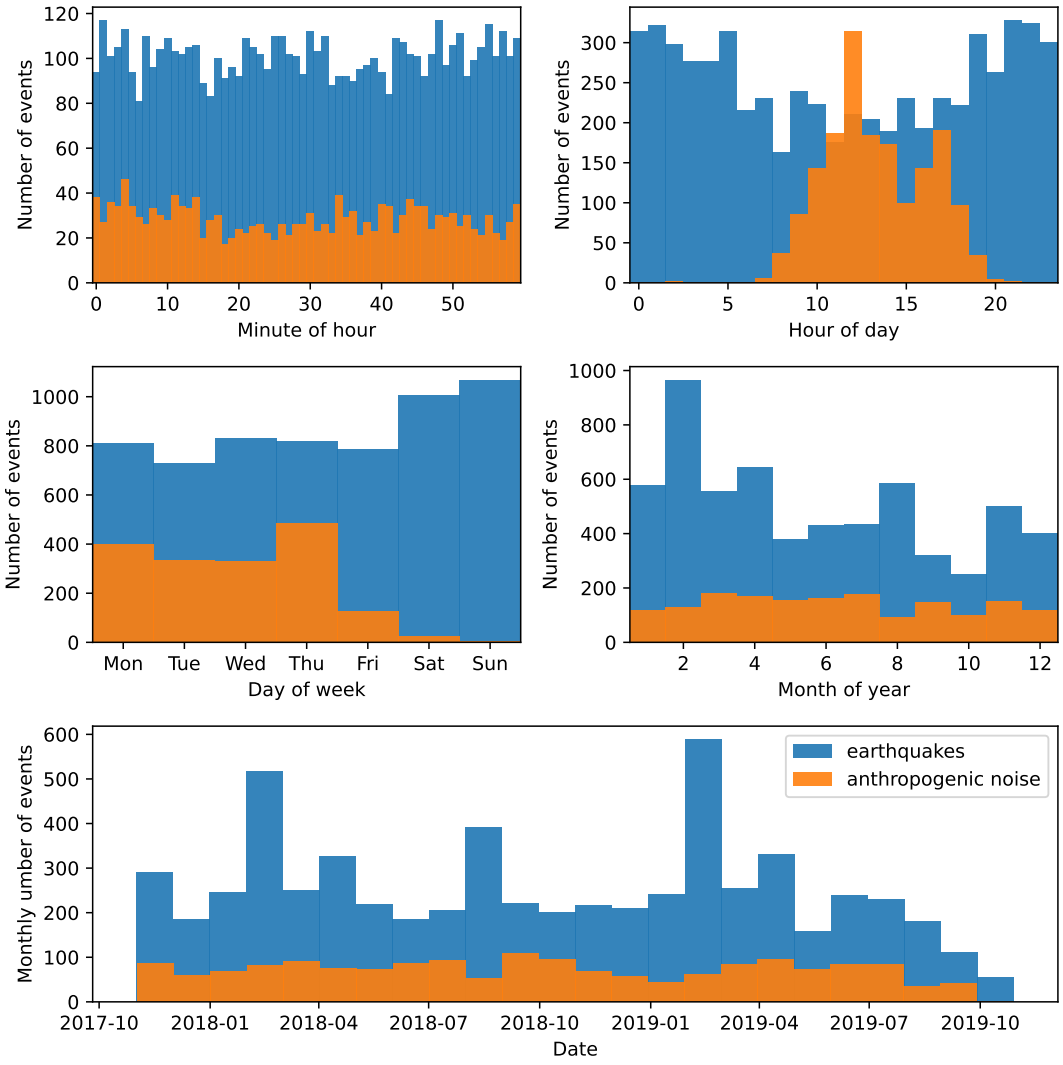

Figure 4.4. Temporal patterns of the set of identified quarry and mine blasts (anthropogenic noise) in orange, and the remaining catalogue of tectonic earthquakes in blue.

CHAPTER 5

Event magnitudes

5.1 Introduction

Historically, the size of an earthquake was measured in *intensities*. The intensity of an earthquake is based on macroseismic observations such as reports by people, and damage to buildings and landscapes. This method is still used today to estimate the size of historical earthquakes (see also Section 1.3). The magnitude scale was proposed by Richter (1935) to be able to quantitatively compare earthquake sizes at different locations. Instead of relying on observations of the effects of an earthquake at a particular location, the energy of the earthquake at its source is estimated based on the maximum amplitude of the seismograph recording and the distance. This magnitude type is still used today and known as the local magnitude M_L.

A multitude of magnitude types were introduced in the following decades to extend the applicability to more general cases. The methods of calculation are all similar to the local magnitude, but the amplitude is derived from specific seismic phases. Because the phases that arrive at a seismograph vary with source distance and depth, and phase amplitudes saturate at a certain magnitude, these methods all have different use cases. Today, the preferable method for measuring the size of an earthquake is the moment magnitude M_w (Hanks and Kanamori, 1979). This magnitude is calculated from the seismic moment rather than from the amplitudes of specific phase-arrivals. However, local earthquake agencies do

not routinely calculate M_w for earthquakes smaller than M_w 3.5 due to technical challenges. Petersen, Cesca, Heimann, et al. (2021) calculated moment tensor inversions for the wider Alpine region using data from the Swath-D network. Only 13 events overlap between our datasets, all in the magnitude range of M_w 3.3 to M_w 3.8, which are the largest events in my catalogue.

5.2 Calculation of local magnitudes

I calculated magnitudes for all of the relocated events in the local magnitude (M_L) scale (Richter, 1935) using the equation proposed by Bakun and Joyner (1984):

$$M_L = \log_{10}(A) + n\log_{10}(R/100) + k(R-100) + 3 + S \tag{5.1}$$

where R is the distance from the earthquake hypocentre to the seismograph in km, n is a parameter characterising the geometrical spreading, k is a parameter characterising the elastic attenuation of S-waves, and S is a station correction term. Finally, A is the geometric mean in millimetres of the zero-to-peak S-wave amplitudes on the horizontal channels of a Wood-Anderson seismograph (the original seismograph used by Richter, 1935). To calculate the amplitudes, I removed the original instrument response from the data and simulated the instrument response of the Wood-Anderson seismograph. Values for n and k for northeastern Italy were calculated by Bragato and Tento (2005), as shown in Table 5.1.

Distance [km]	n	k
10-40	1	0.0169
40-80	1	0.0064
80-120	0.5	0.0000
120-170	1	0.0009
170-250	1	0.0027

Table 5.1. Parameters n and k for north eastern Italy as determined by Bragato and Tento (2005).

Firstly, I calculated local magnitudes using equation 5.1 for the subset of master events without the station correction term S. This allows me to get an estimate of the earthquake magnitude for each station that has an S-pick. I refer to these magnitude estimates as the station magnitudes. The event magnitude is then defined as the median of the station magnitudes. Station correction terms are then applied to compensate for the average deviation from the event magnitudes. Using the master event subset ensures a more uniform spatial sampling, thereby minimising the potential for bias caused by large event clusters. Using these

station corrections, I calculated magnitudes for all earthquakes.

Standard deviations are calculated from all station magnitudes corresponding to an event magnitude within 0.2-sized bins. Figure 5.1 shows that the average standard deviation of the station magnitudes is about 0.25, and decreases slightly for magnitudes above M_L 2.0. All station magnitudes are plotted in the background in light grey. The interference between ambient noise and earthquake signals increases as the magnitude decreases below M_L 0.0, resulting in the appearance of large outliers among the station magnitudes. The small standard deviations give the impression that the event magnitudes are still reliable. I use the median of the station magnitudes to calculate the event magnitude to reduce the sensitivity to outliers. Nonetheless, I expect that the lower end of the magnitude spectrum is slightly biased and that the magnitudes of the smallest events in the catalogue might be overestimated. I further discuss this topic in Appendix B.

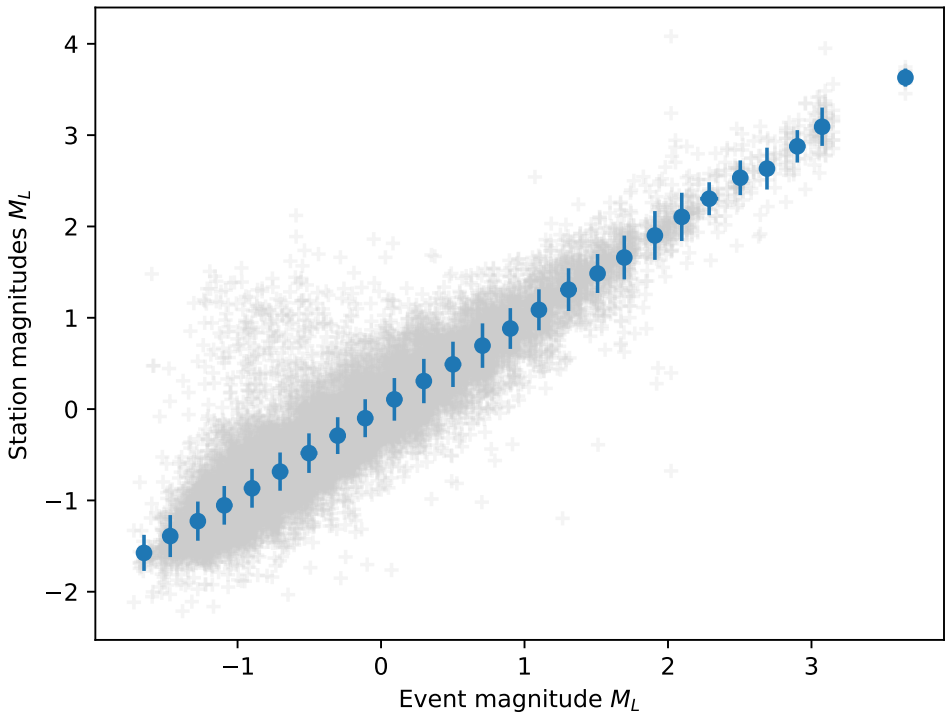

Figure 5.1. Average standard deviation of the station magnitudes (M_L) within each bin (of size 0.2). The binning is applied to the event magnitudes. The station magnitudes are plotted in light grey.

5.3 Magnitude frequency distribution and scaling with M_w

The magnitude frequency distribution (FMD) of earthquake catalogues can be described by the Gutenberg-Richter relation (Gutenberg and Richter, 1944):

$$\log N = a + bM \tag{5.2}$$

where N is the number of earthquakes with magnitude M or greater. Parameters a and b are estimated by fitting a line through the part of the frequency magnitude distribution above the completeness magnitude M_c, where the distribution becomes a log-linear. I achieved the most satisfying fit using the least-squares method, which I justify in more detail in Appendix B. To increase the statistical stability of the estimated parameters, es well as provide standard deviations, I performed a bootstrapping approach. For each FMD, I create an ensemble of 100 bootstrapped subsets by replacing 10% of the event magnitudes with randomly sampled magnitudes from the remaining distribution. From the ensemble, I calculate the mean values for a, b, and M_c and their standard deviations. Whereas a depends mainly on the number of earthquakes sampled, the b-value typically appoaches 1 when a large enough volume is sampled, where local deviations from this value are often attributed to physical characteristics such as stress conditions (Scholz, 2015), faulting style (Schorlemmer et al., 2005), the fractal dimension of fault planes (Hirata, 1989), and rock type (Scholz, 1968). An analysis of the earthquake magnitudes using the Gutenberg-Richter relation is shown in Figure 5.2. In this case, I expect the b-value to be close to one because a large area is sampled. I therefore attribute the low b-value of 0.70 to an underestimation of the seismic moment by the local magnitude scale. Other authors that studied magnitude frequency distributions in a similar range of extremely low magnitudes have observed this before (e.g. Deichmann, 2006; Bethmann et al., 2011; Munafò et al., 2016). To correct for this scaling problem, I estimated the moment magnitude M_w using the scaling relation proposed by Munafò et al. (2016), given by

$$M_w = 2/3 M_L + 1.5 \tag{5.3}$$

Applying Equation 5.3, produces a more common b-value of 1.05.

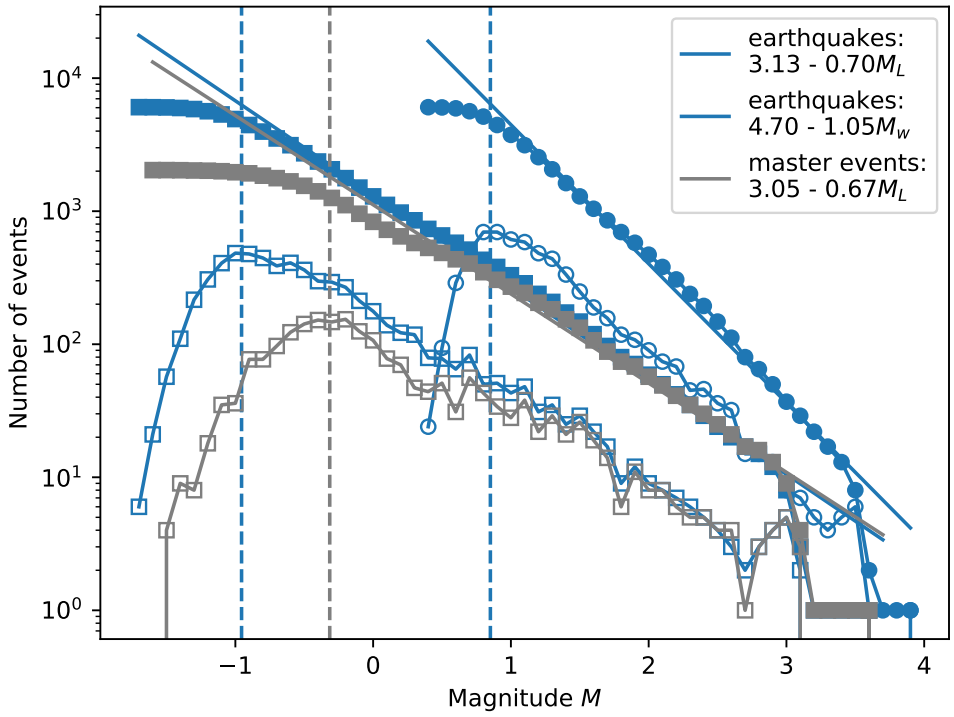

Figure 5.2. Magnitude frequency distribution of the input catalogue (grey squares) and the final earthquake catalogue (blue squares) in the local magnitude scale (M_L), as well the estimated moment magnitude (M_w) using the scaling relation (Equation 5.3) by Munafò et al. (2016) (blue circles). Using a least-squares fit based on the estimated M_w, I obtain the values $a = 4.70 \pm 0.10$ and $b = 1.05 \pm 0.06$ for the Gutenberg-Richter relation (Gutenberg and Richter, 1944). The completeness magnitude M_c based on the maximum curvature of the FMD (Wiemer and Wyss, 2000) is M_L 1.0 (M_w 0.9).

CHAPTER 6

A seismicity catalogue for the Eastern Alps

In this Chapter, I present the final seismicity catalogue for the Eastern Alps, combining the results from Chapters 3, 4, and 5. The spatial distribution of events is displayed in Figure 6.1. The classification of earthquakes and anthropogenic events that is indicated by the blue and orange colours is described in Chapter 4. Chapter 5 describes the methods for calculating the local event magnitudes. Figure 6.2 presents depth profiles through key parts of the study area.

6.1 Spatial and temporal patterns in seismicity

The spatial distribution of the small magnitude seismicity that I detected between late 2017 and late 2019 mainly follows the patterns of larger sized earthquakes known from previous studies over longer time periods (e.g. Slejko et al., 1998; Reiter et al., 2018). The depth of the events is limited to about 20 km, with a strong concentration of seismicity between 8 km and 12 km. This shallow nature of the seismicity in the Eastern Alps is also described by other authors (e.g. Reinecker and Lenhardt, 1999; Viganò et al., 2015; Reiter et al., 2018; Jozi Najafabadi, Haberland, Ryberg, et al., 2021). A slight deepening of the seismicity can be observed towards the south beneath the Po-plain (profiles A, C, D in Figure 6.2), and towards the north-west beneath the Engadine and Ortler Alps (profile B in Figure 6.2).

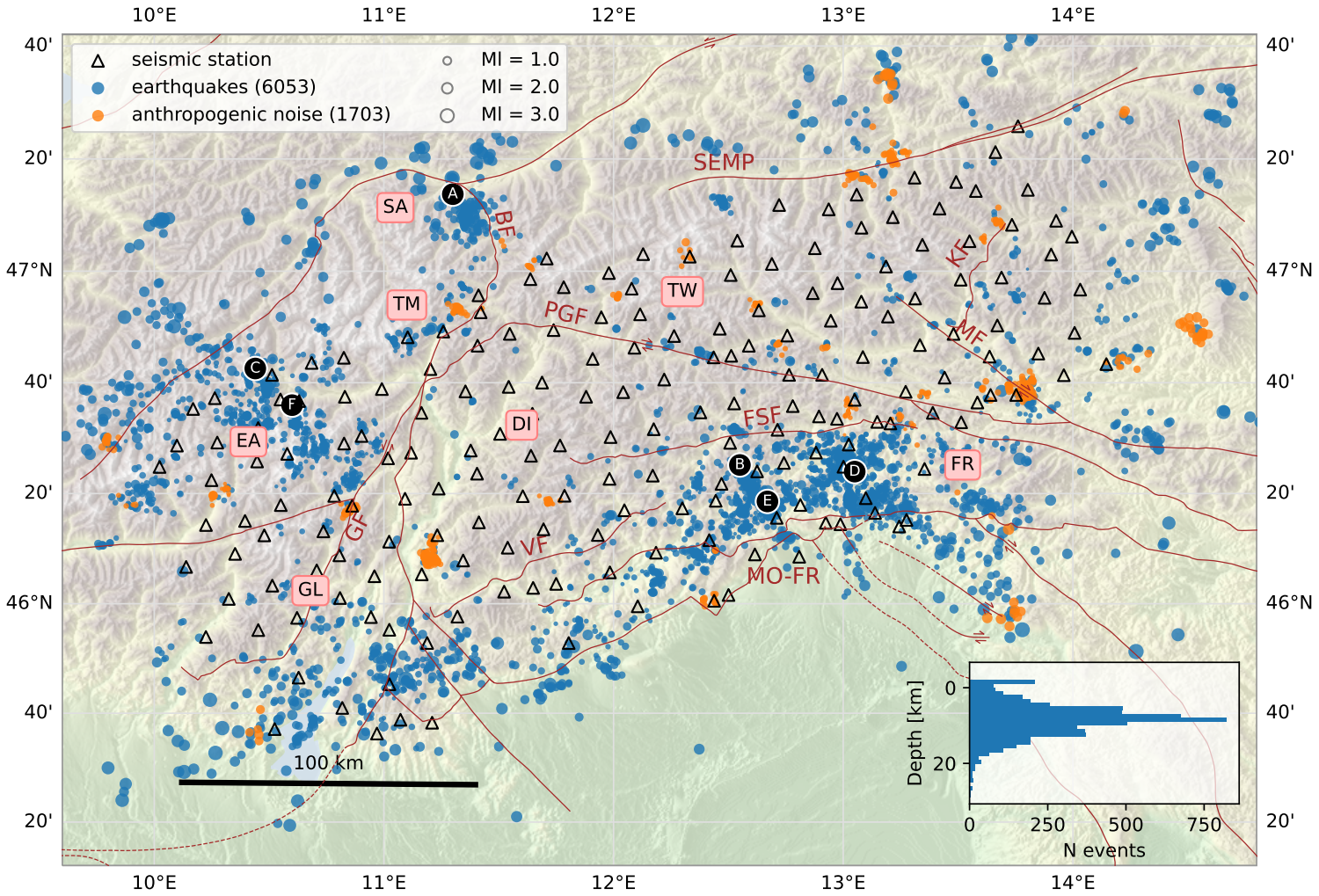

Figure 6.1. Seismicity in the Eastern Alps between late 2017 and late 2019. Symbols $A - F$ mark the locations of earthquake sequences indicated in Figure 3.8. Major faults from Schmid, Fügenschuh, et al. (2004) (red lines) are BF: Brenner Fault, FSF: Fella-Sava Fault, GF: Giudicarie Fault, KF: Katschberg Fault, MO-FR: Montello-Friuli thrust belt, MF: Mölltal Fault, PGF: Pustertal-Gailtal Fault, SEMP: Salzach-Enns-Mariazell-Puchberg Fault, VF: Valsugana Fault. Tectonic units after Reiter et al. (2018) are DI: Dolomite Indenter, EA: Engadine and Ortler Alps, FR: Friuli, GL: Giudicarie-Lessini region, SA: Stubai Alps, TM: Texel Group and Meran-Passeier area, TW: Tauern Window.

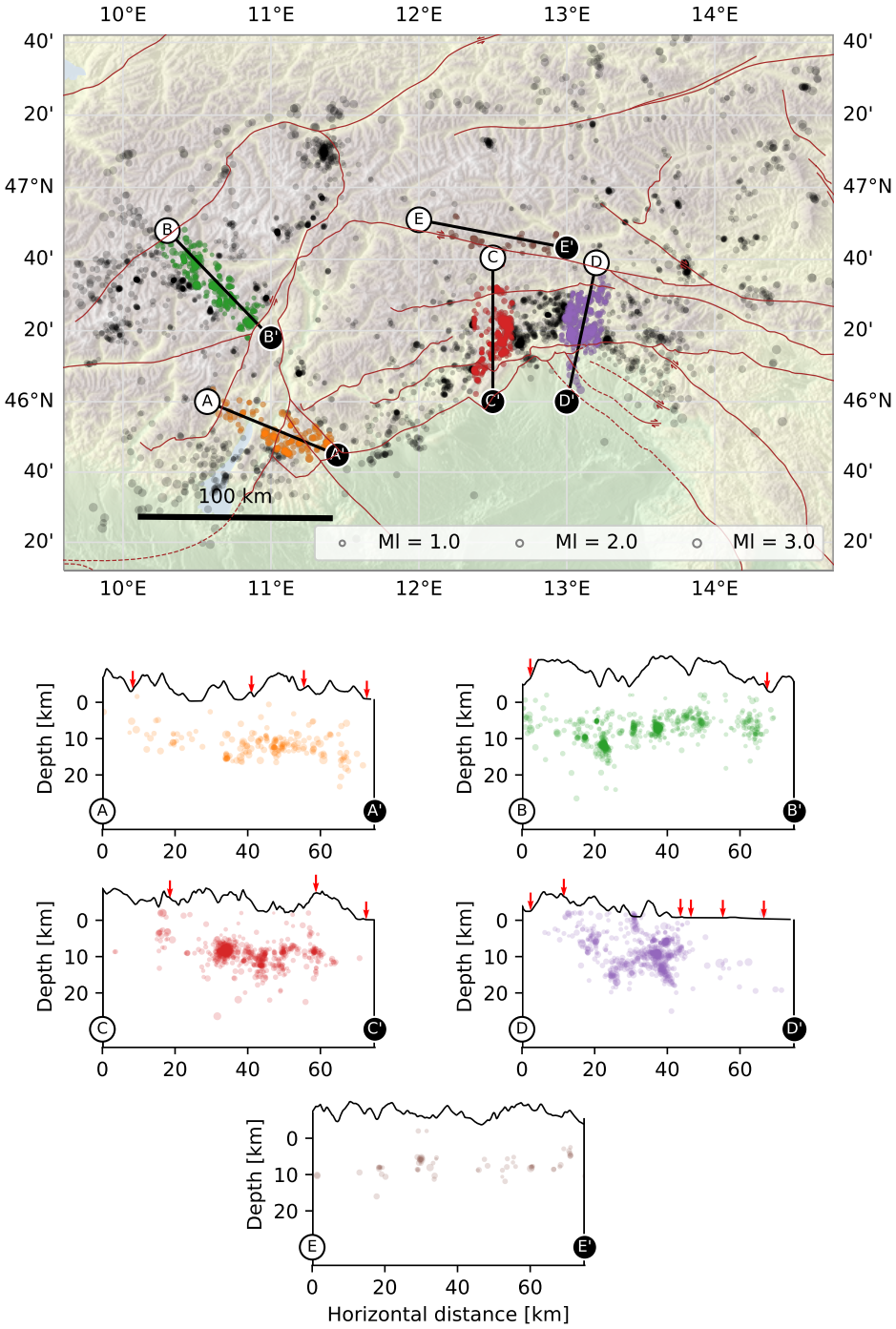

Figure 6.2. Depth profiles of the seismicity catalogue in A: the Giudicarie-Lessini region, B: the Engadine and Ortler Alps, C: the central Dolomites, D: the Fruili region, E: along the Pustertal-Gailtal Fault. The colours help to differentiate the profiles, and indicate which events are used. Intersecting faults are shown as red arrows on the profiles. Topography (4x exaggerated) was extracted from the ETOPO 2022 global relief model (NOAA National Centers for Environmental Information, 2022).

Friuli region

The Montello-Friuli fold- and thrust belt in the Friuli region exhibits the highest seismicity rates of the study area (Romano et al., 2019; Bragato, Comelli, et al., 2021). This region is known to absorb most of the NNW movement of the Adriatic plate with respect to the European plate and marks the southern border of the Dolomite indenter – the part of the Adriatic crust with little internal deformation (Castellarin et al., 2006; Cheloni et al., 2014; Serpelloni et al., 2016; Reiter et al., 2018; Petersen, Cesca, Heimann, et al., 2021). This area also produced the largest recent earthquake in the wider Alpine region, the 1976 M_w6.4 Friuli earthquake (e.g. Slejko, 2018; Aoudia et al., 2000), as well as other historical $M \geq 6$ earthquakes (see Section 1.3 for an overview of the historical seismicity). Known focal mechanisms for the larger events in this region show mainly ENE–WSW striking thrust faulting, with a smaller number of strike-slip events (Petersen, Cesca, Heimann, et al., 2021).

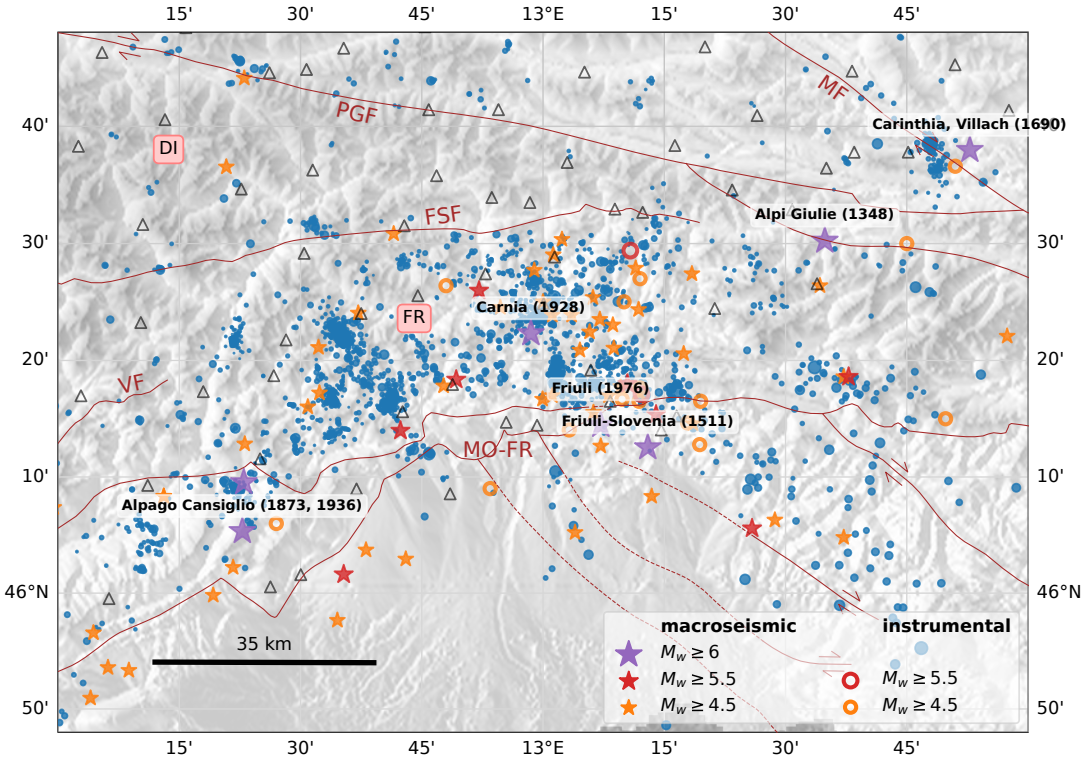

Figure 6.3. Detailed view of the seismicity in the Friuli region (blue circles). The historical earthquakes shown on this map are from Rovida et al. (2022). Major faults from Schmid, Fügenschuh, et al. (2004) (red lines) are FSF: Fella-Sava Fault, MO-FR: Montello-Friuli thrust belt, MF: Mölltal Fault, PGF: Pustertal-Gailtal Fault, VF: Valsugana Fault. Tectonic units after Reiter et al. (2018) are DI: Dolomite Indenter, FR: Friuli.

Profile D in Figure 6.2 shows that seismicity within the fold- and thrust belt reaches from a depth of about 20 km all the way to the surface. The event density abruptly drops at the transition to the Po-plain towards the south, where the depth of seismicity is limited to the depth range of 10-20 km, and more shallow events are absent. Towards the north, seismic activity is truncated by the Valsugana and Fella-Sava faults. Seismicity in the Friuli region is strongly clustered, the largest of which are indicated in Figure 6.1 with symbols B, D, and E. These clusters are discussed in more detail in Chapter 7. A detailed map of the seismicity catalogue of this area is presented in Figure 6.3.

Dolomite indenter

Within the Dolomite indenter, seismic activity is very sparse. This absence of seismicity in this area coincides with high Rayleigh wave velocities at seismogenic depths of 10 to 20 km (Sadeghi-Bagherabadi et al., 2021; Kästle, Molinari, et al., 2021). Jozi Najafabadi, Haberland, Handy, et al. (2023) found that the Dolomite indenter is characterised by an exceptionally low P-wave attenuation. This supports the notion that the crust is especially dense and rigid in this area. Nevertheless, I was able to relocate about 100 events thanks to the dense station configuration of the Swath-D network. The magnitude of these events is generally below $M_L 1$, with the exception of two events along the Fella-Sava Fault. A detailed map of the seismicity catalogue of this area is presented in Figure 6.4.

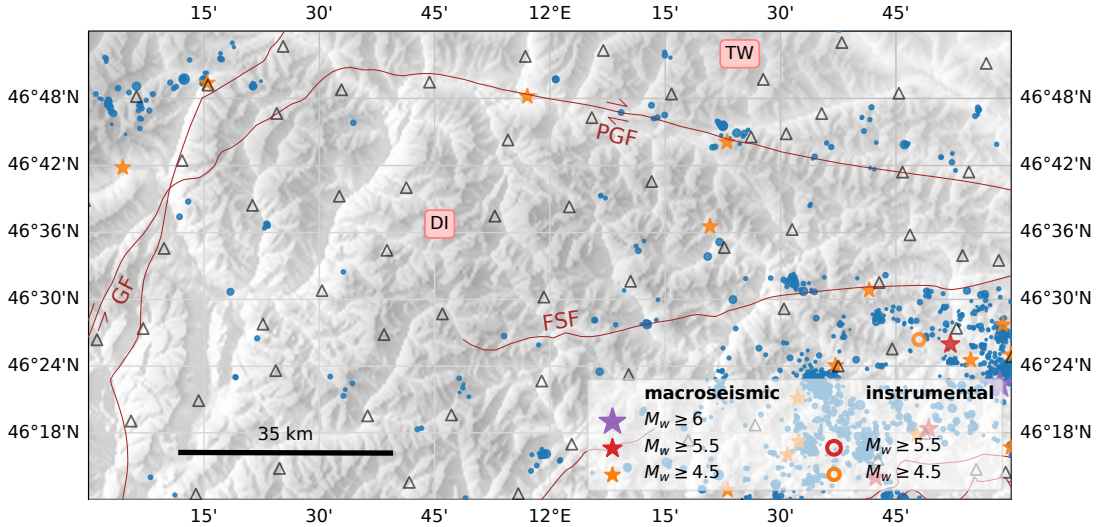

Figure 6.4. Detailed view of the seismicity in the Dolomite indenter region (blue circles). The historical earthquakes shown on this map are from Rovida et al. (2022). Major faults from Schmid, Fügenschuh, et al. (2004) (red lines) are FSF: Fella-Sava Fault, GF: Giudicarie Fault, PGF: Pustertal-Gailtal Fault. Tectonic units after Reiter et al. (2018) are DI: Dolomite Indenter, TW: Tauern Window.

Pustertal-Gailtal Fault and Tauern Window

Caporali et al. (2013) found through modelling of GPS velocities that the Pustertal-Gailtal Fault plays a major role in accommodating the indentation of the Adriatic plate into the European plate by dextral strike-slip motion. Due to its great length, the fault has the largest moment rate within the study area. However, the Pustertal-Gailtal Fault is not known to be very seismically active. I was able to relocate earthquakes along a 100 km section of the fault between 12.0° E and 13.0° E longitude. These events, as shown in profile E of Figure 6.2, occur at shallow depths from 5 to 10 km. A detailed map of the seismicity catalogue of along the fault is presented in Figure 6.5.

Similar to the Dolomite indenter, seismicity within the Tauern Window is sparse and has only few events with magnitudes greater than $M_L 1$. The catalogue contains about 200 events in this region. Especially in the eastern part of the Tauern Window, clustered seismicity can be observed at depths between $5-12$ km in the vicinity of the Mölltal and Katschberg faults. At its northern edge, the Tauern Window is bounded by the Salzach-Enns-Mariazell-Puchberg Fault, above which the seismicity rates as well as magnitudes increase again. However, this area lies outside the Swath-D network, severely decreasing the location accuracy for these events. A detailed map of the seismicity catalogue of this area is presented in Figure 6.5.

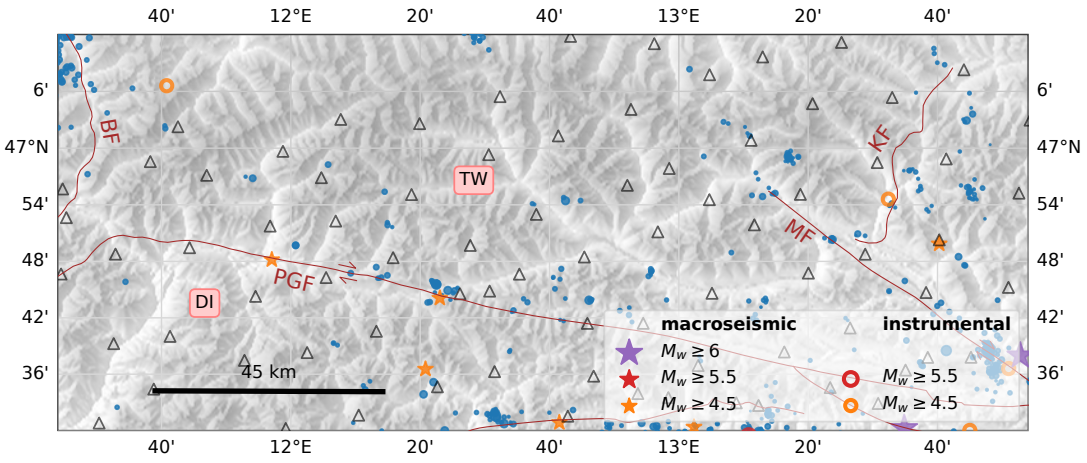

Figure 6.5. Detailed view of the seismicity in the Tauern Window region (blue circles), including the Pustertal-Gailtal Fault (in the southern part of the map view). The historical earthquakes shown on this map are from Rovida et al. (2022). Major faults from Schmid, Fügenschuh, et al. (2004) (red lines) are BF: Brenner Fault, KF: Katschberg Fault, MF: Mölltal Fault, PGF: Pustertal-Gailtal Fault. Tectonic units after Reiter et al. (2018) are DI: Dolomite Indenter, TW: Tauern Window.

Giudicarie-Lessini region

Seismicity in the Giudicarie-Lessini region is scattered and follows a more constant rate compared to the Friuli region. The area features frequent $M_L > 1$ earthquakes and multiple $M_L \geq 2$ events, especially around the lake Garda area. A single M_L 3 event was also recorded. As shown in Profile A of Figure 6.2, events occur mainly within a depth range of $5 - 15$ km, gradually deepening towards the Po-plain in the southeast. A detailed map of the seismicity catalogue of this area is presented in Figure 6.6.

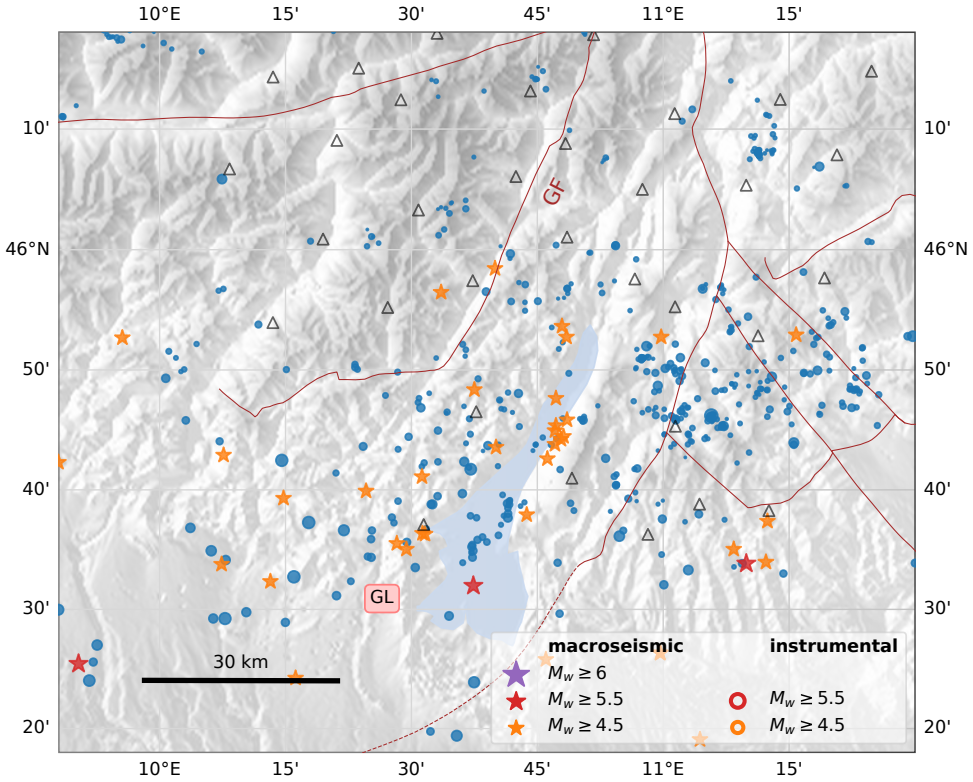

Figure 6.6. Detailed view of the seismicity in the Giudicarie-Lessini indenter region (blue circles). The historical earthquakes shown on this map are from Rovida et al. (2022). Major faults and tectonic units after Schmid, Fügenschuh, et al. (2004) and Reiter et al. (2018) are GF: Giudicarie Fault, and GL: Giudicarie-Lessini region.

Engadine and Ortler Alps

The Engadine and Ortler Alps demonstrate the second highest seismicity rate of the study area after the Friuli region. The seismicity is strongly clustered and occurs mainly above a depth of 10 km, with deeper earthquakes occurring towards the northwestern part of the region. This can be observed in Profile B of

Figure 6.2. The earthquakes in this region do not exceed magnitude $M_L 2$. The largest clusters in this region are indicated with symbols C and F in Figure 6.1, a more detailed analysis of these is provided in Chapter 7. A detailed map of the seismicity catalogue of this area is presented in Figure 6.7.

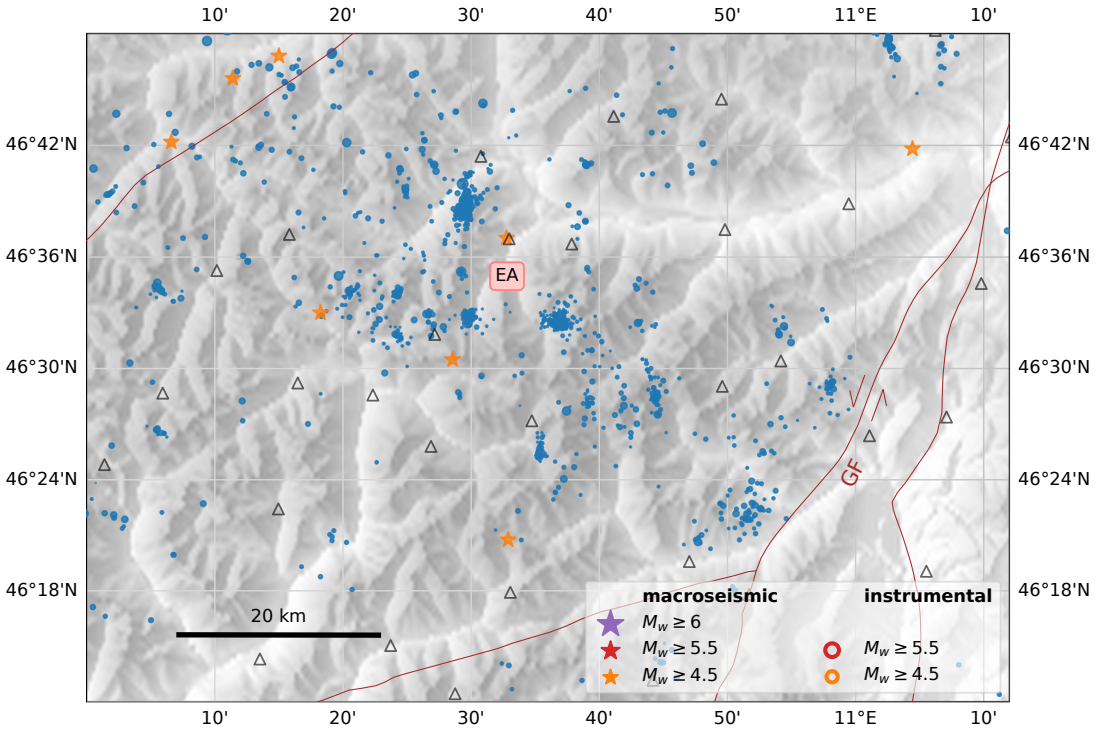

Figure 6.7. Detailed view of the seismicity in the Engadine Alps and Ortler Alps region (blue circles). The historical earthquakes shown on this map are from Rovida et al. (2022). Major faults and tectonic units after Schmid, Fügenschuh, et al. (2004) and Reiter et al. (2018) are GF: Giudicarie Fault, and EA: Engadine and Ortler Alps.

6.2 Spatial variation of the b-value

To investigate the spatial variation of the b-value of the Gutenberg-Richter relation (Gutenberg and Richter, 1944), I separated the study area into 5 seismo-tectonic domains: the Friuli region, the Giudicarie-Lessini region, the Engadine and Ortler Alps, the Dolomite indenter, and the Tauern Window. The domains are loosely based on the tectonic units described by Reiter et al. (2018), avoiding areas that are too small to provide a statistically stable result, as well as areas outside the Swath-D network. Figure 6.8 shows the events attributed to each of the different domains, and the magnitude frequency distribution for each domain.

Figure 6.8 reveals a significant variation in the b-value of the Gutenberg-Richter relation for the different seismo-tectonic domains with values ranging from 1.02 in the Friuli region to 1.73 in the Tauern Window. Due to the limited sample size and range of magnitudes in certain regions, I employed a bootstrapping approach to estimate the uncertainties and test the statistical significance of the results, as detailed in Section 5.3.

The values for a, b, and M_c and their standard deviations derived by bootstrapping are shown in Table 6.1.

Domain	a	b	M_c	N **events**
Dolomite indenter (DI)	2.92 ± 0.28	1.07 ± 0.19	1.13 ± 0.12	93
Engadine & Ortler Alps (EA)	4.38 ± 0.14	1.42 ± 0.10	0.81 ± 0.03	1453
Friuli (FR)	4.01 ± 0.18	1.02 ± 0.11	0.86 ± 0.05	2667
Giudicarie-Lessini (GL)	3.93 ± 0.22	1.07 ± 0.12	1.33 ± 0.16	417
Tauern Window (TW)	4.01 ± 0.30	1.73 ± 0.22	1.16 ± 0.11	163

Table 6.1. Parameters a and b and M_c and their standard deviations derived by bootstrapping for each seismo-tectonic domain.

By comparing b-values from many different areas around the world, Scholz (2015) found that the b-value appears to be inversely related to the differential stress ($\sigma_1 - \sigma_3$), confirming earlier results from laboratory experiments (Scholz, 1968; Amitrano, 2003). The b-values I found for the seismo-tectonic domains nicely fit into this picture, with the smallest b-values along the southern deformation front. The smallest b-value in the Friuli region coincides with the largest deformation rates from Global Navigation Satellite Systems (GNSS) studies (Caporali et al., 2013; Métois et al., 2015; Sánchez et al., 2018), followed by the second smallest b-value in the Giudicarie-Lessini region. The seismicity in the Engadine and Ortler Alps is characterised by an elevated b-value, coinciding with a low horizontal deformation rate. The high seismicity rate in this area could be related to uplift, as the Engadine and Ortler Alps show one of the highest uplift rates in the Alps (Sánchez et al., 2018), most likely due to postglacial isostatic rebound (Mey et al.,

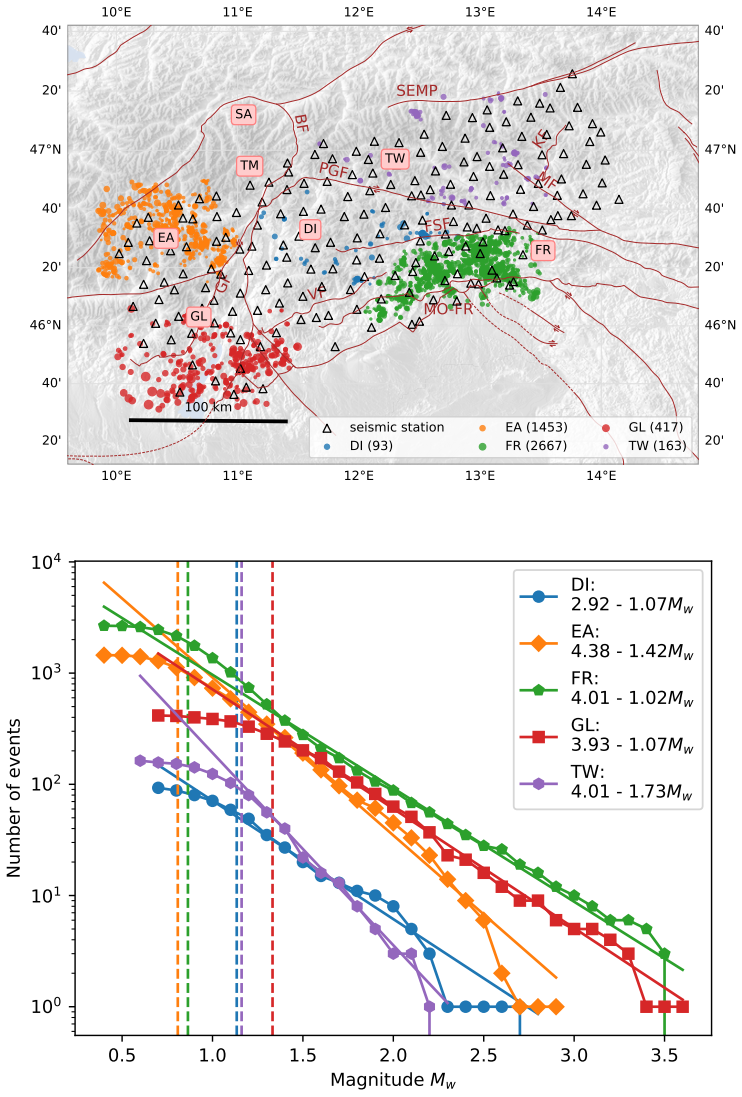

Figure 6.8. The upper panel shows the earthquakes selected for each of the seismo-tectonic domains: the Friuli region (FR, green), the Giudicarie-Lessini region (GL, red), the Engadine and Ortler Alps (EA, orange), the Dolomite indenter (DI, blue), and the Tauern Window (TW, purple). Magnitude frequency distributions for each of the seismo-tectonic domains are shown in the same colours in the lower panel. Magnitudes are in the moment magnitude scale (M_w), estimated using the scaling relation (Equation 5.3) by Munafò et al. (2016).

2016). The b-value in the Dolomite indenter is close to 1, but this is mainly due to contributing events on the Fella-Sava and Valsugana Faults along its southern margin. The north eastern part of the Dolomite indenter is almost completely aseismic. Recent crustal tomography studies show anomalously high surface wave phase velocities at seismogenic depths in this area (Sadeghi-Bagherabadi et al., 2021; Kästle, Molinari, et al., 2021), suggesting that this part of the crust is exceptionally dense and rigid. The Tauern Window displays a high b-value and lacks moderate magnitude seismicity. This could be related to the high-grade metamorphic lithology. Reiter et al. (2018) attributes the lack of seismicity in this region to the unfavourable orientation of existing faults with respect to the current stress field.

In Figure 6.9, I show the event rates and local magnitudes for each domain, with an additional time-dependent b-value for the Engadine and Ortler Alps and the Friuli regions. The b-values are based on the moment magnitude estimates (M_w), as described in Section 5.3, and calculated within a 150-event sliding window. Note that in both the Engadine and Ortler Alps and the Friuli regions, the seismicity is strongly clustered temporally, with a vast majority of the events occurring within a few sequences. Interestingly, in the Engadine and Ortler Alps, the b-value remains elevated throughout the observation period, independent of these sequences, whereas in the Friuli region, the low b-value increases within each of the sequences. This might be an indication that the Engadine and Ortler Alps host more swarm-type sequences, and the Friuli region shows typical mainshock-aftershock sequences. One exception is the 1 February 2019 sequence, which I discuss in more detail in Chapter 7. Due to the small number of events used for the b-value calculation, the absolute values should not be given too much credit. The temporal patterns, however, are significant and hint at different seismic mechanisms in both areas.

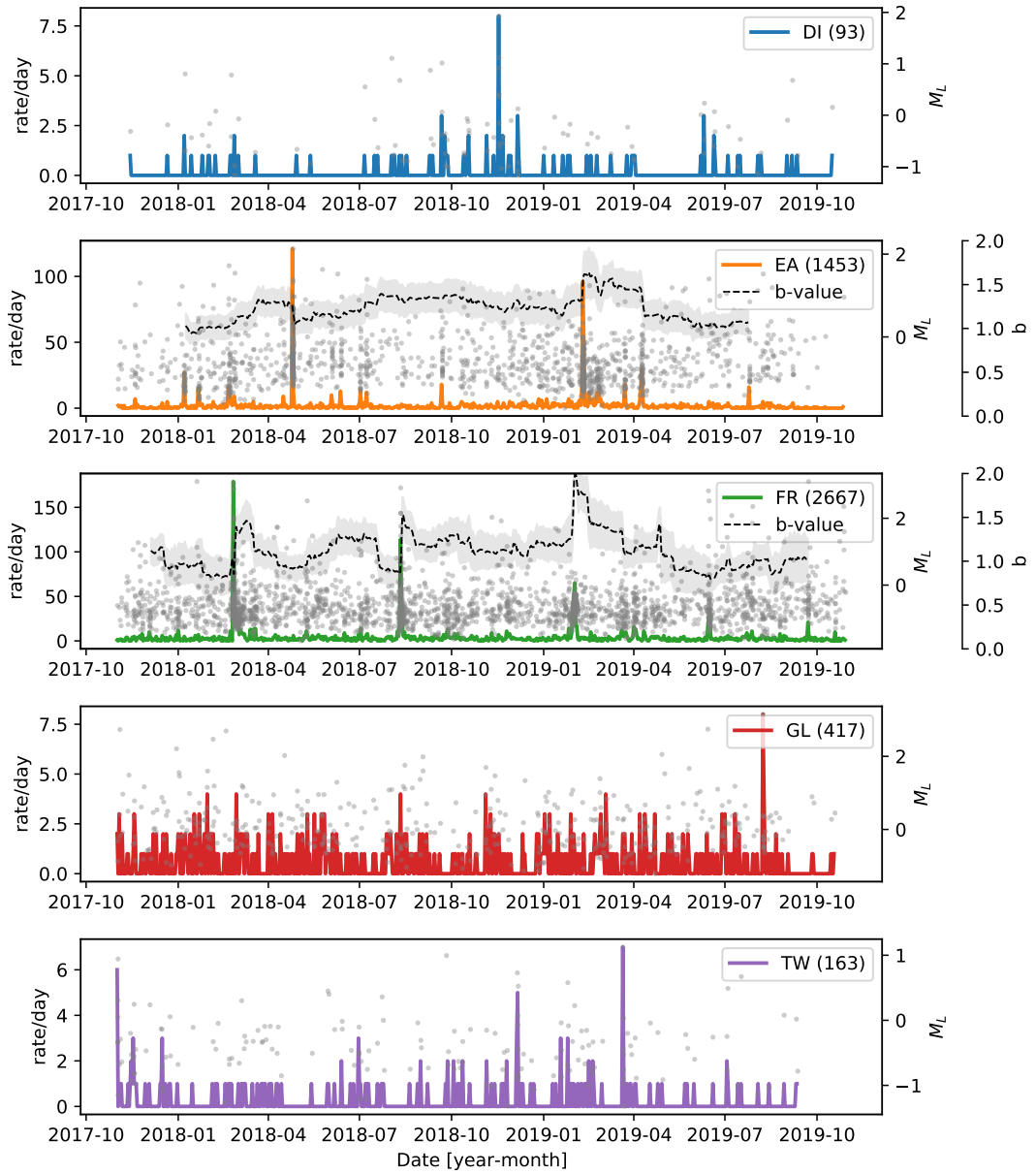

Figure 6.9. Event rate and local magnitudes for the different seismo-tectonic domains. A time dependent b-value is shown additionally for the Engadine and Ortler Alps and the Friuli regions. The b-values are calculated from the estimated M_w (see Section 5.3) in a 150-event sliding window and smoothed out by taking the mean b-value for each day. Bootstrapping was applied to each time step to estimate the errors as in Section 5.3.

6.3 Sensitivity of template matching to low-magnitude seismicity

The effectiveness of the template matching method for detecting small-magnitude earthquakes is illustrated in Figure 6.10. The figure displays the variation in units of local magnitude between all of the detected earthquakes and corresponding master events for three different cross-correlation thresholds. I define the cross-correlation value (CC) as the median of the three highest maximum cross-correlation coefficients on the 15 stations closest to the event pair. Each cross-correlation is based on two 10 s event waveforms on the vertical channel. For the subset where $CC \geq 0.9$, the maximum difference is limited to two units of magnitude, whereas for $CC \geq 0.5$, earthquakes with a difference of up to four units of magnitude are detected. I show an example of such a detection in appendix Figure A7. The asymmetric shape of the histogram is caused by the skewness of the master event magnitudes. This can be inferred from Figure 5.2: almost all of the events with magnitude $M_L \geq 1.0$ are used as master events. The majority of the seismic activity I detected ranges from zero to two units of magnitude below the known seismic activity in the region, demonstrating that my workflow is exceptionally sensitive to low-magnitude seismicity.

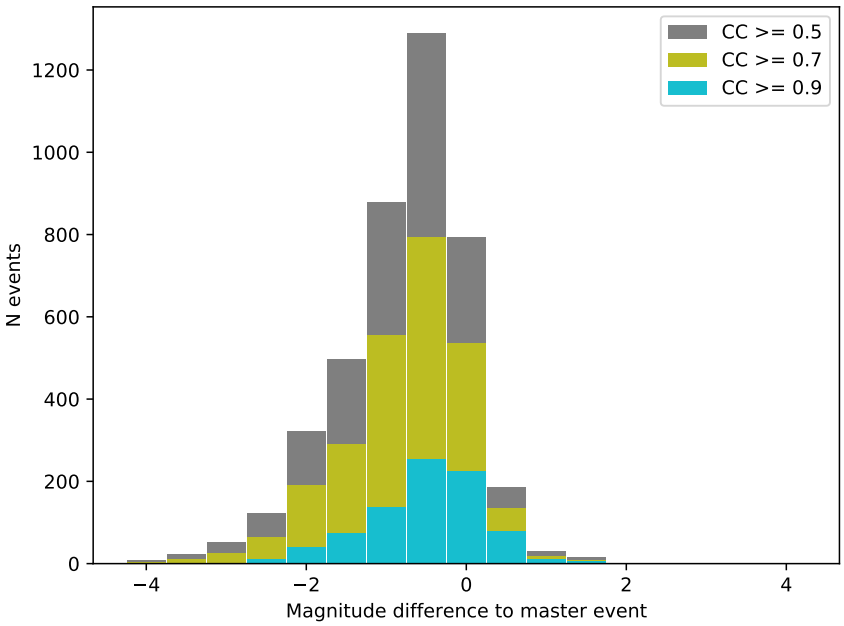

Figure 6.10. Difference in local event magnitude between each event and its corresponding master event. The CC values refer to the median of the three highest maximum cross-correlation coefficients, where 15 stations are considered. Each cross-correlation is performed on a 10 s event waveform on the vertical channel. This figure appeared in Hofman, Kummerow, and Cesca (2023).

CHAPTER 7

Analysis of seismicity clusters

Within the two-year recording period of the Swath-D network, the average seismicity rate is approximately 20 events per day. However, as can be seen in Figure 3.8, several short bursts of seismic activity have occurred throughout the recording period, with daily rates exceeding 100 events on six occasions. These sequences are indicated in Figure 3.8 by the symbols A-F, which also appear on the map in Figure 6.1 to indicate their locations. The first event sequence (A) occurred on 3 November 2017 in the Stubai Alps south of Innsbruck, Austria. This area is known to be seismically active (e.g. Reiter et al., 2018). The largest magnitude recorded within this sequence is 3.02 M_L. However, this earthquake cluster is located outside the Swath-D network, and the station distribution is therefore unfavourable for the precise relocation of these events. The peak in April 2019 originates from two separate smaller event sequences coincidentally occurring on the same day. I will therefore not discuss these earthquake clusters any further in this thesis.

In Section 7.1, I demonstrate the successful application of graph theory to separate the seismicity clusters into distinct sequences that can be attributed to individual segments of complex fault systems. Based on these sub-clusters, in Section 7.2, I present a method of precise relative relocalisation using S-P differential travel-time inversion that allows me to find the orientations of individual fault planes.

After applying these methods to the clusters B-F, I provide a detailed analysis of

the earthquake sequences in terms of the spatial and temporal distribution of the events within each sequence, as well as their frequency magnitude distributions in Section 7.3. Three of these sequences are located in the Friuli region (B, D, and E, as indicated in Figure 6.3) and will be discussed in Section 7.3.1. The other two sequences are located in the Engadine and Ortler Alps region (C and F, as indicate in Figure 6.7) and will be discussed in Section 7.3.2.

7.1 Application of Graph Theory

Graph theory, also referred to as network theory, is a mathematical concept used to describe and analyse relations between objects. In graph theory, the objects are referred to as the graph's nodes or vertices, whereas their relation to one another is represented by edges connecting them. Edges may or may not have a weight describing the strength of the connection, and a direction, the latter of which makes the graph a directed graph. Redefining a problem as a graph can be very useful, because it allows us to apply algorithms to analyse properties of the graph. Albert and Barabási (2002) give an overview of the recent advances in graph theory. Downey (2018) provides an introduction to graph theory and programming in Python, making use of the NetworkX package (Hagberg et al., 2008).

The abstract nature of graph theory allows for its application across numerous scientific disciplines. Phillips et al. (2015) provide an overview of the applications of graph theory in geosciences. In seismology, examples of applications include seismic ray path calculation (Nakanishi and Yamaguchi, 1986), identification of multiplets in microseismic data (Arrowsmith and Eisner, 2006), phase association (McBrearty et al., 2019), and complex earthquake networks (Abe and Suzuki, 2012). Abe and Suzuki (2012) used vertices to represent volumes on a spatial grid, and added edges between all subsequent events above a certain magnitude threshold. They then studied how the properties of the graph changed due to the occurrence of large earthquakes.

This section presents a very different approach to the application of graph theory, which is based on the waveform-based similarity clustering of earthquakes. In order to characterise the seismicity cluster as a graph, I define vertices for all individual earthquakes, and edges represent the waveform similarity between the connected earthquakes. An edge is established between two earthquakes when the median of the three highest maximum cross-correlation coefficients exceeds a threshold of 0.85. The cross-correlation coefficients are calculated using a 10-second event waveform on the vertical channel of the seismograph. The edge is weighted with the cross-correlation value and has no direction. Arrowsmith and Eisner (2006) also used waveform similarity to create graphs, but the event clus-

ters that they end up with could have more easily been calculated using classical single-linkage hierarchical algorithms. An example of the graph representation of an earthquake cluster is illustrated in Figure 7.1, where the left panel shows the spatial distribution of the earthquakes in the cluster, and the right panel shows the graph representation of the cluster, with the vertices coloured by their degree (the number of edges connecting to it).

It should be noted that there are infinite ways to draw a graph in terms of the positioning of the vertices. For the purpose of showing the event similarity as in Figure 7.1, it is useful to use a force directed graph layout. In such a layout, the vertices are placed in a position, as if held together by springs with forces proportional to the weights of the edges. These positions can be approximated using an algorithm such as the Kamada-Kawai algorithm (Kamada and Kawai, 1989). In this representation, events with high waveform similarity will be drawn closer, while events less similar will be placed further apart. In this representation, it can easily be seen that two sub-clusters emerge from the earthquake cluster in Figure 7.1. Although there are numerous edges interconnecting the two main sub-clusters, the events within the sub-clusters are more strongly connected.

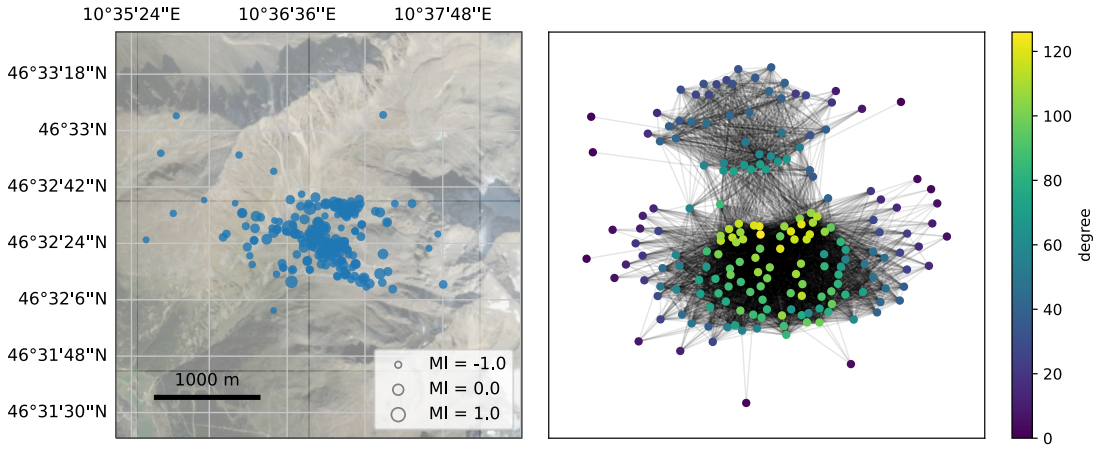

Figure 7.1. Example of the event locations of an earthquake cluster in the Ortler Alps (sequence F in Figure 6.1) (left), and the graph representation of the earthquake cluster (right) with the vertices coloured by their degree (number of connected edges).

A useful property of the graph in the context of sub-clusters is its modularity (Newman, 2006). This is a measure of the graph's tendency to form strongly connected groups of vertices with more sparse connections between those groups. These groups are referred to as communities or partitions in graph theory. In the context of earthquake clusters, I refer to those groups as sub-clusters. The modularity is expressed by Newman (2006) as

$$Q = \frac{1}{2m} \sum_{ij} (A_{ij} - \frac{k_i k_j}{2m}) \delta(c_i, c_j) \tag{7.1}$$

where m is the total number of edges in the graph, A_{ij} is the weight of the edge between vertices i and j. k_i and k_j are the total number of edges connected to vertices i and j, respectively, also referred to as the degree of vertices i and j. Finally, c_i and c_j are the sub-clusters that vertices i and j belong to, and $\delta(c_i, c_j)$ is 1 if both vertices are in the same sub-cluster, or 0 otherwise. It should be noted that to calculate the modularity, a separation into sub-clusters is already implied. The goal is therefore to find the configuration of sub-clusters that maximises the modularity. Blondel et al. (2008) proposed an algorithm for approximating the optimal modularity and sub-cluster configuration. Their method, often referred to as the Louvain method for community detection, avoids calculating all possible configurations of any number of sub-clusters, which would be computationally expensive.

Applying the Louvain method for community detection to the earthquake cluster from Figure 7.1 yields 3 sub-clusters as illustrated in Figure 7.2. By colouring the events by their associated sub-cluster in the map view, a clear spatial separation can be observed.

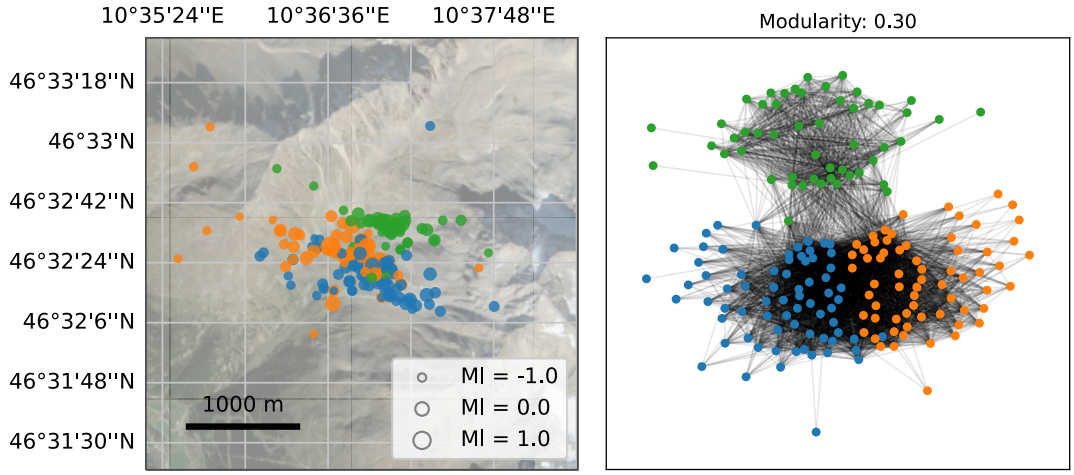

Figure 7.2. Earthquake cluster from Figure 7.1 split into 3 sub-clusters that optimise the modularity of the graph. The events are coloured by their associated sub-clusters in a map view (left), and in the graph representation of the cluster (right).

7.2 High precision relative relocalisation

To further improve the precision of earthquake hypocenters locally, relative relocalisation methods can be applied. Rather than locating each event individually using independent phase-arrival picks as described in Section 3.3, relative relocalisation depends on differential travel-times between closely located events. A requirement for such methods is that the inter-event distances are small compared to the source-receiver distances. If this condition is satisfied, and we assume a constant seismic velocity between the event locations, we can relate the differential P-wave travel time for an event pair to their inter-event distance, following Got and Okubo (2003):

$$\Delta T_{P}{}_{ij}^{k} = \Delta t_{ij} + \Delta \mathbf{r}_{ij} \cdot \mathbf{s}_{P}{}^{k} \tag{7.2}$$

where $\Delta T_{P}{}_{ij}^{k}$ is the differential P-wave travel-time for station k between events i and j, Δt_{ij} is their difference in origin time, $\Delta \mathbf{r}_{ij}$ is the vector between their locations, and $\mathbf{s}_{P}{}^{k}$ is the P-wave slowness vector pointing from the source location to station k, which is assumed to be equal for both events. Similarly, for S-waves, we can write:

$$\Delta T_{S}{}_{ij}^{k} = \Delta t_{ij} + \Delta \mathbf{r}_{ij} \cdot \mathbf{s}_{S}{}^{k} \tag{7.3}$$

If we assume that $\mathbf{s}_{P}{}^{k}$ and $\mathbf{s}_{S}{}^{k}$ are parallel, which can be assumed if v_P/v_S is constant along the ray-path, subtracting Equation 7.2 from 7.3 yields:

$$\Delta T_{S\text{-}P}{}_{ij}^{k} = \Delta \mathbf{r}_{ij} \cdot [\mathbf{s}_{S}{}^{k} - \mathbf{s}_{P}{}^{k}] = \frac{v_P - v_S}{v_P \cdot v_S} \cdot \mathbf{e}^{k} \cdot \Delta \mathbf{r}_{ij} \tag{7.4}$$

establishing an elegant relation between the differential S - P travel time of the event pair ij and their inter-event distance (Jörn Kummerow, pers. comm.). Assuming that $\mathbf{s}_{S}{}^{k}$ and $\mathbf{s}_{P}{}^{k}$ are parallel, $\mathbf{e}^{k}$ is the unit vector pointing in the shared direction of the P- and S-wave takeoff direction. The origin times of both events are conveniently eliminated by the substraction. A schematic illustration of the method is provided in Figure 7.3.

We can write a system of equations of the form $\mathbf{d} = G \cdot \mathbf{m}$ based on Equation 7.4. This allows us to solve for the relative locations of N co-located events using the differential S - P travel time delays for M stations as a linear inverse problem. Vector $\mathbf{d}$ is contains all $M \cdot N(N-1)/2$ differential travel time delays $\Delta T_{S\text{-}P}{}_{ij}^{k}$. Matrix G contains the three Cartesian coordinates of the $\mathbf{e}^{k}$ vectors, which can be computed by ray-tracing. The model vector $\mathbf{m}$ has $3 \cdot N$ elements that represent Cartesian coordinates of the event locations relative to a fixed reference point. This reference point can be any of the events, that will subsequently be used as an origin of the coordinate system.

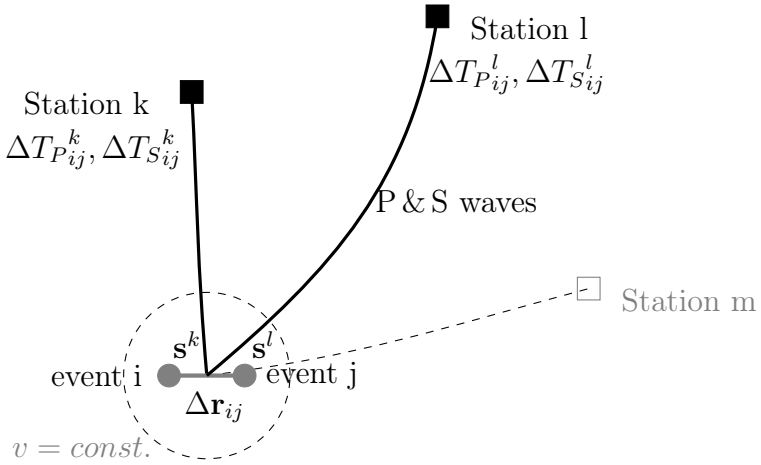

Figure 7.3. Schematic illustration of the relative relocalisation method using S-P differential travel times. The relative position vector $\Delta \mathbf{r}_{ij}$ determines the locations of the two events, i and j, that are recorded by stations k, l, and m. The inter-event distance should be small compared to the source-receiver distances, and the slowness vectors $\mathbf{s}_P$ and $\mathbf{s}_S$ are assumed to be identical for the two events.

In Equation 7.5, $s_{x,y,z}^{k}$ represent the elements of the slowness vector from the source region to station k, $\mathbf{s}^k = \frac{v_p - v_s}{v_p \cdot v_s} . \cdot \mathbf{e}^k$. The location vector $\Delta \mathbf{r}_{ij}$ between events i and j is represented by the Cartesian coordinates (x_{ij}, y_{ij}, z_{ij}). In this example, the first event defines the origin of the relative coordinate system $(0, 0, 0)$. It therefore follows that $\Delta \mathbf{r}_{ij} = \Delta \mathbf{r}_{1j} - \Delta \mathbf{r}_{1i}$.

$$
\begin{pmatrix}
\Delta T_{S\text{-}P}{}^{1}_{11} \\
\vdots \\
\Delta T_{S\text{-}P}{}^{M}_{11} \\
\Delta T_{S\text{-}P}{}^{1}_{12} \\
\vdots \\
\Delta T_{S\text{-}P}{}^{M}_{12} \\
\Delta T_{S\text{-}P}{}^{1}_{13} \\
\vdots \\
\Delta T_{S\text{-}P}{}^{M}_{13} \\
\vdots \\
\cdot \\
\vdots \\
\Delta T_{S\text{-}P}{}^{M}_{1N} \\
\Delta T_{S\text{-}P}{}^{1}_{23} \\
\vdots \\
\Delta T_{S\text{-}P}{}^{M}_{23} \\
\Delta T_{S\text{-}P}{}^{1}_{24} \\
\vdots \\
\Delta T_{S\text{-}P}{}^{M}_{24} \\
\vdots \\
\cdot \\
\vdots \\
\Delta T_{S\text{-}P}{}^{M}_{(N-1)N}
\end{pmatrix}
=
\left(\begin{array}{cccccccccccccccccccccccc}
-s_x^1 & -s_y^1 & -s_z^1 & 0 & \cdots &&&&&&&&&&&&&&&&&& \cdots & 0 \\
\vdots & \vdots & \vdots & \vdots &&&&&&&&&&&&&&&&&&&& \vdots \\
-s_x^1 & -s_y^1 & -s_z^1 & 0 & \cdots \\
0 & \cdot & 0 & -s_x^1 & -s_y^1 & -s_z^1 & 0 & \cdots \\
\vdots &&& \vdots & \vdots & \vdots & \vdots \\
&& 0 & -s_x^M & -s_y^M & -s_z^M & 0 & \cdots \\
&&& 0 & \cdot & 0 & -s_x^1 & -s_y^1 & -s_z^1 & 0 & \cdots \\
&&& \vdots && \vdots & \vdots & \vdots & \vdots & \vdots \\
&&&& \cdots & 0 & -s_x^M & -s_y^M & -s_z^M & 0 & \cdots \\
&&&&&& \ddots & \ddots & \ddots & \ddots & \ddots \\
&&&&&&& \cdots & \cdots & \cdots & \cdots & \cdots & \cdots & \cdots & \cdots & \cdots & \cdots & \cdots & \cdots & \cdots \\
&&&&&&&&&&&&&&&& \ddots & \ddots & \ddots & \ddots & \ddots \\
&&&&&&&&&&&&&&&& \cdots & 0 & -s_x^M & -s_y^M & -s_z^M & 0 & \cdots \\
&&&& \cdots & 0 & s_x^1 & s_y^1 & s_z^1 & -s_x^1 & -s_y^1 & -s_z^1 & 0 & \cdots \\
&&&&& \vdots & \vdots & \vdots & \vdots & \vdots & \vdots & \vdots & \vdots \\
&&&& \cdots & 0 & s_x^M & s_y^M & s_z^M & -s_x^M & -s_y^M & -s_z^M & 0 & \cdots \\
&&&& \cdots & 0 & s_x^1 & s_y^1 & s_z^1 & 0 & \cdot & 0 & -s_x^1 & -s_y^1 & -s_z^1 & 0 & \cdots \\
&&&&& \vdots & \vdots & \vdots & \vdots & \vdots && \vdots & \vdots & \vdots & \vdots & \vdots \\
&&&&& 0 & s_x^M & s_y^M & s_z^M & 0 & \cdot & 0 & -s_x^M & -s_y^M & -s_z^M & 0 & \cdots \\
&&&&&& \ddots & \ddots & \ddots & \ddots & \ddots && \ddots & \ddots & \ddots & \ddots & \ddots \\
&&&&&&& \cdots & \cdots & \cdots & \cdots & \cdots & \cdots & \cdots & \cdots & \cdots & \cdots & \cdots & \cdots & \cdots & \cdots & \cdots && \vdots \\
\vdots &&&&&&&&&&&&&&&& \ddots & \ddots & \ddots & \ddots & \ddots & \ddots & \ddots & 0 \\
0 & \cdots &&&&&&&&&&&&&&& \cdots & 0 & s_x^M & s_y^M & s_z^M & -s_x^M & -s_y^M & -s_z^M
\end{array}\right)
\begin{pmatrix}
x_{11} \\
y_{11} \\
z_{11} \\
\vdots \\
x_{1N} \\
y_{1N} \\
z_{1N}
\end{pmatrix}
\tag{7.5}
$$

In order to evaluate the method, I constructed a synthetic set of events through the forward modelling of travel-times on a real location within the network, utilising the actual station configuration illustrated in Figure 7.4. The synthetic events are arranged on a 5 by 5 rectangular plane with a strike of 90° and a 45° dip towards the south. The location of the central event was fixed in the inversion. The differential travel-times $\Delta T_{S\text{-}P}$ were calculated from the synthetic P- and S-wave travel-times. The result of the inversion is shown in Figure 7.5.

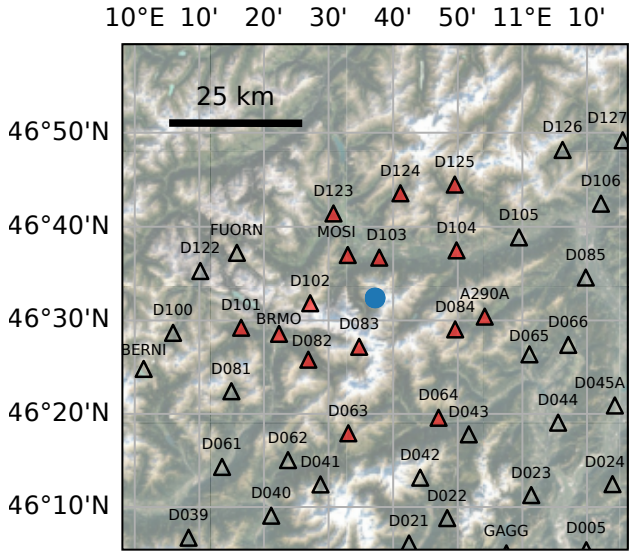

Figure 7.4. Station configuration of the synthetic test shown in Figure 7.5. The location of the synthetic events is indicated by the blue dot in the centre of the map. The filled triangles indicate the selection of seismic stations used in the synthetic test.

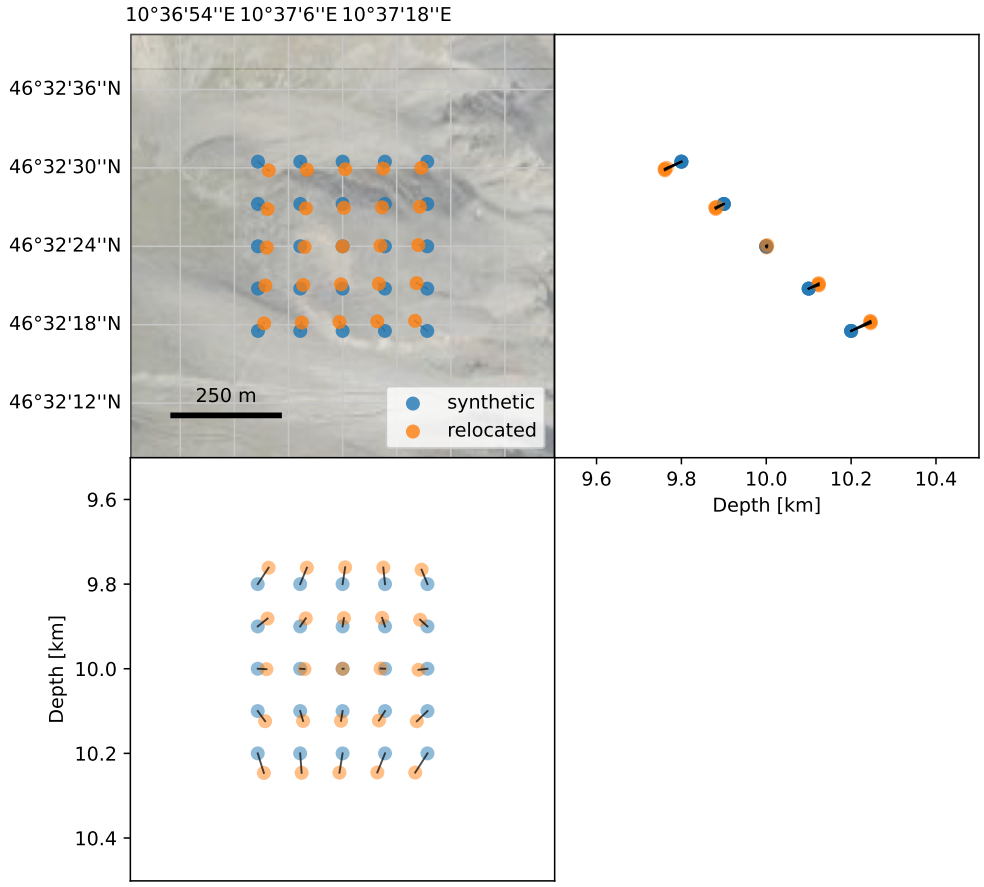

Figure 7.5. Result of the synthetic differential travel-time inversion. The synthetic event locations are arranged on a 5 by 5 rectangular plane with a strike of 90° and a 45° dip towards the south (blue dots). In general, the event locations are accurately reconstructed. The geometry of the plane is precisely resolved, with the horizontal dimensions slightly underestimated and the vertical dimensions slightly overestimated. This results in an overestimation of the plane dip by 8°. The strike of the relocated fault plane is reconstructed with a precision of 1° in comparison to the synthetic model.

When real data are are used, the differential travel-times ΔT_P, ΔT_S, and consequently $\Delta T_{S\text{-}P}$, can be calculated from the cross-correlation of the corresponding phase windows. To ensure that the locations are well constrained, I select only events with at least 4 stations containing both a P- and an S-pick. An example of the differential travel-time inversion using data from the northernmost sub-cluster of the event cluster illustrated in Figure 7.2 is shown in Figure 7.6. Whereas the original locations scatter quite significantly, the relocated events are located on a planar geometry striking roughly north-south, and steeply dipping towards the west at an almost vertical angle.

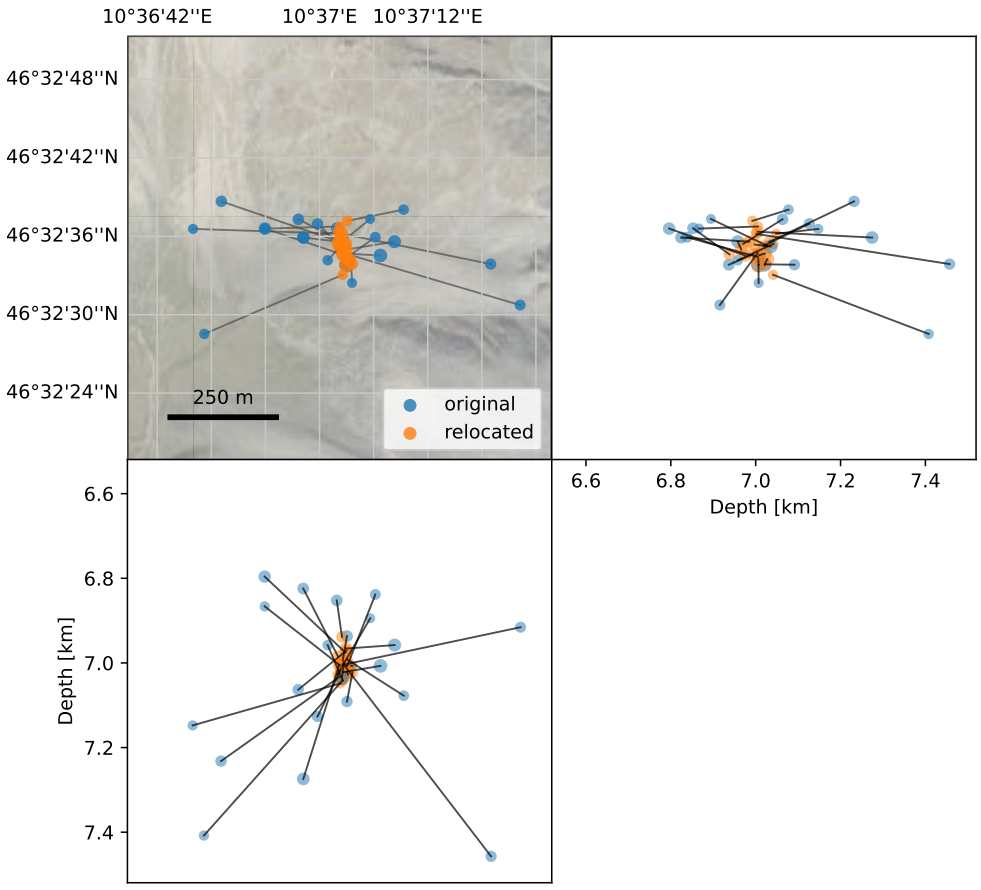

Figure 7.6. Result of the travel-time inversion of a real data example. The events in this example are from the northernmost sub-cluster of the event cluster illustrated in Figure 7.2. Note that only a selection of the sub-cluster is shown here, as the events are required to have at least 4 stations containing both a P- and an S-pick for the inversion.

I estimate the orientation of the geometry described by the relocated events by

calculating the eigenvectors of the covariance matrix using singular value decomposition. The application of this method yields a plane with a strike of 352°, dipping west at a steep angle of 86°. Moment tensors calculated for events within this set align within a few degrees strike and about 10 degrees dip (Gesa Petersen, pers. comm.) as shown in Figure 7.7.

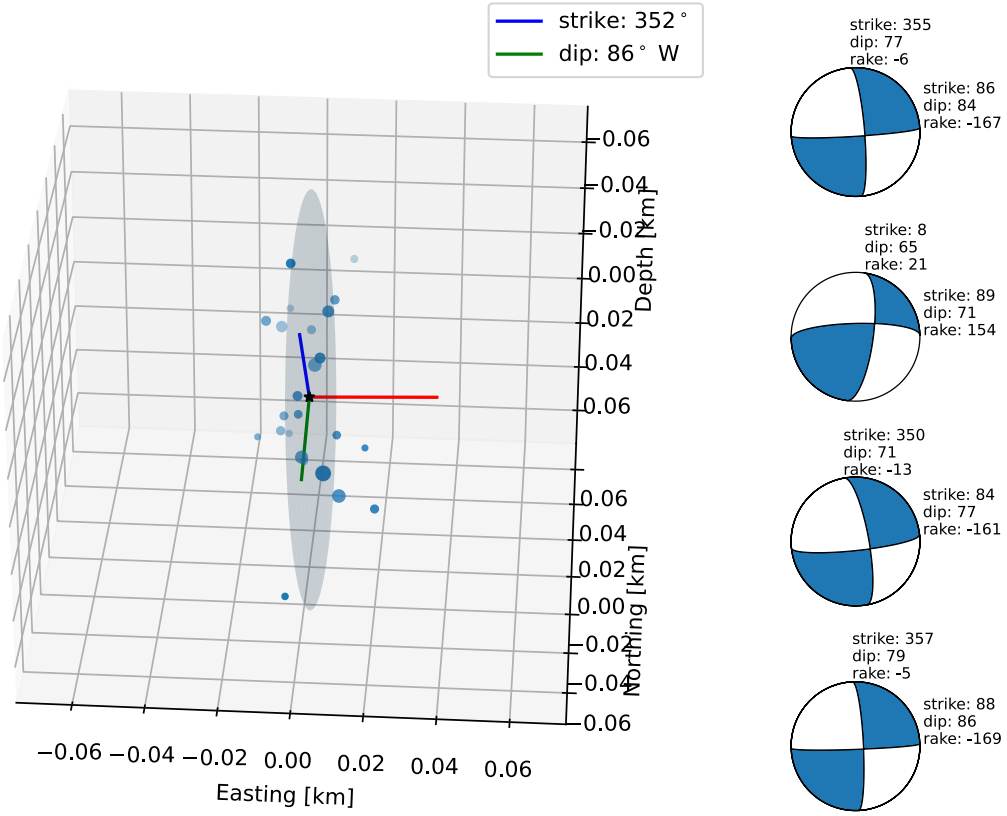

Figure 7.7. 3-D plot of the relocated events from Figure 7.6 and the plane described by the eigenvectors of the covariance matrix (left), and moment tensors from this set of events calculated by Gesa Petersen (pers. comm.).

7.3 Spatio-temporal analysis of clustered seismicity

The seismicity clusters described in this section have been identified based on the event detection rate in in Figure 3.8. For each of the six peaks where the event rate exceeds 100 events per day , I determined the location of the sequence by analysing the locations of all events on that particular day. I then applied a spatial filter to extract only the events that are spatially clustered. Finally, I included the template families of each of the events into the cluster (see Section 3.1). This allows me to analyse the evolution of each cluster before and after its main event sequence.

7.3.1 Friuli region

The seismicity in the Friuli region is strongly clustered, and three of the largest seismicity clusters recorded by the Swath-D network (B, D, and E in Figures 6.1 and 6.3) are located in this region.

Sequence B (25 February 2018)

The first sequence (B) occurred on 25 February 2018. A total of 411 events could be located for this sequence, which occurred north of the village of Cimolais, on the border to Veneto. The largest magnitudes in this sequence are 3.05 M_L and 2.88 M_L. The graph representation of this cluster yields a very high modularity value, indicating that it can be split into several sub-clusters. The Louvain method for community detection as described in Section 7.1 suggests a split into 8 different sub-clusters, the 4 largest of which could be sucessfully relocated using the method described in Section 7.2. The graph representation of this cluster, as well as the spatial distribution of the relocated events coloured by their sub-cluster association, is depicted in Figure 7.8. A comparison of the relocated events to the original event locations is made in appendix Figure A17.

Based on the eigenvectors of the covariance matrix, I estimated fault plane orientations for the largest 4 sub-clusters of sequence B, as illustrated in Figure 7.9. The orientations are indicated in the figure. For comparison, the moment tensor solutions of individual events within the largest 2 of the sub-clusters (Gesa Petersen, pers. comm.) are presented alongside in the same colours.

The strike of the estimated fault plane for the first sub-cluster (in blue colour) fits very well with the moment tensor solutions, as both indicate a possible fault

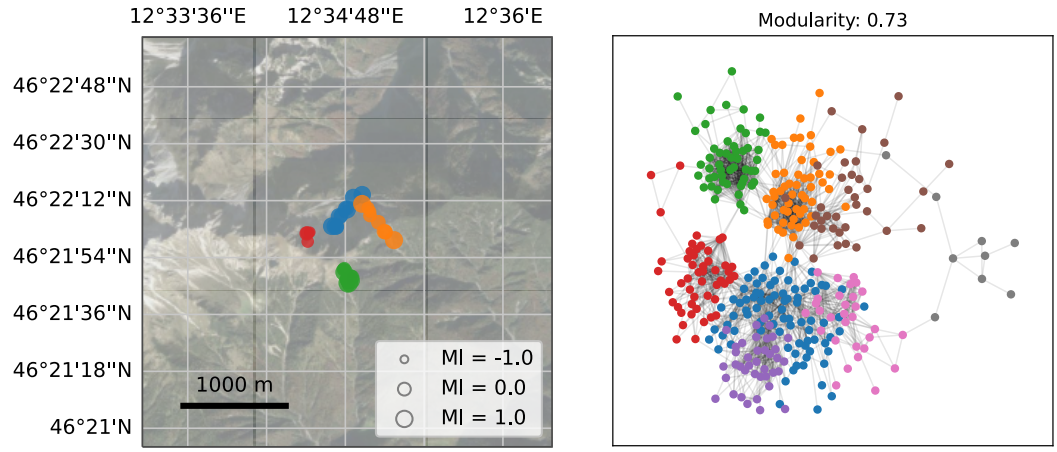

Figure 7.8. Earthquake cluster B split into 8 sub-clusters that optimise the modularity of the graph. The relocated event locations are coloured by their associated sub-clusters in a map view (left), and in the graph representation of the cluster (right).

plane within 10°. For the second fault plane, the strike shows a difference of 37°. Both faults are near vertical and the moment tensors indicate mainly strike-slip faulting, although one of the moment tensor solutions for the first fault indicates a slight reverse-faulting component. No moment tensor solutions are available for the third and fourth sub-clusters (in green and red colour), which appear to have very different orientation. Based on the orientation of these faults within the prevailing stress field, they should have normal- or thrust-fault mechanisms.

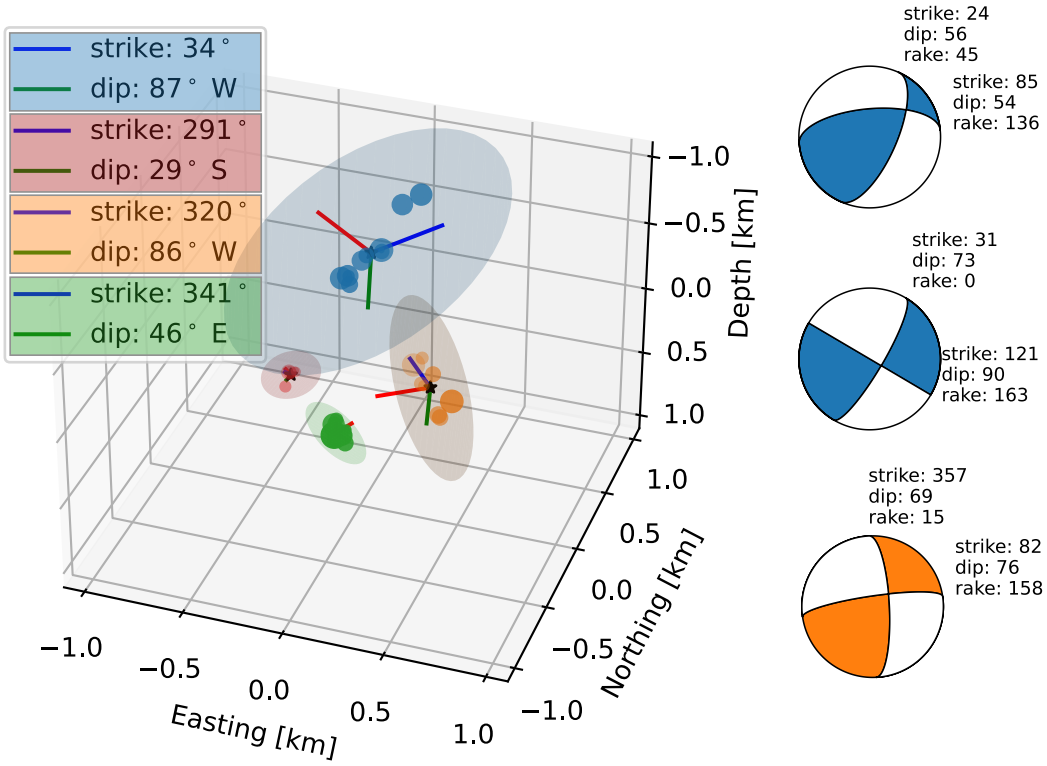

Figure 7.9. Estimated fault plane orientations for the 4 largest sub-clusters of sequence B, and moment tensor solutions of individual faults within the largest 2 sub-clusters by Gesa Petersen (pers. comm.)

Figure 7.10 illustrates the distribution of the event magnitudes over time, which exhibits typical mainshock-aftershock characteristics. The largest event occurs at the start of the main sequence on 25 Februrary 2018, with no significant foreshock activity recorded. There is a typical gap of one unit of magnitude between the largest two events and the rest of the aftershock series, and the activity decays over the period of about 4 months. The first two faults (in blue and orange colour) from Figure 7.9 are activated simultaneously and remain active for an extended period of times, whereas the other sub-clusters seem to be activated later in the sequence and comprise only aftershock events.

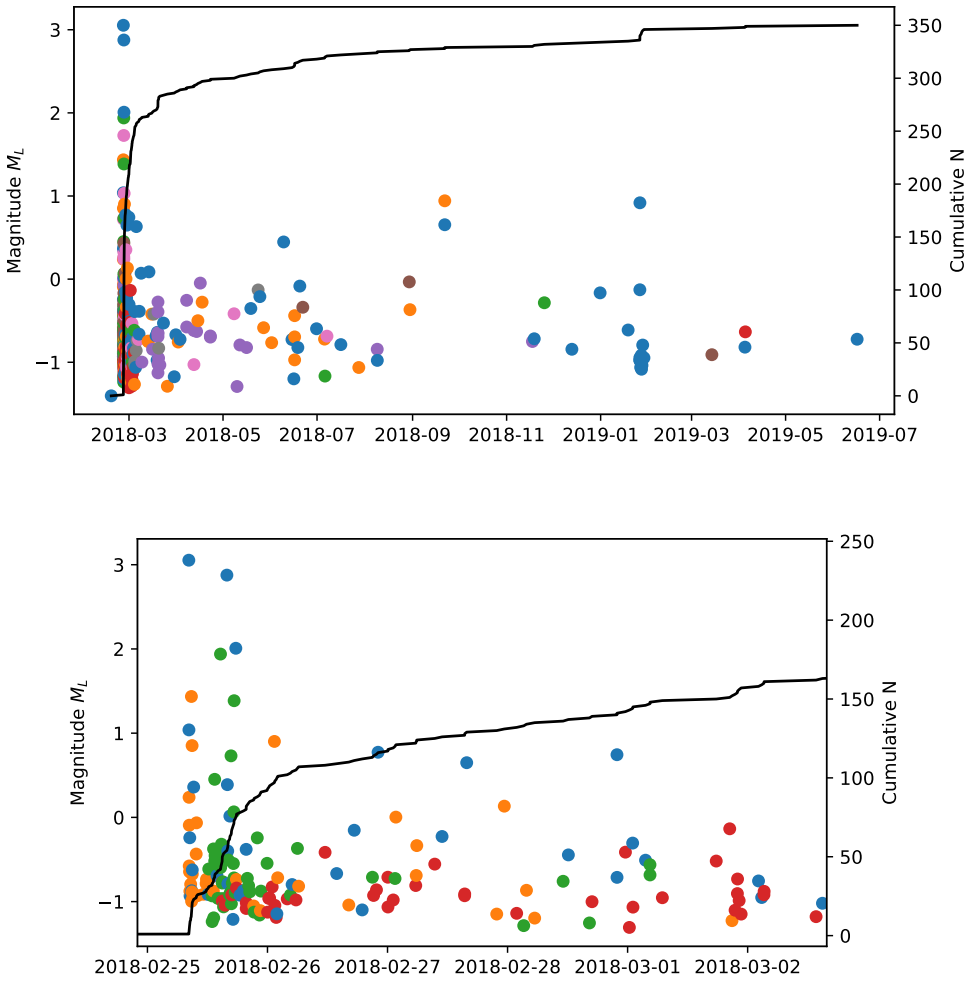

Figure 7.10. Temporal magnitude distribution of all events in sequence B over a period of 4 months (upper panel), and within the first 5 days from the main sequence (lower panel). The events are coloured by their associated sub-clusters.

Sequence D (11 August 2018)

The second sequence in the Friuli region (D) took place on 11 August 2018 and comprises a total of 202 relocated events. The events in this sequence are located just south of the municipality of Tolmezzo. The largest magnitude in this sequence is 2.91 M_L. The graph representation of this cluster yields an elevated modularity value, indicating that it can be split into several sub-clusters. The Louvain method for community detection as described in Section 7.1 suggests a split into 4 different sub-clusters. A relative relocalisation of the events based on the S-P differential travel times (see Section 7.2) was possible for all 4 sub-clusters. The graph representation of this cluster, as well as the spatial distribution of the relocated event locations coloured by their sub-cluster association, is depicted in Figure 7.11. A comparison of the relocated events to the original event locations is made in appendix Figure A18.

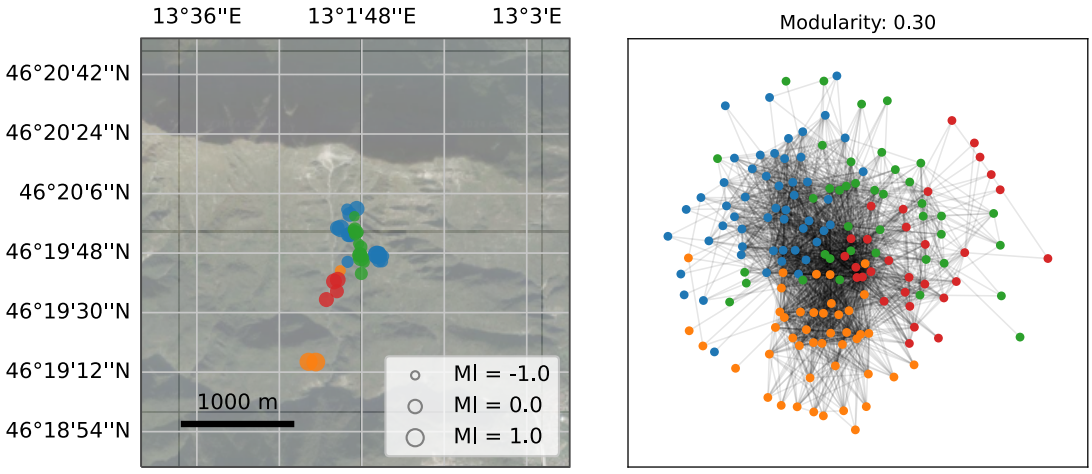

Figure 7.11. Relocated events for earthquake cluster D (left) and the graph representation of the cluster (right).

Apart from the second sub-cluster (in orange colour), all relocated sub-clusters concentrate on planar geometries, as illustrated in Figure 7.12. The orientations of the estimated fault planes are indicated on the figure. For comparison, the moment tensor solution of a single event from the largest of the sub-clusters (Gesa Petersen, pers. comm.) is presented alongside. The strike of the estimated fault for this sub-cluster (in blue colour) fits within 3° from the moment tensor solution, although the dip is found to be shallower. The focal mechanism implies a thrust-faulting event with a strike slip component. No moment tensor solutions are available for the third and fourth sub-clusters (in green and red colour).

Figure 7.13 illustrates the distribution of the event magnitudes over time, which exhibits foreshock-mainshock-aftershock characteristics. The foreshock series on

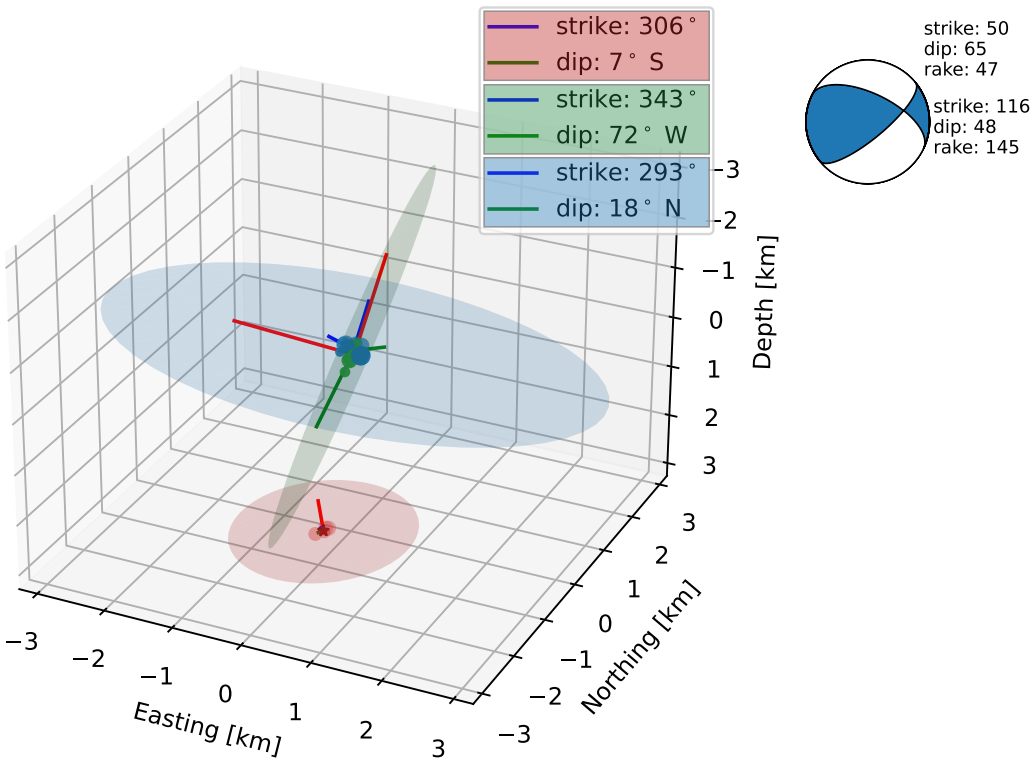

Figure 7.12. Estimated fault plane orientations for the two largest sub-clusters of sequence D, and the moment tensor solution for an event within the first sub-cluster by Gesa Petersen (pers. comm.).

10 August 2018 is part of the largest sub-cluster (in blue colour), while the largest mainshock occurs at the start of the second sequence on 11 August 2018. The second sub-cluster (in orange colour) is activated after the mainshock, and has a magnitude 2.2 M_L event. The third and fourth sub-clusters (in green and red colour) are part of the aftershock series. There is a typical gap between the magnitudes of the largest event and the rest of the aftershock series of about one unit of magnitude, and the activity decays very quickly within two days, with sporadic events up to one year after the main sequence.

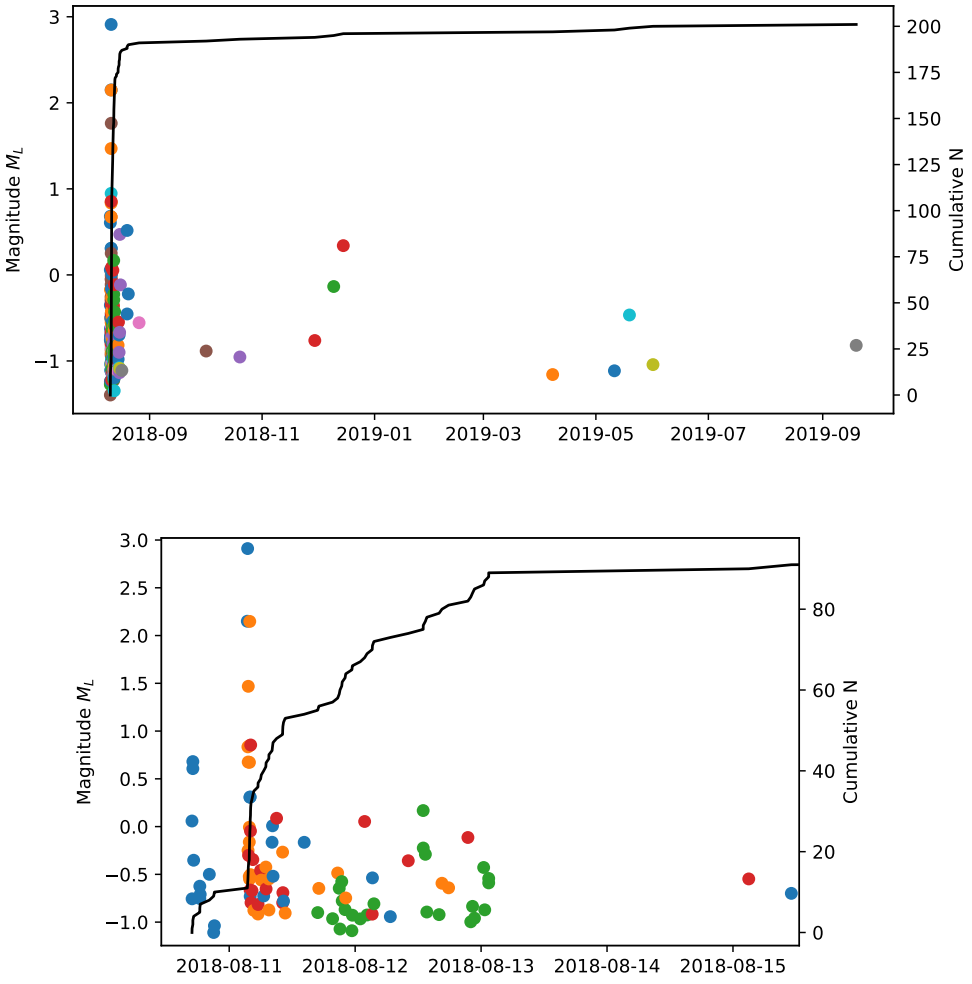

Figure 7.13. Temporal magnitude distribution of all events in sequence D over a period of one year (upper panel), and within the first 4 days from the main sequence (lower panel). Events are coloured by their associated sub-clusters.

Sequence E (1 February 2019)

The third and final earthquake sequence in the Friuli region (E) occurred on 1 February 2019. This sequence comprises 178 events that are located west of the village of Chievolis. The magnitudes in this sequence are extremely low, with the largest event being 0.35 M_L. As illustrated in Figure 7.22, the estimated b-value for this sequence is extremely high due to the limited magnitude range, and the complete absence of larger events, which is very atypical for this region. Due to the low magnitudes, and hence low SNR of the events in this sequence, the number of phase-picks was insufficient for a relative relocation using S-P differential travel-times.

Figure 7.14 shows the original event locations, as well as the graph representation of the cluster, which has a very low maximum modularity (0.11) and shows no indication of sub-clustering. The cluster was therefore not separated into sub-clusters.

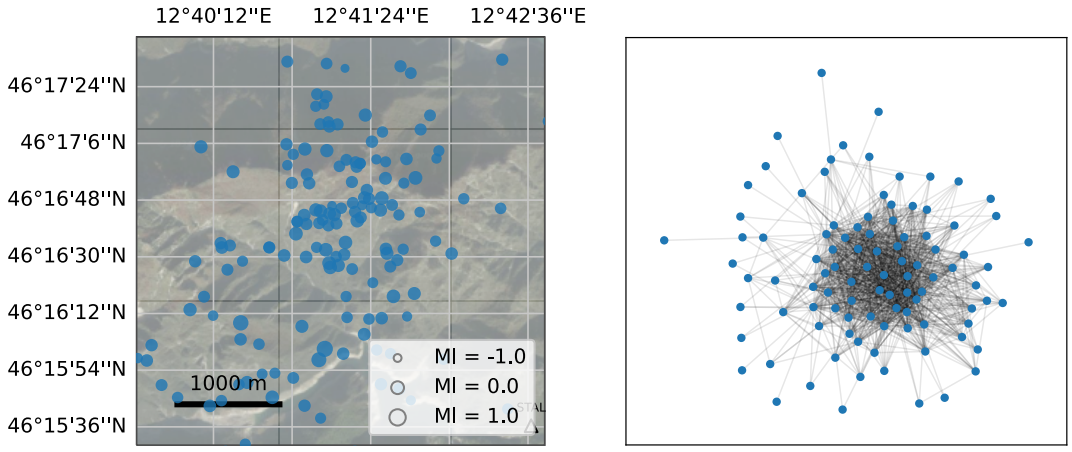

Figure 7.14. Relocated events for earthquake cluster E (left) and the graph representation of the cluster (right).

The temporal distribution of the event magnitudes in the sequence is illustrated in Figure 7.15 and exhibits swarm type characteristics, which is atypical for the region. The entire sequence last a few days with a relatively constant rate. Only 3 events have magnitudes exceeding -0.2 M_L. The timing of the events make them unlikely to be related to industrial activities. However, the locations of the events scatter over an area of about 2.5 km between two hydroelectric reservoirs, suggesting the possibility that they are related to poroelastic stress changes. This would explain most of the unusual characteristics, but is of course highly speculative. The depth of the events is poorly constrained but seems to focus at approximately 11 km.

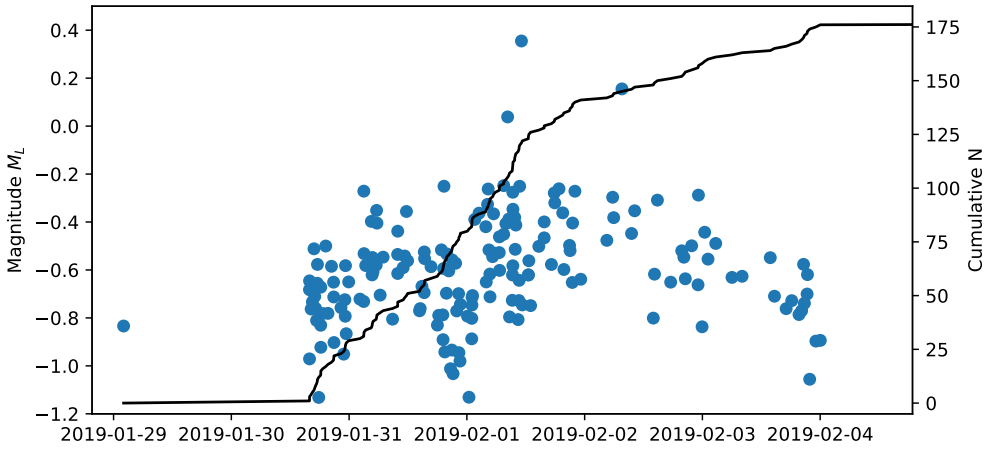

Figure 7.15. Temporal magnitude distribution of all events in sequence E over a period of 6 days.

7.3.2 Engadine and Ortler Alps

Sequence C (25 April 2018)

The seismicity in the Engadine and Ortler Alps is more scattered compared to the Friuli region. Nonetheless, two strong earthquake sequences were recorded by the Swath-D network. The first sequence (C) occurred on 25 April 2018. It comprises 173 events that have a maximum magnitude of 2.13 M_L. The events in this sequence are located in the Münstertal valley in Switzerland, close to the Swiss-Italian border. The graph representation of the cluster yields a maximum modularity of 0.14, and is well connected. A separation of the cluster into sub-clusters was therefore not applied. The relative relocalisation using S-P differential travel-time inversion as described in Section 7.2 was successfully applied. The relocated events, as well as the graph representation of the cluster are illustrated in Figure 7.16. A comparison of the relocated events to the original event locations is made in appendix Figure A19.

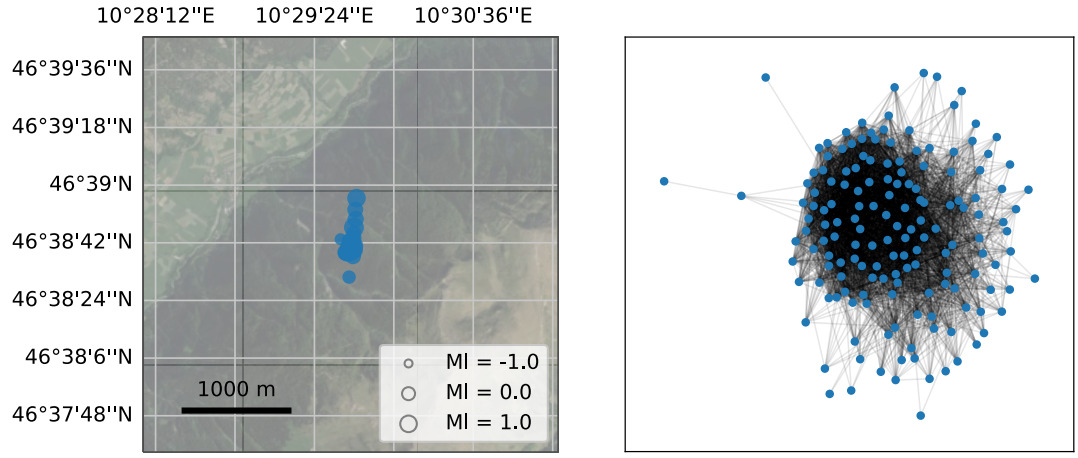

Figure 7.16. Relocated events for earthquake cluster C (left) and the graph representation of the cluster (right).

Based on the eigenvectors of the covariance matrix, I estimated to orientation of a possible fault plane, which fits well with moment tensor inversions for two events within this cluster (Gesa Petersen, pers. comm.). The orientation of the plane is presented in Figure 7.17 together with the moment tensor solutions. These fit very well and indicate left lateral strike-slip faulting on a north-south striking vertical fault.

The temporal distribution of the event magnitudes in the cluster is illustrated in Figure 7.18. This upper panel of this shows that the fault was activated in 4 distinct phases in April 2018, June 2018, July 2018, and again in November 2018, although the last activation caused only a few, very small events. In the lower

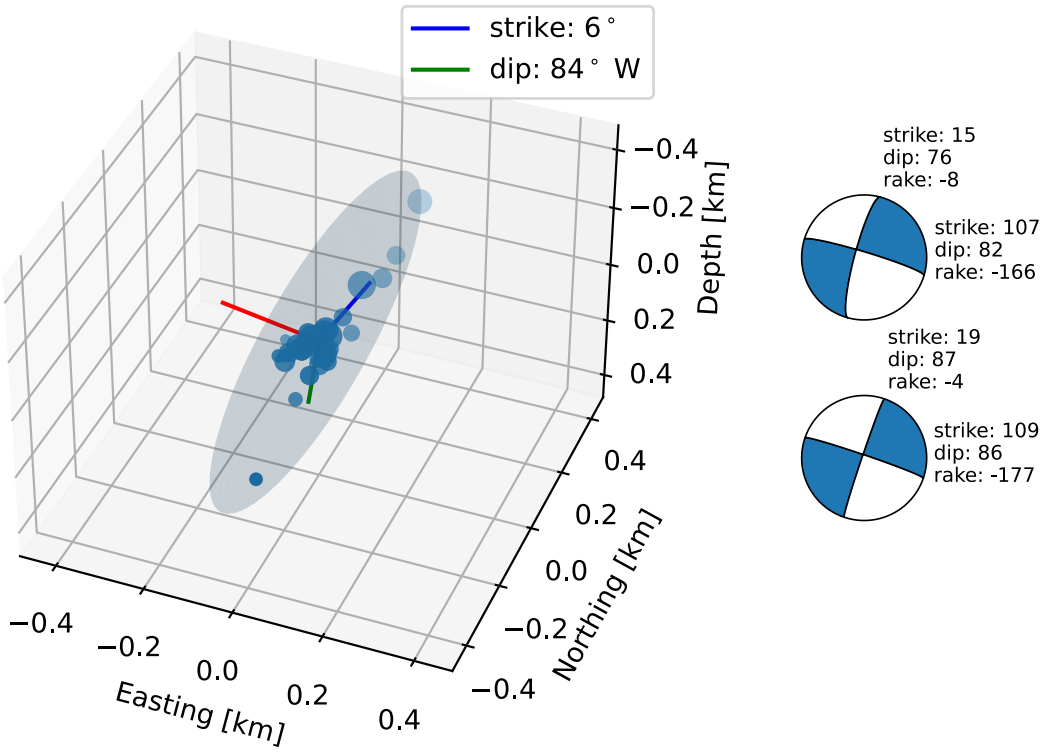

Figure 7.17. Estimated fault plane orientation for clusters C, and the moment tensor solutions for 2 events from this cluster by Gesa Petersen (pers. comm.)

panel of Figure 7.18, a detailed view of the first activation phase is illustrated, revealing 4 bursts of high activity, 3 of which are on 25 April 2018, and one on the next day. These burst of activity are not preceded by a main shock, nor do they exhibit significant aftershock activity. This leads to the conclusion that these are very short-lived swarm sequences.

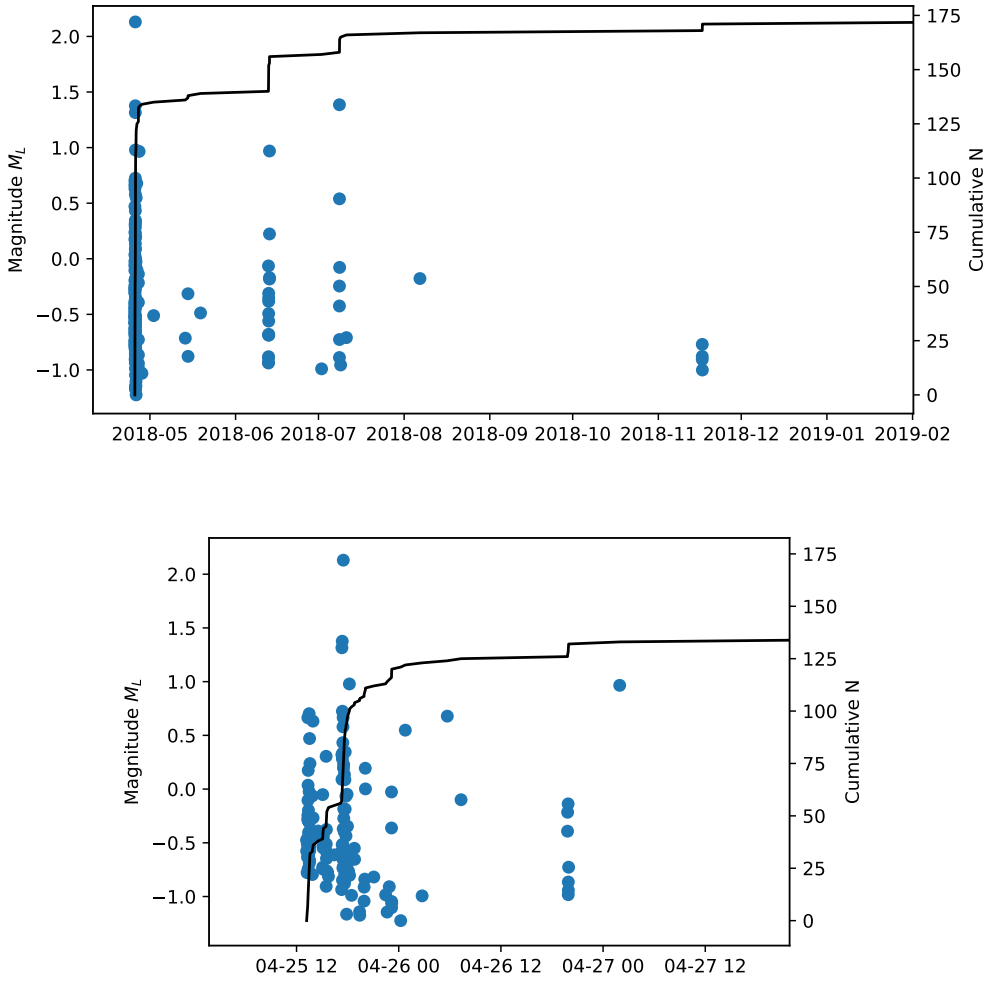

Figure 7.18. Temporal magnitude distribution of all events in sequence C over a period of 10 months (upper panel) and over a period of 2 days during the main event sequence (lower panel).

Sequence F (9 February 2019)

The second sequence (F) occurred on 9 February 2019 in the Suldental valley, about 15 km south-east of the first sequence. The maximum magnitude within this cluster is 1.24 M_L. By applying the Louvain method for community detection as described in Section 7.1, I separated the events of this cluster into 3 sub-clusters in a way that optimises the modularity of the graph. A relative relocalisation of the events was possible for each of the three sub-clusters. The graph representation of this cluster, as well as the spatial distribution of the relocated events coloured by their sub-cluster association, is depicted in Figure 7.19. A comparison of the relocated events to the original event locations is made in appendix Figure A20.

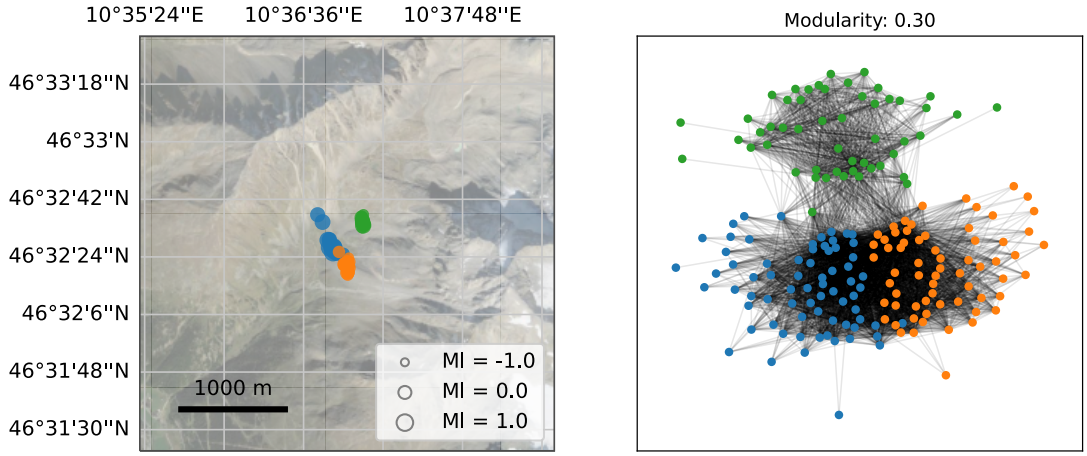

Figure 7.19. Earthquake cluster F split into 3 sub-clusters that optimise the modularity of the graph. The relocated event locations are coloured by their associated sub-clusters in a map view (left), and in the graph representation of the cluster (right).

The orientations of the estimated fault planes for each of the three sub-clusters are illustrated in Figure 7.20. For comparison, the moment tensor solutions of individual events within each of the sub-clusters (Gesa Petersen, pers. comm.) are presented alongside in the same colours. The first and largest sub-cluster (in blue colour) exhibits normal faulting with a varying amount of strike-slip. The second sub-cluster (in orange colour) has a slightly more pronounced strike-slip component and the fault-plane is rotated with respect to the first sub-cluster. The third sub-cluster (in green colour) exhibits pure left-lateral strike-slip on a vertical, north-south striking fault.

The temporal distribution of the event magnitudes in this cluster is illustrated in Figure 7.21. This upper panel of this shows that the faults were activated multiple times between February 2019 and April 2019. In the lower panel of Figure 7.21,

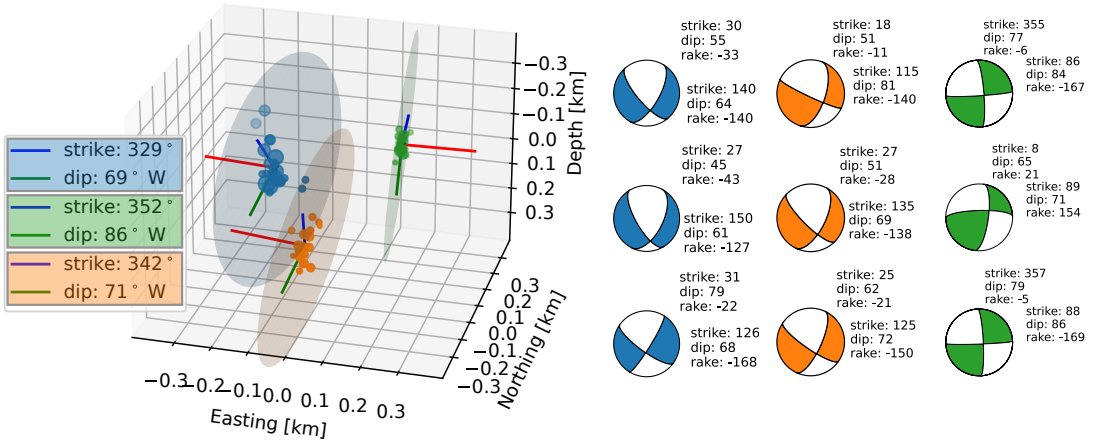

Figure 7.20. Estimated fault plane orientations for the three sub-clusters of sequence F, and moment tensor solutions of individual faults within these sub-clusters by Gesa Petersen (pers. comm.).

it can be observed that the different faults are activated one after another. While most of the activity before and after the main sequence is attributed to the first (normal faulting) sub-cluster (in blue colour), the main sequence has three different phases. The first and longest phase is attributed to the third sub-cluster (strike-slip, in green colour), whereas the second and third phase are attributed to the second sub-cluster (normal faulting with strike-slip component, in orange colour). None of the sequences contain clear main-shocks, making it more of a swarm-type cluster.

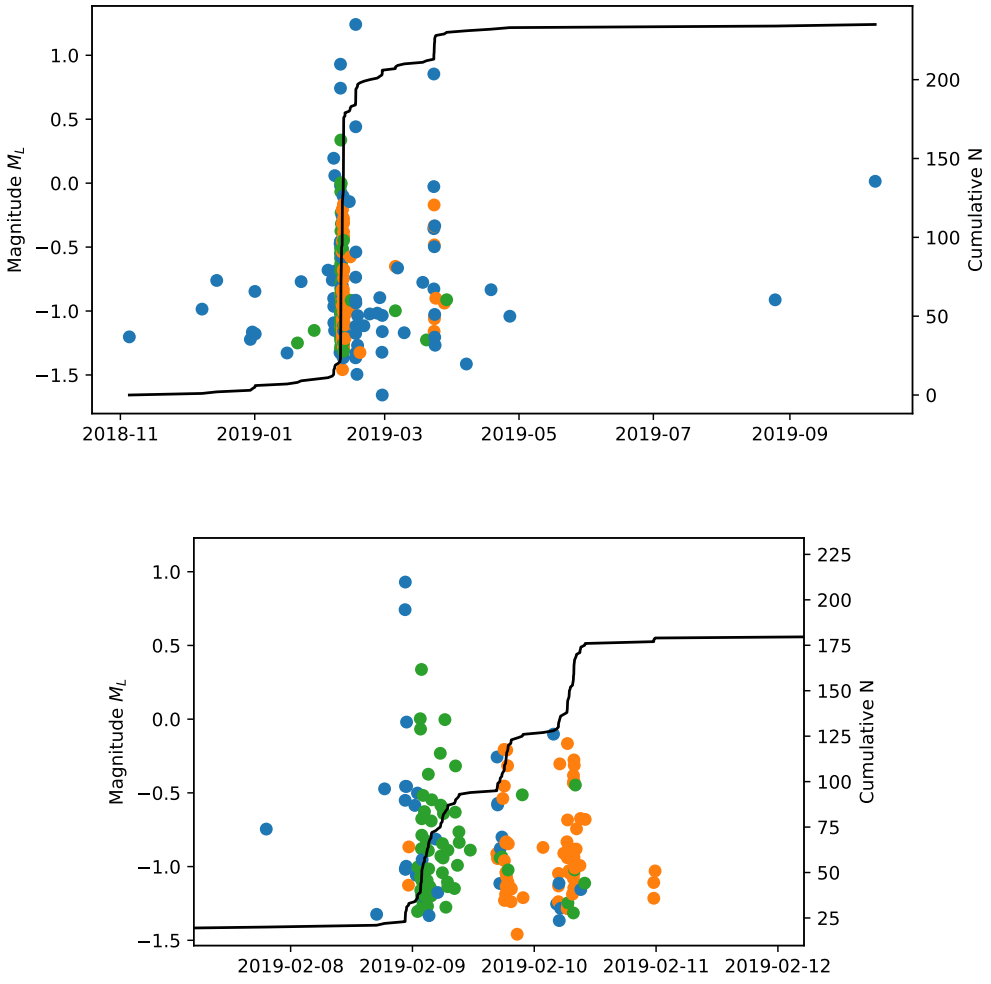

Figure 7.21. Temporal magnitude distribution of all events in sequence F over a period of 7 months (upper panel), and within the 4 days surrounding the main event sequence (lower panel). Events are coloured by their associated sub-clusters.

7.3.3 Comparison of the b-values

In the Friuli region, clusters B and D yield relatively low b-values as illustrated in Figure 7.22, which signifies high differential stress in the crust. This fits well with the regional b-value as shown in Figure 6.8. These clusters comprise typical mainshock-aftershock sequences. The b-value for cluster E is abnormally high and atypical for the region. This could be caused by changes in the poroelastic stress conditions caused by two nearby hydroelectric reservoirs between which the seismicity occurred. However, this possibility would have to be studied in much more detail.

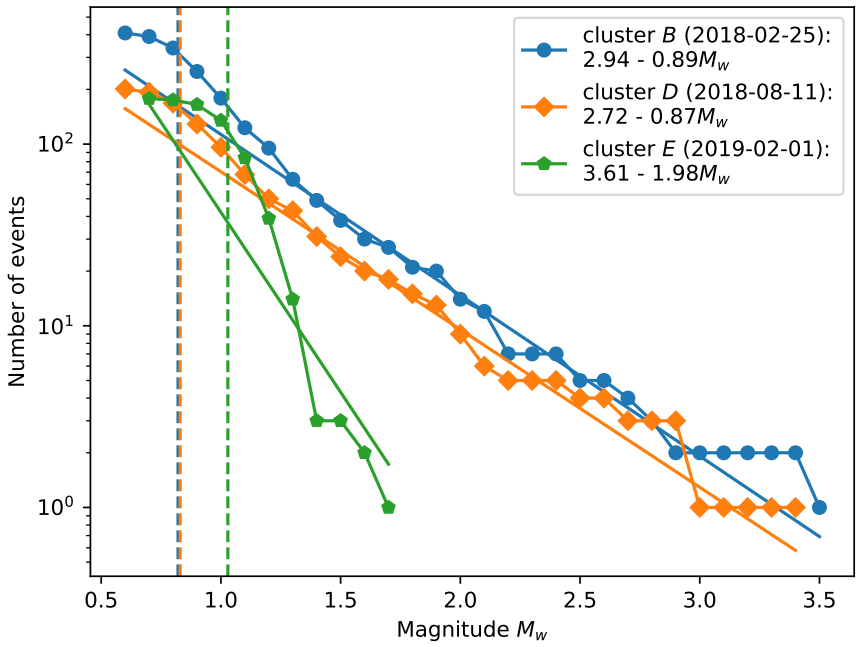

Figure 7.22. Frequency magnitude distributions for the three earthquake sequences (B, D, and E) in the Friuli region with estimated b-values.

The earthquake clusters in the Engadine and Ortler Alps show elevated b-values (7.23). This fits to the overall b-value for the region as shown in Figure 6.8. Both are swarm-type sequences, as they lack the typical mainshock-aftershock characteristics seen in the Friuli region. The high seismicity rate in this region is most likely linked to the high uplift rate caused by glacial isostatic rebound.

The methods that I presented in this chapter, and in particular their combination into a systematic workflow, have allowed a dramatic increase in the local resolution of the seismicity catalogue. Whereas the events in the original catalogue have horizontal uncertainties of about 1 km, the relative relocalisation based on

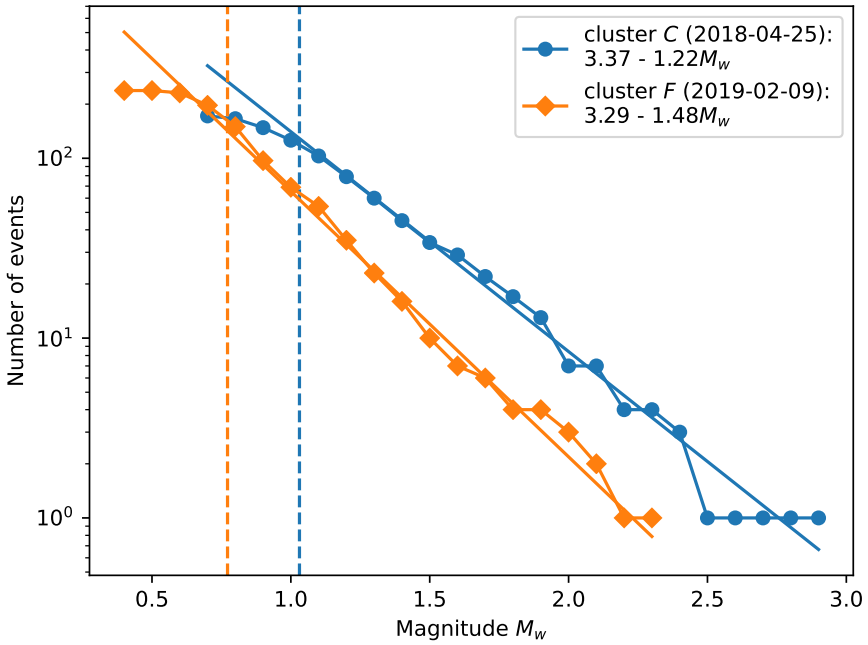

Figure 7.23. Frequency magnitude distributions for the two earthquake sequences (C and F) in the Engadine and Ortler Alps region with estimated b-values.

S-P differential travel times reduced these by about two orders of magnitude. This result could only be achieved by the inventive application of graph theory, which I used to break down seismicity clusters into sub-clusters. This workflow allowed me to relocate closely located events to individual segments within complex fault systems. The orientation of these fault segments generally agreed well with moment tensor inversions for individual events within the sub-clusters.

CHAPTER 8

Conclusions

The objective of this thesis was to analyse the spatio-temporal distribution of seismicity in the Eastern Alps. Despite routine seismic monitoring being conducted by a number of local agencies across different parts of the region, the station density of the local permanent networks varies. This obstructs a uniform approach to earthquake detection on a regional scale. The recent AlpArray Swath-D experiment comprised a dense and uniformly spaced network of 163 seismic stations. For the first time, this enabled the development of a comprehensive and uniformly processed earthquake catalogue for the Eastern Alps.

Utilising data from a combined total of 200 stations from the Swath-D network, as well as the local AlpArray backbone stations, I developed a successful workflow for the detection, localisation, and analysis of low-magnitude seismicity. Based on a starting catalogue compiled from regional public catalogues and additional energy-based detections, I was able to detect 15,155 unique events within the two-year time-span of the Swath-D network, from late 2017 to late 2019, based on template matching. This required the development of a highly efficient code, which I accomplished by developing a parallelised, GPU-accelerated Python code. The results demonstrate that template matching is an excellent method to detect very small earthquakes, with a magnitude up to 4 units below that of the master event used as input, and at distances of up to 10 km from these events.

Using innovative waveform based methods, I was able to accurately pick and relocate 7,712 events. I estimated the location errors to be about 1 km horizon-

tally and 1.5 km vertically. I classified these events into earthquakes (6,053) and anthropogenic events (1,659) based on the temporal signatures of the clusters in which they appear. I estimated the size of the earthquakes by applying the local magnitude scale, yielding magnitudes between -1.7 $\leq M_L \leq$ 3.7, with a completeness magnitude of -1.0M_L.

The spatial distribution of earthquakes in the study area follows the known deformation patterns from long-term seismic monitoring. The most seismically active part is the Friuli region, with high seismicity rates, strong spatio-temporal clustering and frequent $M_L \geq 3$ events. Earthquake clusters in this region are found to be mainly mainshock-aftershock type sequences. Frequent $M_L \geq 2$ earthquakes also occur in the Giudicarie-Lessini region, albeit with a much lower overall seismicity rate compared to the Friuli region. GPS studies confirm that the deformation rates are the highest along the southern margin of the study area, peaking in the Friuli region. A surprisingly high seismicity rate was found in the Engadine and Ortler Alps, but the earthquakes in this region do not exceed magnitude M_L 2. This results in a slightly unusual frequency magnitude distribution characterised by a large b-value. The seismicity in this region shows strong spatio-temporal clustering, with mostly swarm type sequences. Recent GPS studies found that this area is subject to high uplift rates, most probably due to postglacial isostatic rebound. The Dolomite indenter and Tauern Window are known to be seismically quiet areas. However, due to the high sensitivity to low-magnitude earthquakes in my workflow, I was able to detect more earthquakes in these regions. The high b-value of the frequency magnitude distribution observed in the Tauern Window can be attributed to the particularly dense metamorphic rocks in the region. Additionally, existing faults in the region are thought to be unfavourably oriented to be triggered in the prevailing stress conditions, explaining the lack of any larger earthquakes.

In exploring novel, innovative approaches to the analysis of small-magnitude seismicity, I employed techniques derived from graph theory. The construction of graph representations of earthquake clusters enabled me to differentiate closely located earthquakes into sub-clusters based on the optimisation of the modularity. By relocating the events within these sub-clusters based on S-P differential travel-time inversion, I was able to resolve the geometries of individual fault segments within complex fault systems with a precision in the order of 10 m. The orientation of these fault planes was found to be in good agreement with independently calculated moment tensor inversions for earthquakes within each of the sub-clusters.

CHAPTER 9

Outlook

The template matching code that I developed specifically for the case study of the Swath-D network in the Eastern Alps can be extended to other regions with optional slight adaptations. For example in Folesky et al. (2024), I applied the code to the catalogue published by Sippl et al. (2023) using the IPOC network in northern Chile (GFZ German Research Centre For Geosciences and Institut Des Sciences De L'Univers-Centre National De La Recherche CNRS-INSU, 2006). Because of the larger spatial extent of the network, template waveforms need to have variable length to account for the variable length of the earthquake signals depending on the station's hypocentral distance. Using over $180,000$ template events, I detected $1,836,195$ unique events. Our work on this dataset is ongoing and has shifted towards the analysis of repeating earthquakes (i.e. multiplets with extremely high waveform similarity), for which the method is evidently well suited.

The deployment of machine learning has been demonstrated to be increasingly successful in many seismological applications (e.g. Woollam et al., 2022). However, it has been shown that template matching catalogues are more complete than comparable deep learning catalogues (Scotto di Uccio et al., 2022). Particularly, in a challenging scenario such as the Eastern Alps (low-magnitude character of the seismicity combined with the elevated background noise levels in the Swath-D dataset), a template matching approach is therefore preferable over the current pre-trained neural network-based algorithms (Jannes Münchmeyer, pers. comm.). An interesting experiment would be to train a neural network-based al-

gorithm specifically for this scenario by using the seismicity catalogue published in Hofman, Kummerow, Cesca, and the AlpArray-Swath-D Working Group (2023) and subsequently assess its accuracy relative to the template matching catalogue. Another potential machine learning application would be the automatic classification of events as described in Chapter 4. The seismicity catalogue published in Hofman, Kummerow, Cesca, and the AlpArray-Swath-D Working Group (2023) could be used to create a labelled training dataset for this purpose.

The analysis of seismicity in the Eastern Alps in this thesis was limited to the time span of the AlpArray Swath-D network. Extending the catalogue in either direction would create a drop in resolution outside the availability window of the Swath-D network. However, when looking at individual clusters of seismicity, such as the ones discussed in Chapter 7, one might investigate their long term temporal behaviour by extending the template matching period using permanent stations. Locations for newly detected events could be calculated using relative relocation methods as described in Section 7.2. As demonstrated in this thesis, high location precision can be achieved with a relatively low number of stations. The longer time span would allow the investigation of seasonal and long-term temporal variations, as well as provide more data for statistical analysis of the frequency magnitude distribution. Also, the research area could be extended towards the east by including the DSEBRA stations (D154 to D163) that are part of the Swath-D network (Schlömer et al., 2022). The reason for excluding these stations was their deployment at a considerably later point in time, which would compromise the uniformity of the catalogue over time.

The application of graph theory has proven to be a valuable tool for the analysis of seismicity clusters, with significant room for further expansion. It would be interesting to explore the relationship between the connectivity of a graph based on waveform similarity and the geometry of the fault or fault network on which the earthquakes occur. Useful properties to investigate could be the eigenvalues and corresponding eigenvectors of the graph's Laplacian matrix, which is also referred to as spectral graph theory.

Finally, it would be interesting to study the source of the earthquake cluster from 1 February 2019 in Friuli in more detail, because it shows such unusual characteristics for the region. An analysis over a longer period of time might reveal more activity, which could exhibit seasonal variation or migration patterns.

Appendices

Appendix A: Additional figures and data

Table A1. List of stations used in this thesis.

Identifiers		Location				P-picks		S-picks	
Net	**Station**	**Lon**	**Lat**	**Alt. [m]**	**Picked events**	**N**	**RMS [s]**	**N**	**RMS [s]**
BW	SCE	11.709	47.038	1730	96	58	.049	84	.089
CH	BERNI	10.023	46.414	2311	440	414	.058	257	.073
CH	FUORN	10.264	46.620	2286	1073	1004	.063	680	.087
IV	BRMO	10.372	46.476	1380	770	576	.065	652	.097
IV	CTI	11.650	46.048	1180	306	259	.070	133	.146
IV	FVI	12.780	46.597	1024	114	78	.051	80	.098
IV	MABI	10.514	46.055	1853	40	34	.034	22	.120
IV	MAGA	10.629	45.775	1265	75	73	.058	41	.052
IV	PTCC	13.354	46.407	700	496	402	.070	338	.098
IV	ROVR	11.072	45.647	1316	54	49	.037	33	.045
IV	SALO	10.524	45.618	600	26	26	.026	15	.051
IV	STAL	12.710	46.260	625	626	523	.057	450	.103
NI	PALA	12.924	46.245	1280	544	394	.069	415	.102
NI	POLC	12.501	46.027	150	170	145	.072	74	.124
NI	PURA	12.742	46.426	1417	518	257	.065	395	.136
NI	VINO	13.275	46.254	608	549	462	.065	410	.089
OE	ABTA	12.512	46.747	1041	154	132	.058	90	.127
OE	KBA	13.345	47.078	1721	246	214	.061	147	.122
OE	MYKA	13.642	46.630	909	757	692	.066	471	.093
OX	ACOM	13.514	46.548	1788	428	402	.077	191	.105
OX	AGOR	12.047	46.283	631	7	6	.053	1	.042
OX	BAD	13.244	46.234	590	777	629	.061	609	.103
OX	BALD	10.819	45.683	1911	200	164	.046	132	.070
OX	BOO	13.098	46.319	444	1085	895	.059	932	.089
OX	CAE	12.438	46.009	870	341	277	.074	248	.108
OX	CGRP	11.805	45.881	1757	164	146	.049	110	.093
OX	CIMO	12.445	46.312	710	1440	1194	.066	1313	.111
OX	CLUD	12.881	46.457	635	955	714	.074	713	.102
OX	FUSE	13.001	46.414	520	970	846	.064	632	.075
OX	MARN	11.210	45.638	785	240	214	.048	173	.069
OX	MLN	12.615	46.150	814	825	599	.083	557	.111
OX	MPRI	12.988	46.241	762	854	751	.064	572	.090
OX	PLRO	13.148	46.549	1410	863	749	.084	597	.113
OX	PRED	13.565	46.443	902	128	105	.074	72	.129
OX	VARN	12.105	45.992	1265	307	296	.068	173	.083
OX	ZOU2	12.973	46.558	1911	941	874	.068	566	.090
RF	GEPF	13.139	46.275	255	698	527	.066	546	.096

Continued on next page

Table A1. – continued from previous page

Identifiers		Location				P-picks		S-picks	
Net	Station	Lon	Lat	Alt. [m]	Picked events	N	RMS [s]	N	RMS [s]
SI	KOSI	11.378	46.463	1604	81	70	.074	19	.096
SI	LUSI	10.944	45.959	860	723	669	.064	288	.088
SI	MOSI	10.550	46.616	1957	978	746	.062	744	.091
SI	RISI	12.079	46.948	1785	.	.	nan	.	nan
SI	ROSI	11.412	46.928	1917	340	312	.059	229	.101
ST	DOSS	11.188	45.881	1660	561	528	.068	247	.074
ST	GAGG	10.959	46.084	1617	698	649	.061	195	.092
Z3	A027A	14.007	46.816	1217	767	716	.063	321	.122
Z3	A028A	13.996	47.103	1105	.	.	nan	.	nan
Z3	A029A	13.761	47.430	992	79	77	.062	30	.057
Z3	A034A	13.079	46.909	1050	134	130	.062	49	.086
Z3	A035A	12.721	47.197	1652	1	.	nan	1	.021
Z3	A290A	10.903	46.507	1729	675	570	.086	453	.121
Z3	A291A	11.880	46.625	1568	61	53	.066	22	.175
ZS	D001	10.225	45.899	259	65	58	.055	44	.079
ZS	D002	10.453	45.920	1569	156	141	.051	112	.098
ZS	D003	10.622	45.957	1223	168	159	.064	81	.092
ZS	D004	10.809	46.017	840	336	256	.063	187	.104
ZS	D005	11.165	46.089	646	672	642	.044	337	.093
ZS	D006	11.345	46.131	1385	558	545	.049	369	.081
ZS	D007	11.539	46.170	1822	470	407	.071	338	.160
ZS	D008	11.695	46.226	1291	68	59	.057	46	.111
ZS	D009	11.931	46.208	1142	97	70	.074	68	.112
ZS	D010	12.299	46.289	692	877	687	.079	691	.102
ZS	D011	12.470	46.363	1025	107	97	.061	95	.071
ZS	D012	12.625	46.400	886	1073	936	.069	833	.092
ZS	D013	13.024	46.481	548	606	438	.078	374	.096
ZS	D014	13.205	46.544	1175	748	609	.086	484	.124
ZS	D015	13.390	46.576	1449	244	198	.067	147	.130
ZS	D016	13.584	46.607	769	.	.	nan	.	nan
ZS	D017	13.753	46.630	808	745	673	.037	448	.076
ZS	D018	13.961	46.689	647	709	666	.056	425	.103
ZS	D019	14.146	46.722	599	728	646	.087	438	.113
ZS	D020	10.325	46.015	545	56	41	.044	37	.115
ZS	D021	10.707	46.101	1324	285	266	.056	76	.114
ZS	D022	10.806	46.147	1786	232	165	.069	123	.136
ZS	D023	11.023	46.188	826	661	622	.057	465	.113
ZS	D024	11.232	46.208	1058	740	716	.044	468	.080

Continued on next page

Table A1. – continued from previous page

Identifiers		Location				P-picks		S-picks	
Net	Station	Lon	Lat	Alt. [m]	Picked events	N	RMS [s]	N	RMS [s]
ZS	D025	11.414	46.246	967	312	286	.066	182	.132
ZS	D026	11.605	46.326	1293	222	201	.081	53	.171
ZS	D027	11.786	46.327	1736	101	86	.052	77	.112
ZS	D028	11.982	46.378	823	102	73	.105	60	.109
ZS	D029	12.171	46.387	1475	265	208	.073	152	.125
ZS	D031	12.507	46.486	1143	173	110	.063	120	.117
ZS	D032	12.714	46.525	1003	770	572	.083	660	.124
ZS	D033	12.894	46.566	1920	741	551	.069	528	.096
ZS	D034	13.050	46.615	1185	413	330	.064	254	.102
ZS	D035	13.272	46.639	1028	294	229	.071	169	.121
ZS	D036	13.441	46.682	953	.	.	nan	.	nan
ZS	D037	13.637	46.745	745	436	360	.068	293	.102
ZS	D038	13.849	46.754	1150	481	437	.059	235	.111
ZS	D039	10.139	46.112	1274	142	112	.067	103	.136
ZS	D040	10.352	46.151	666	4	1	.000	4	.089
ZS	D041	10.479	46.207	1578	289	274	.060	100	.171
ZS	D042	10.736	46.219	2138	99	81	.082	48	.130
ZS	D043	10.862	46.297	1456	91	65	.058	37	.092
ZS	D044	11.092	46.318	789	298	250	.065	137	.143
ZS	D045A	11.238	46.348	347	486	454	.069	159	.138
ZS	D046	11.406	46.393	1462	.	.	nan	.	nan
ZS	D047	11.640	46.447	1967	46	27	.071	38	.125
ZS	D048	11.767	46.478	1464	37	26	.095	23	.150
ZS	D049	11.987	46.504	1737	84	49	.074	65	.157
ZS	D050	12.175	46.527	2234	86	75	.057	36	.103
ZS	D051	12.378	46.578	959	226	164	.080	147	.108
ZS	D052	12.525	46.605	1129	258	165	.097	197	.127
ZS	D053	12.764	46.690	1327	185	142	.066	89	.097
ZS	D054	12.908	46.690	1151	280	234	.083	117	.146
ZS	D055	13.085	46.744	640	36	22	.046	22	.120
ZS	D056	13.334	46.779	1051	128	109	.066	59	.085
ZS	D057	13.480	46.813	632	71	52	.059	33	.116
ZS	D058	13.671	46.838	1262	738	620	.073	440	.107
ZS	D059	13.877	46.921	1760	790	731	.079	464	.117
ZS	D060	14.032	46.945	1483	244	228	.065	154	.079
ZS	D061	10.225	46.238	526	71	58	.053	34	.063
ZS	D062	10.395	46.251	1346	357	337	.052	70	.111
ZS	D063	10.551	46.299	1757	411	382	.053	154	.134

Continued on next page

Table A1. – continued from previous page

Identifiers		Location				P-picks		S-picks	
Net	Station	Lon	Lat	Alt. [m]	Picked events	N	RMS [s]	N	RMS [s]
ZS	D064	10.784	46.326	1485	366	273	.080	204	.150
ZS	D065	11.018	46.440	936	211	154	.079	142	.125
ZS	D066	11.118	46.456	931	112	87	.047	72	.116
ZS	D067	11.506	46.513	837	39	29	.029	27	.134
ZS	D068	11.647	46.574	1167	25	20	.032	6	.116
ZS	D069	12.042	46.638	1534	17	10	.050	8	.129
ZS	D070	12.220	46.676	1344	20	8	.034	17	.079
ZS	D071	12.436	46.743	1201	87	64	.064	51	.119
ZS	D072	12.589	46.777	1168	163	152	.054	111	.091
ZS	D073	12.756	46.808	686	25	18	.023	14	.059
ZS	D074	12.946	46.852	898	91	84	.057	46	.106
ZS	D075	13.195	46.865	1202	53	46	.043	27	.111
ZS	D076	13.313	46.919	1519	14	14	.045	1	.021
ZS	D077	13.511	46.975	1606	101	88	.064	50	.105
ZS	D078	13.689	46.981	1421	314	284	.068	94	.093
ZS	D079	13.905	47.049	1168	259	226	.065	133	.101
ZS	D081	10.249	46.374	1696	613	521	.061	416	.112
ZS	D082	10.448	46.430	1857	1041	897	.068	774	.100
ZS	D083	10.579	46.453	2706	1065	909	.059	898	.098
ZS	D084	10.827	46.484	1897	411	288	.079	329	.140
ZS	D085	11.163	46.576	666	237	202	.068	139	.080
ZS	D086	11.355	46.641	969	94	65	.076	63	.080
ZS	D087	11.543	46.654	1293	160	149	.059	71	.094
ZS	D088	11.689	46.667	1511	29	28	.026	1	.002
ZS	D089	11.909	46.738	1727	67	63	.033	15	.144
ZS	D090	12.091	46.771	1404	77	49	.058	56	.093
ZS	D091	12.264	46.807	1834	71	59	.052	51	.098
ZS	D092	12.462	46.828	1561	162	150	.060	111	.103
ZS	D093	12.633	46.883	1226	166	136	.047	114	.084
ZS	D094	12.867	46.935	1423	187	173	.073	81	.108
ZS	D095	12.975	46.964	1980	160	149	.056	70	.105
ZS	D096	13.186	47.014	1271	42	31	.076	29	.056
ZS	D097	13.550	47.089	1086	59	48	.061	27	.068
ZS	D098	13.735	47.138	1099	59	48	.046	26	.098
ZS	D099	13.927	47.150	1280	167	156	.067	90	.078
ZS	D100	10.099	46.478	1949	336	310	.074	220	.078
ZS	D101	10.274	46.487	1520	646	492	.089	412	.117
ZS	D102	10.453	46.531	2852	1011	634	.082	873	.102

Continued on next page

Table A1. – continued from previous page

Identifiers		Location				P-picks		S-picks	
Net	Station	Lon	Lat	Alt. [m]	Picked events	N	RMS [s]	N	RMS [s]
ZS	D103	10.631	46.612	968	779	698	.063	611	.081
ZS	D104	10.830	46.625	711	696	600	.081	338	.113
ZS	D105	10.991	46.648	528	43	36	.075	18	.112
ZS	D106	11.203	46.708	778	180	149	.080	92	.092
ZS	D107	11.408	46.778	1457	290	252	.062	215	.095
ZS	D108	11.548	46.813	847	23	10	.057	17	.159
ZS	D109	11.739	46.824	1138	149	82	.067	124	.180
ZS	D110	11.947	46.863	847	21	19	.094	6	.091
ZS	D111	12.116	46.871	1323	60	47	.049	46	.100
ZS	D112	12.311	46.918	1714	97	70	.055	62	.087
ZS	D113	12.510	46.989	1160	145	133	.048	102	.076
ZS	D114	12.689	47.022	1875	66	61	.040	45	.083
ZS	D115	12.877	47.068	1900	65	53	.066	36	.123
ZS	D116	13.079	47.129	1204	23	7	.017	22	.064
ZS	D117	13.216	47.161	1449	200	183	.060	128	.081
ZS	D118	13.419	47.186	1484	179	156	.063	72	.138
ZS	D119	13.578	47.238	1707	71	54	.069	39	.101
ZS	D120	13.804	47.242	1284	112	102	.072	46	.100
ZS	D122	10.169	46.588	1830	19	16	.042	14	.046
ZS	D123	10.513	46.690	1300	691	539	.082	525	.098
ZS	D124	10.685	46.726	1821	445	283	.080	338	.088
ZS	D125	10.826	46.741	1947	416	379	.079	173	.123
ZS	D126	11.104	46.803	1674	282	263	.053	146	.058
ZS	D127	11.259	46.820	1004	343	318	.055	218	.097
ZS	D128	11.421	46.877	1248	243	203	.068	152	.107
ZS	D129	11.638	46.976	1498	164	140	.049	107	.105
ZS	D130	11.783	46.952	1850	178	128	.083	155	.122
ZS	D131	11.980	46.995	1049	27	17	.073	12	.089
ZS	D132	12.129	47.051	1617	30	29	.042	13	.123
ZS	D133	12.332	47.043	1880	84	75	.048	41	.078
ZS	D134	12.539	47.091	1658	10	9	.027	4	.028
ZS	D135	12.937	47.184	1050	35	17	.056	21	.146
ZS	D136	13.059	47.228	1806	178	172	.047	120	.097
ZS	D137	13.311	47.278	1216	221	203	.040	199	.075
ZS	D138	13.492	47.265	1294	113	109	.084	20	.083
ZS	D139	13.663	47.354	960	66	51	.050	38	.089
ZS	D140	10.970	45.605	667	120	86	.054	79	.084
ZS	D141	11.024	45.755	337	286	240	.043	219	.079

Continued on next page

Table A1. – continued from previous page

Identifiers		Location				P-picks		S-picks	
Net	Station	Lon	Lat	Alt. [m]	Picked events	N	RMS [s]	N	RMS [s]
ZS	D145	12.808	46.143	197	208	184	.091	106	.121
ZS	D146	11.024	45.921	366	239	166	.063	177	.086
ZS	D147	11.320	45.961	1364	236	126	.075	178	.104
ZS	D148	11.523	46.037	429	248	125	.064	165	.128
ZS	D149	11.750	46.060	789	188	162	.069	115	.080
ZS	D150	11.984	46.095	588	189	136	.075	135	.129
ZS	D151	12.185	46.155	476	257	191	.069	210	.093
ZS	D152	12.417	46.193	1144	1186	896	.077	1011	.110
ZS	D153	12.813	46.299	448	798	664	.073	585	.101

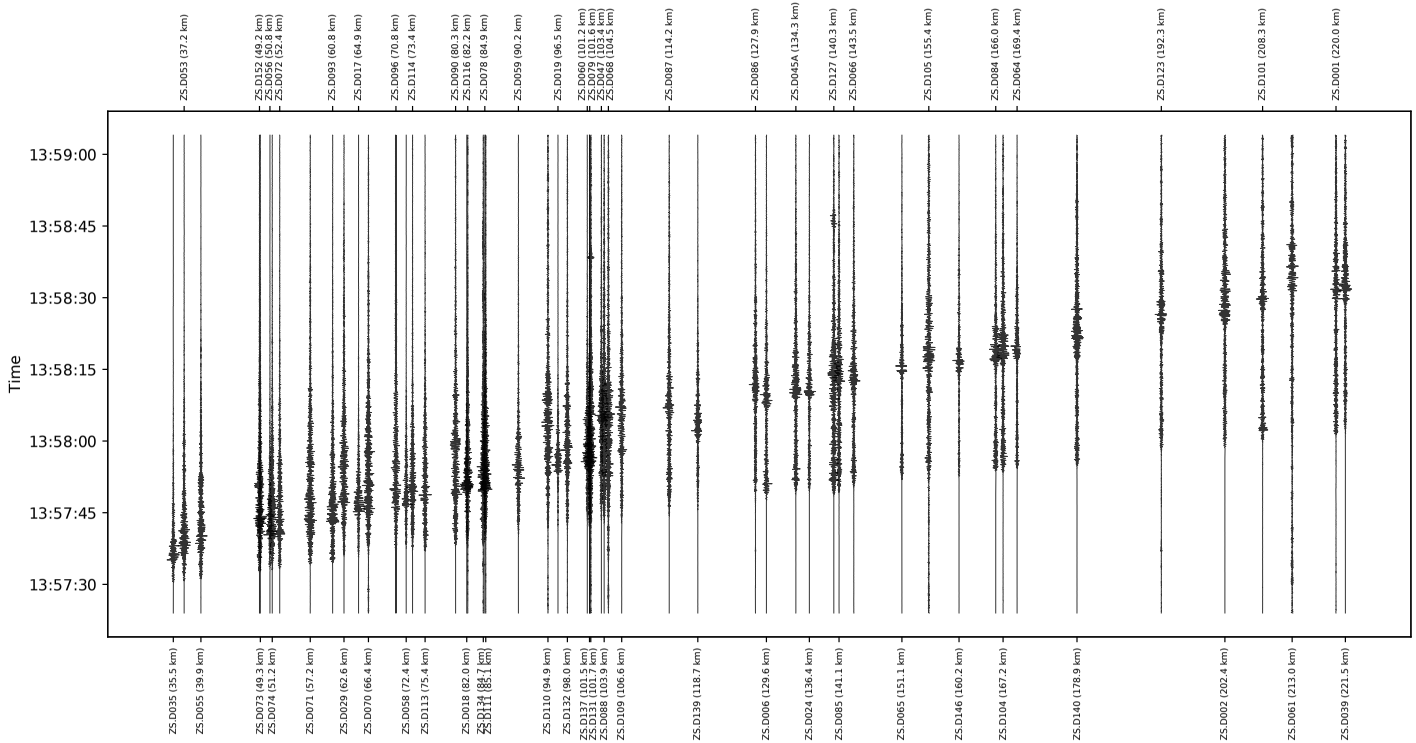

Figure A1. Vertical channel event waveforms for all available online stations of the Swath-D network (ZS) for a relatively large earthquake of magnitude M_w 3.7 that took place near the village of Tolmezzo in Friuli, Italy on 14 June 2019 at 13:57:24 (UTC). Stations are sorted by distance from left to right. The waveform data is band-pass-filtered between $2 - 8$ Hz.

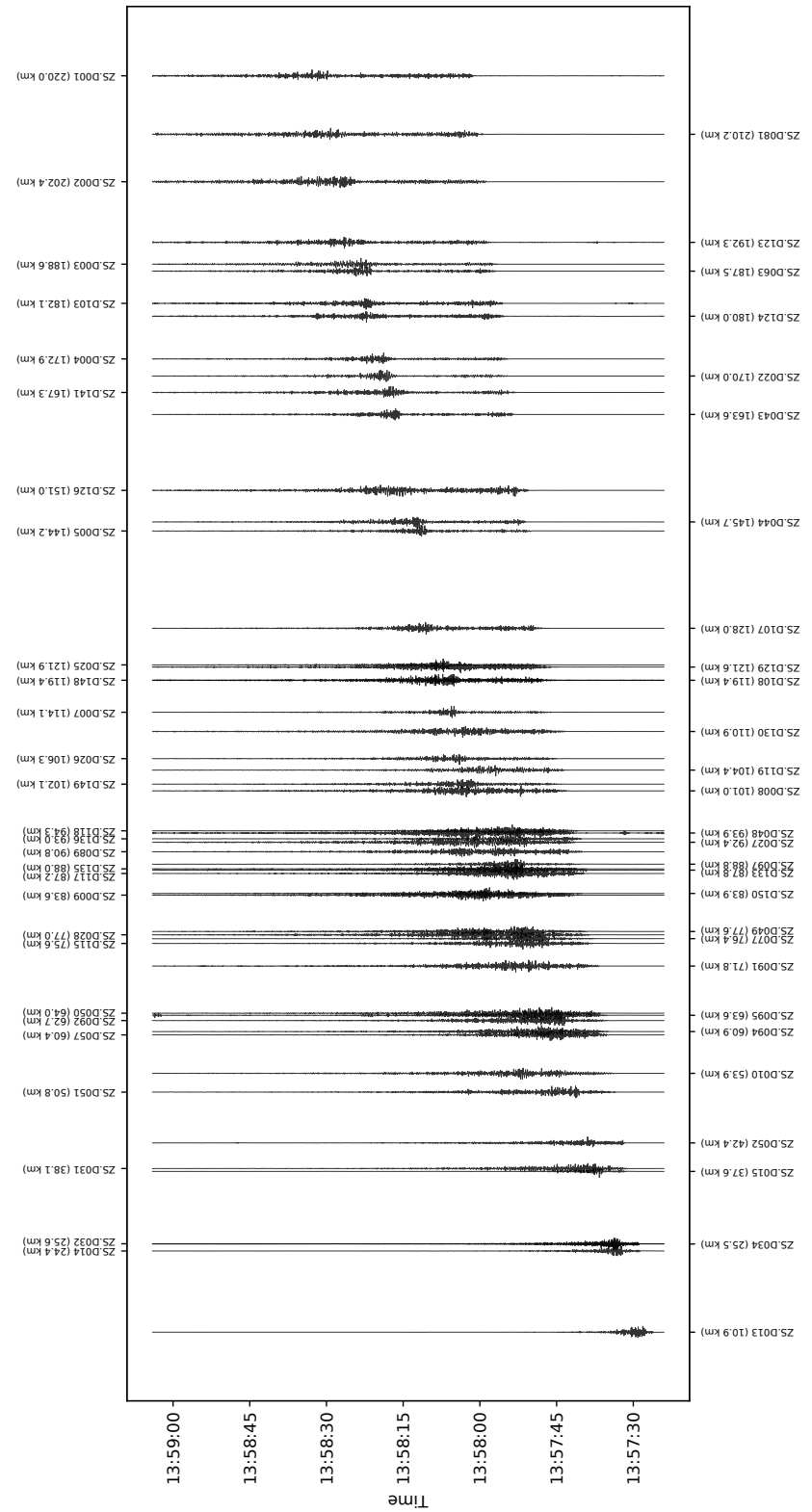

Figure A2. Vertical channel event waveforms for all available offline stations of the Swath-D network (ZS) for a relatively large earthquake of magnitude M_w 3.7 that took place near the village of Tolmezzo in Friuli, Italy on 14 June 2019 at 13:57:24 (UTC). Stations are sorted by distance from left to right. The waveform data is band-pass-filtered between $2 - 8$ Hz.

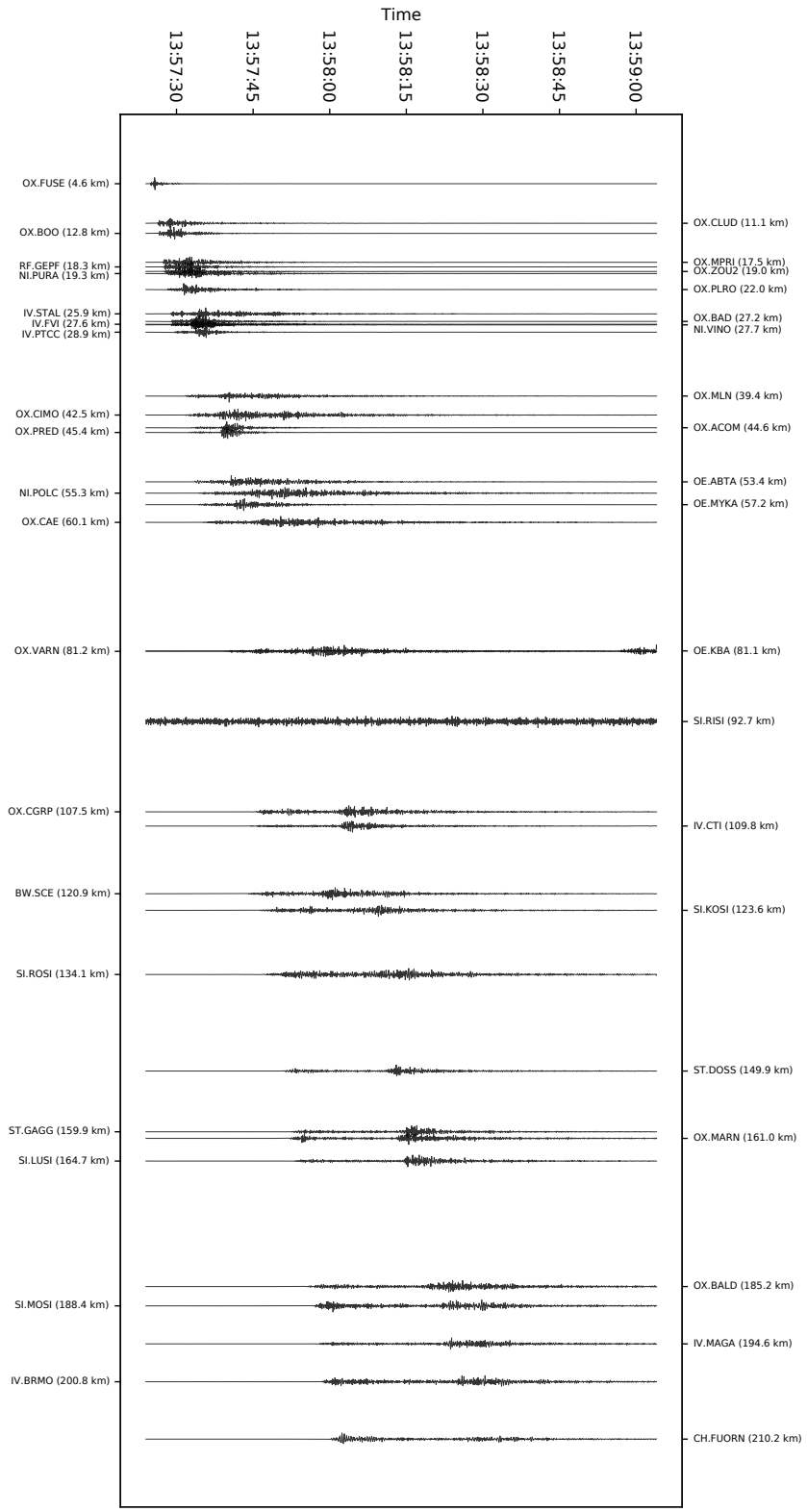

Figure A3. Vertical channel event waveforms for all available permanent AlpArray stations within the Swath-D area (see Section 2.1 for a description of the networks) for a relatively large earthquake of magnitude M_w 3.7 that took place near the village of Tolmezzo in Friuli, Italy on 14 June 2019 at 13:57:24 (UTC). Stations are sorted by distance from left to right. The waveform data is band-pass-filtered between $2 - 8$ Hz.

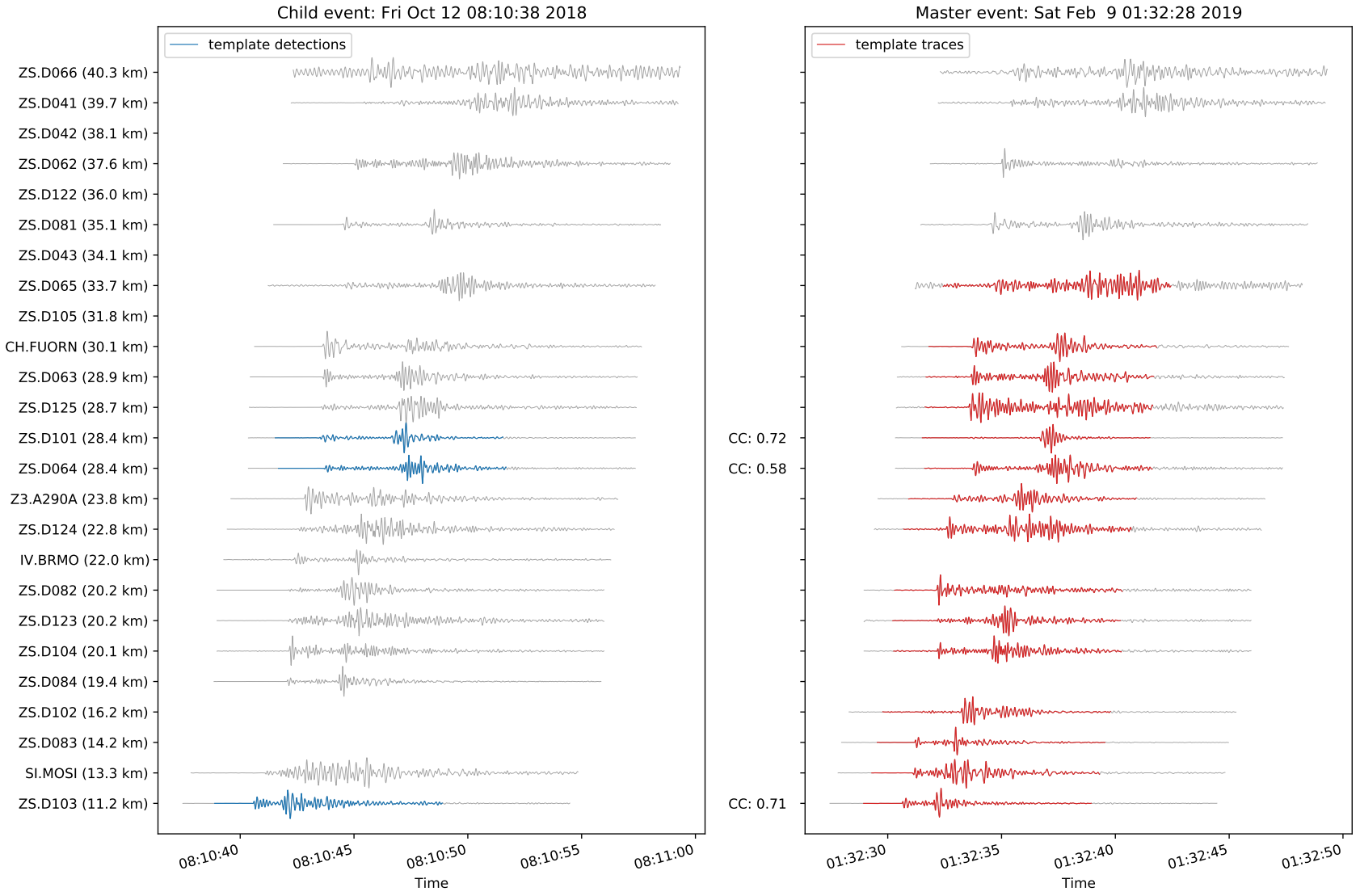

Figure A4. Example of an event detection by template matching. Note that although these events are co-located and similar in magnitude, the waveforms are quite different for many stations.

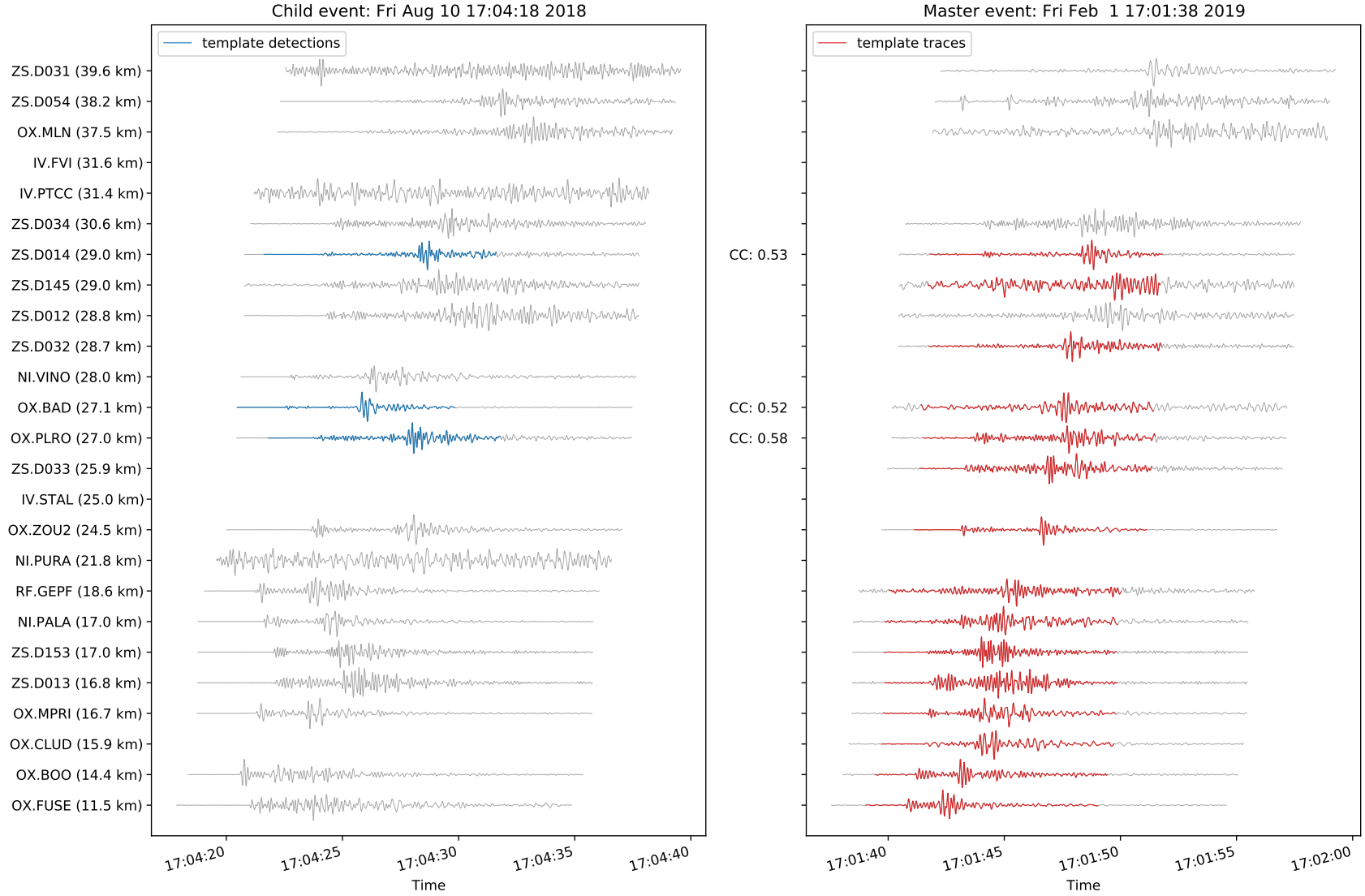

Figure A5. Example of an event that barely meets the template matching threshold. The difference in travel-times for the first stations indicate that these events are spatially separated. The closest stations have completely different waveforms. In the final event catalogue, the epicentral distance for these events is 5.91 km.

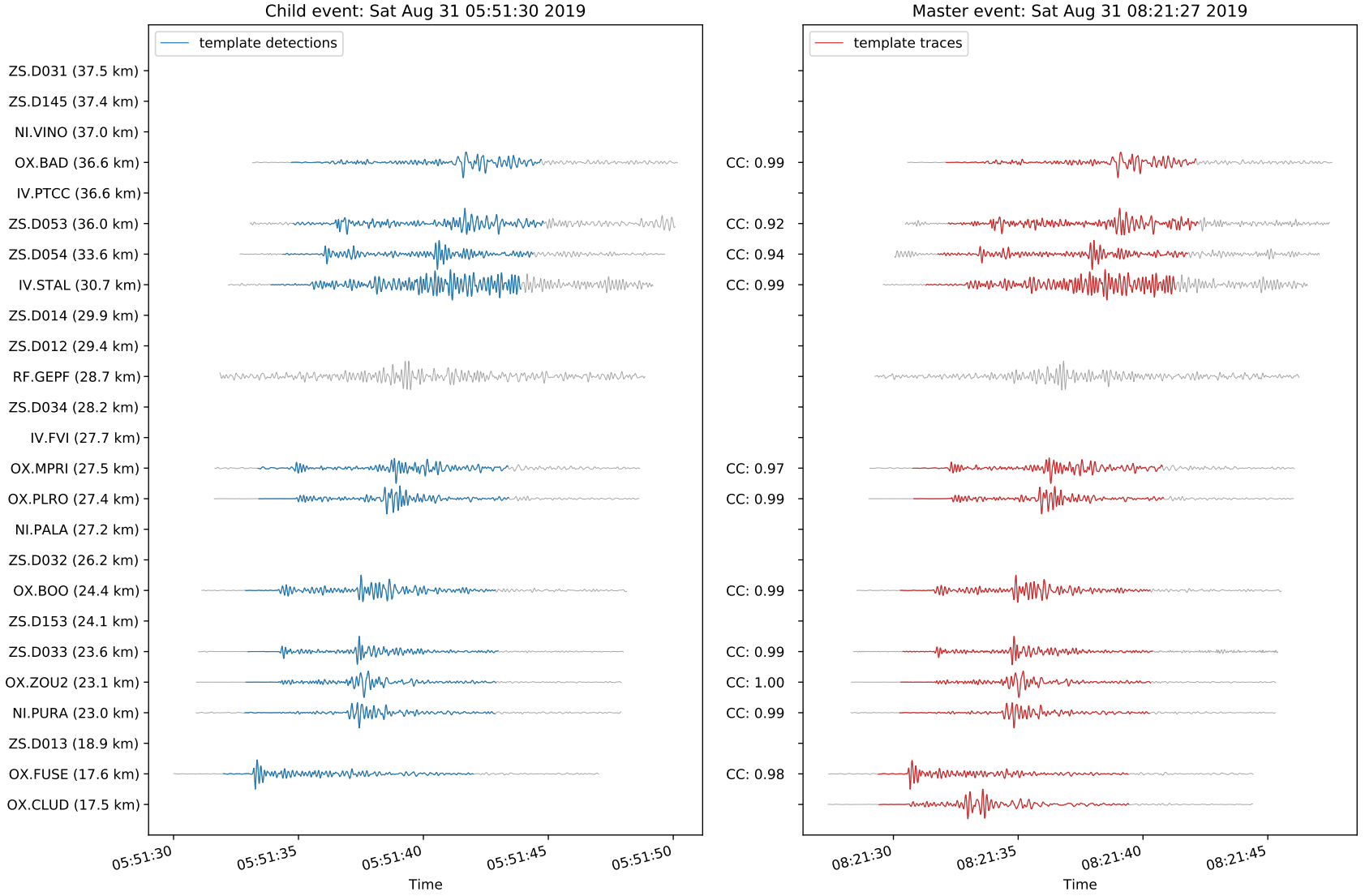

Figure A6. Example of an event detection by template matching with extremely similar waveforms for many different stations. These events are exactly co-located. The master event is of magnitude $0.2M_L$, the detected event is of magnitude $0.1M_L$.

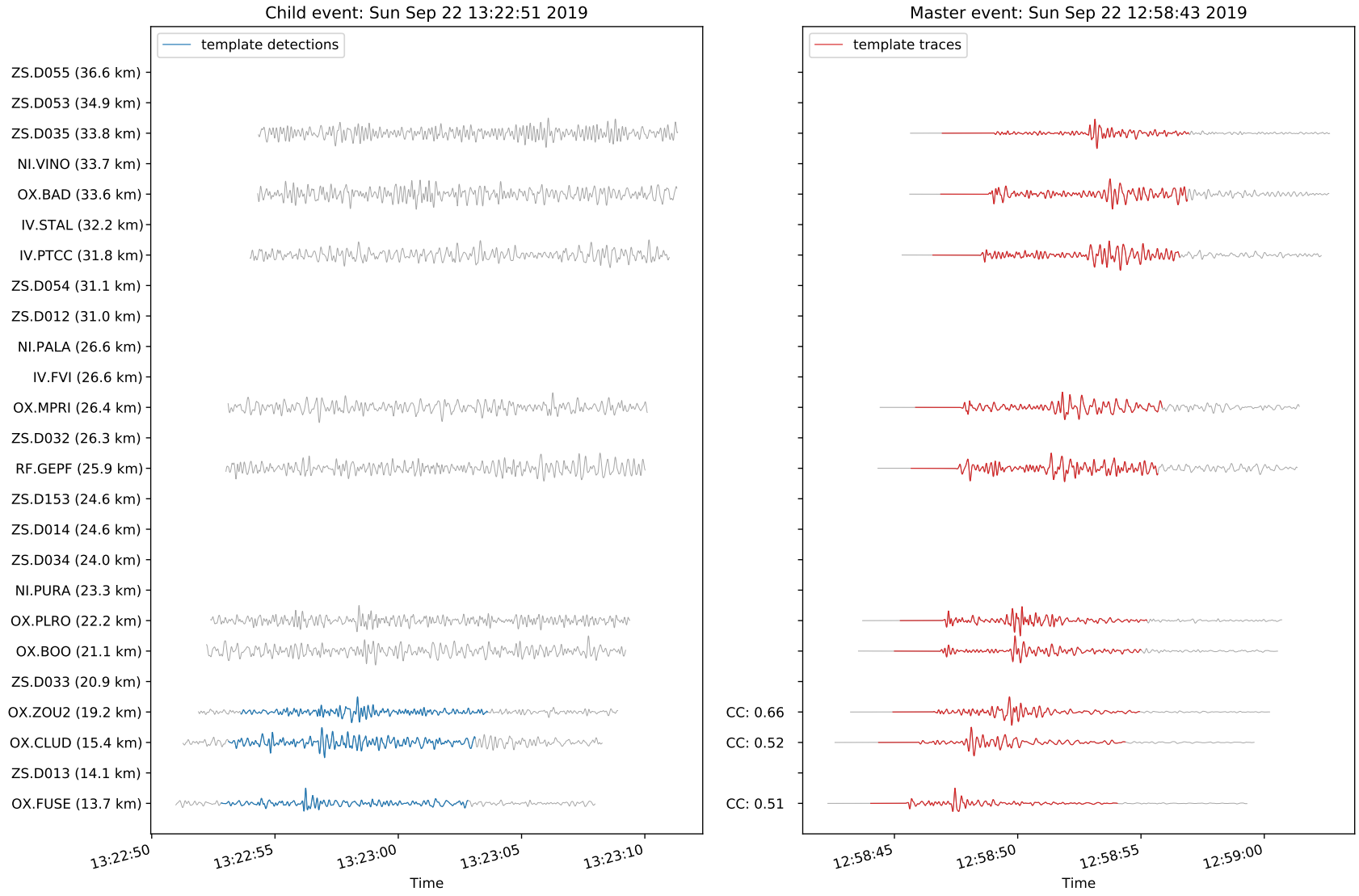

Figure A7. Example of an event detection with an extremely large magnitude difference. The master event is of magnitude $3.1M_L$ and the detected event is of magnitude $-0.9M_L$.

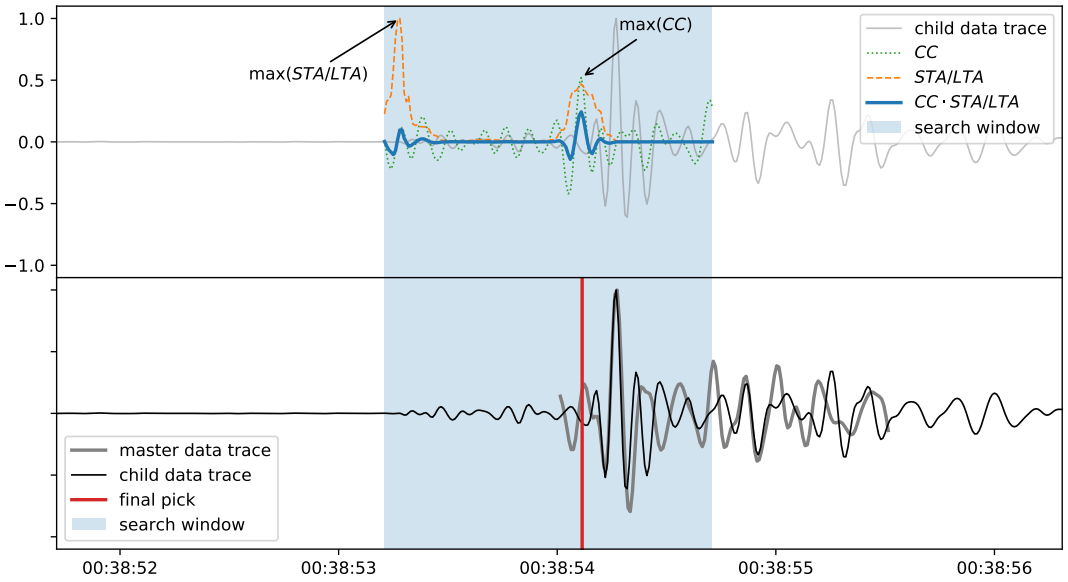

Figure A8. Example of the automated picking algorithm using a master pick as explained in Section 3.2.2. The final pick is based on the maximum of the product of the cross-correlation function, and an STA/LTA trigger. Note that the STA/LTA trigger catches on to the P-phase at the edge of the search window, but the cross-correlation guides the trigger to the correct place.

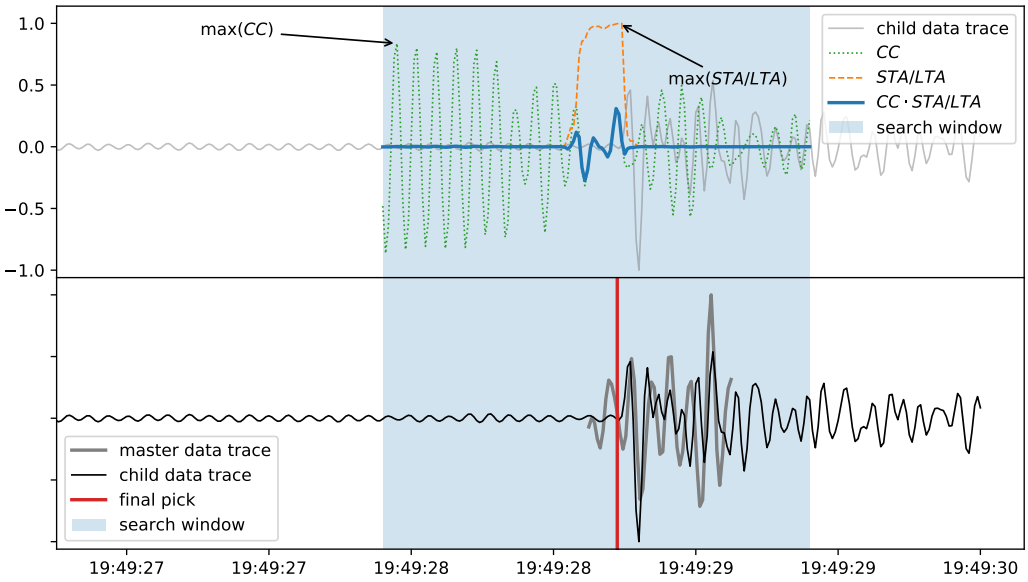

Figure A9. Example of the automated picking algorithm using a master pick as explained in Section 3.2.2. The final pick is based on the maximum of the product of the cross-correlation function, and an STA/LTA trigger. Note that the cross-correlation function is extremely disturbed due to an interfering noise signal. The STA/LTA trigger helps guide the picker to the phase-onset.

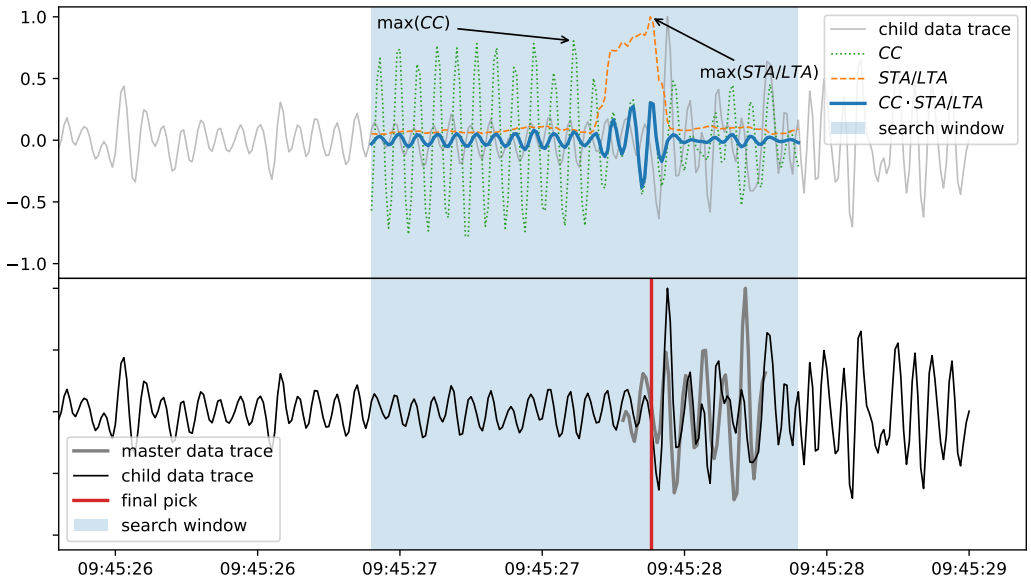

Figure A10. Example of the automated picking algorithm using a master pick as explained in Section 3.2.2. The final pick is based on the maximum of the product of the cross-correlation function, and an STA/LTA trigger. This example shows the successful application of the method to a very noisy data trace.

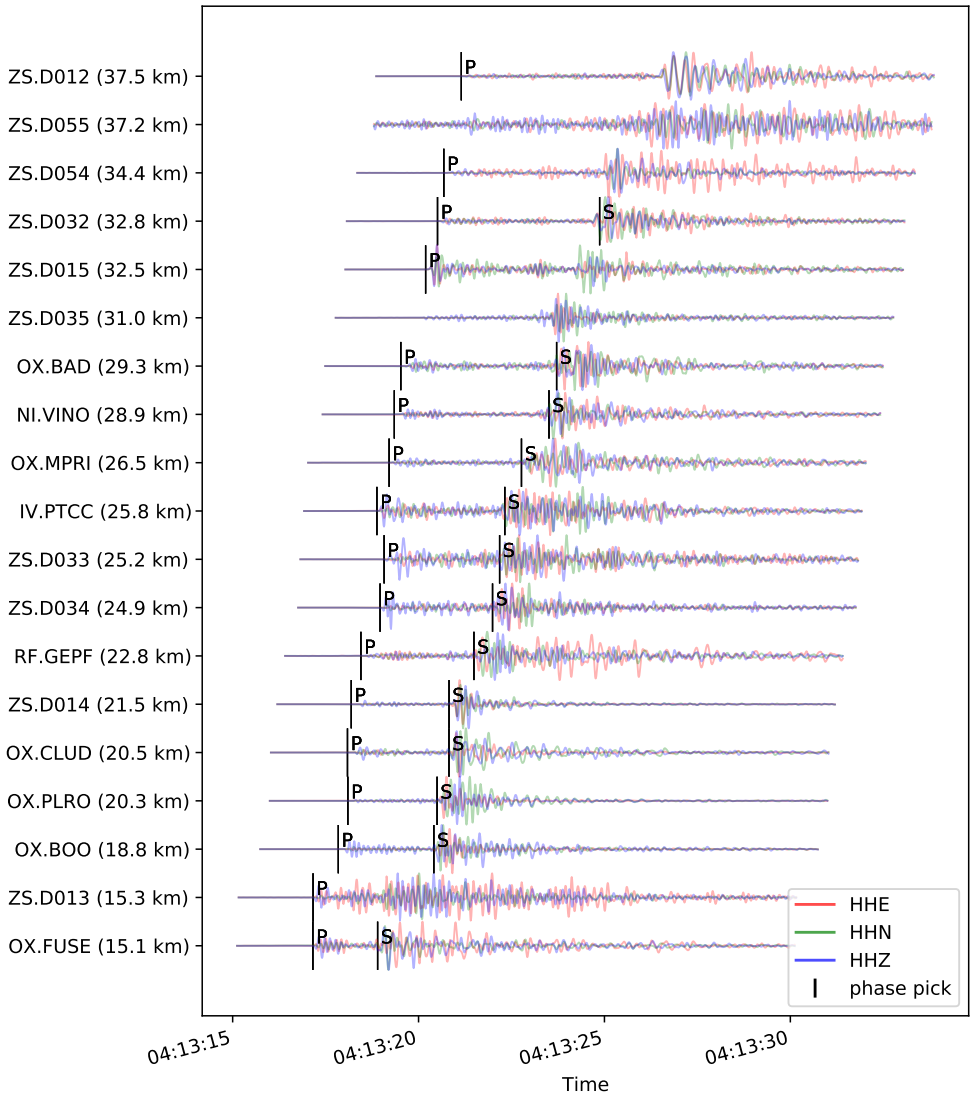

Figure A11. Waveform data for a relatively large earthquake detected in the Friuli region on 5 June 2018 at 04:13:14 (UTC) with a magnitude of 1.3 M_L (2.4 M_w). Stations are sorted by the hypocentral distance.

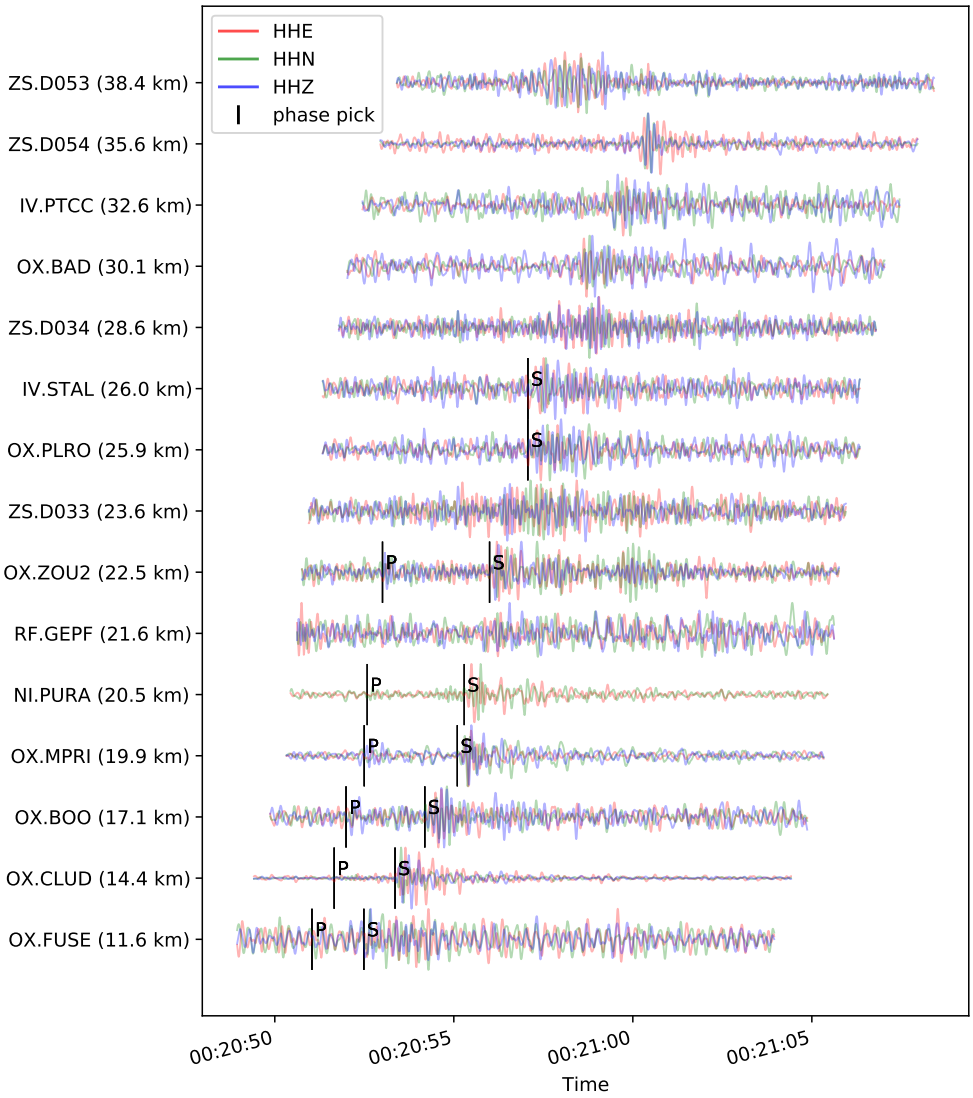

Figure A12. Waveform data for a small earthquake detected in the Friuli region on 4 November at 00:20:49 (UTC) with a magnitude of -1.1 M_L (0.8 M_w). Stations are sorted by the hypocentral distance.

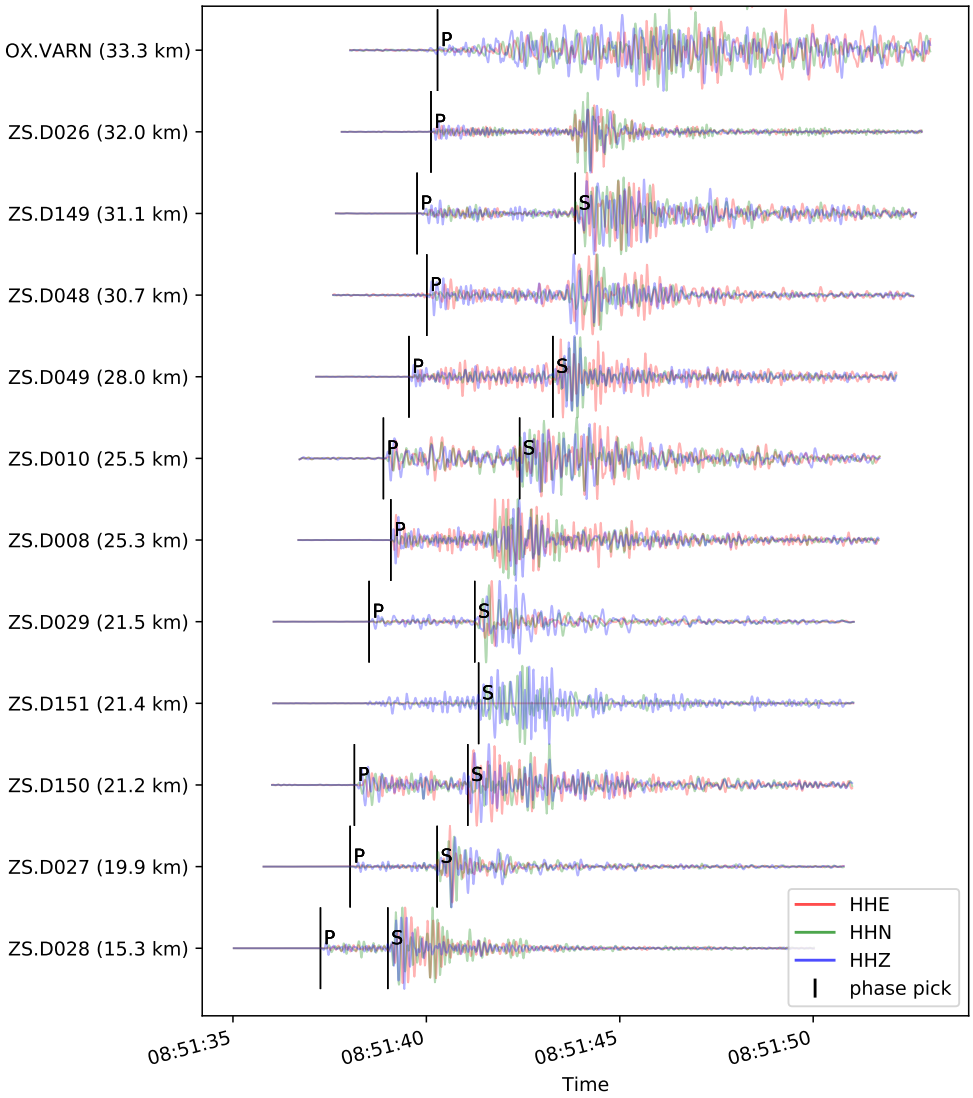

Figure A13. Waveform data for a relatively large earthquake detected in the Dolomite indenter region on 2 August 2018 at 08:51:34 (UTC) with a magnitude of 1.1 M_L (2.2 M_w). Stations are sorted by the hypocentral distance.

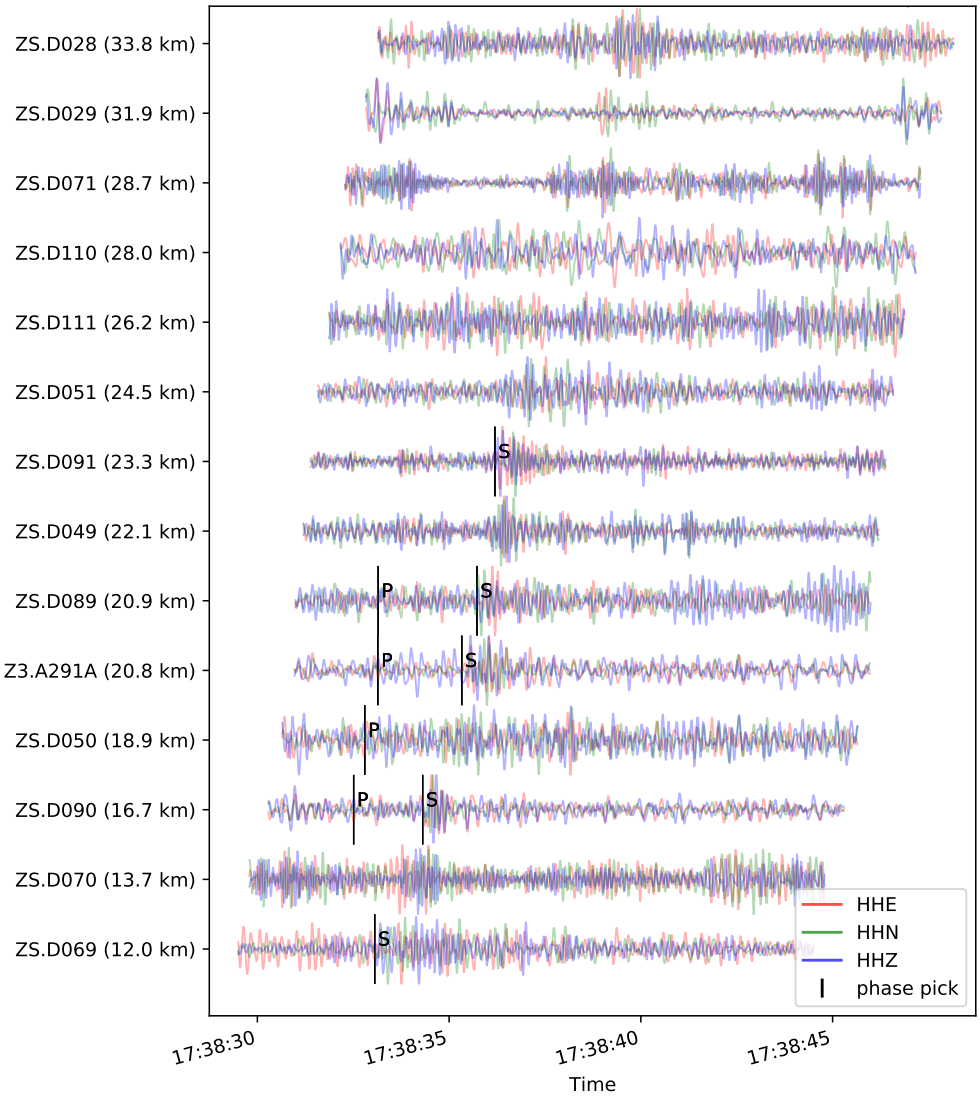

Figure A14. Waveform data for a small earthquake detected in the Dolomite indenter region on 2 April 2019 at 17:38:29 (UTC) with a magnitude of -1.1 M_L (0.8 M_w). Stations are sorted by the hypocentral distance.

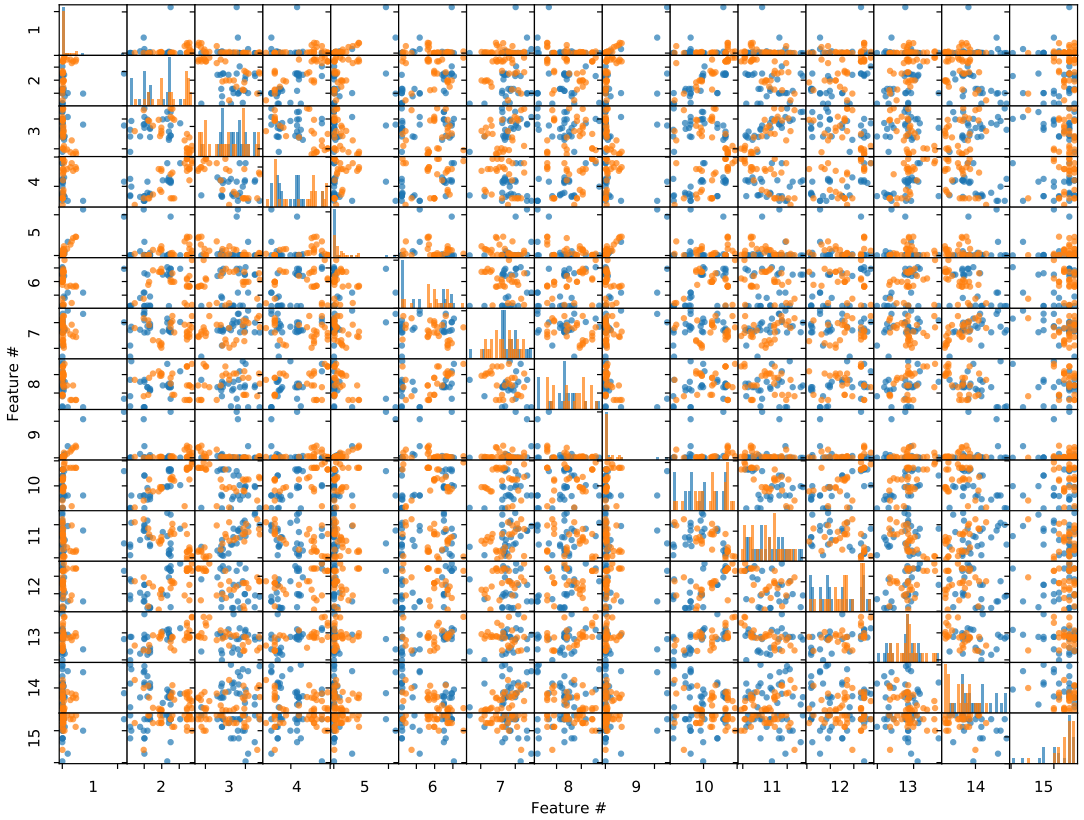

Figure A15. Scatter matrix of a selection of waveform attributes for dataset 2 as described in Section 4.1. On the off-diagonal subfigures, the row attribute i is plotted against the column attribute j, the diagonal subfigures show a histogram of the distribution for attribute i. The attribute numbers are explained in Table 4.1. Tectonic earthquakes are shown in blue, quarry blasts are shown in orange. The reduced feature space (PCA) of this dataset is shown in Figure 4.2.

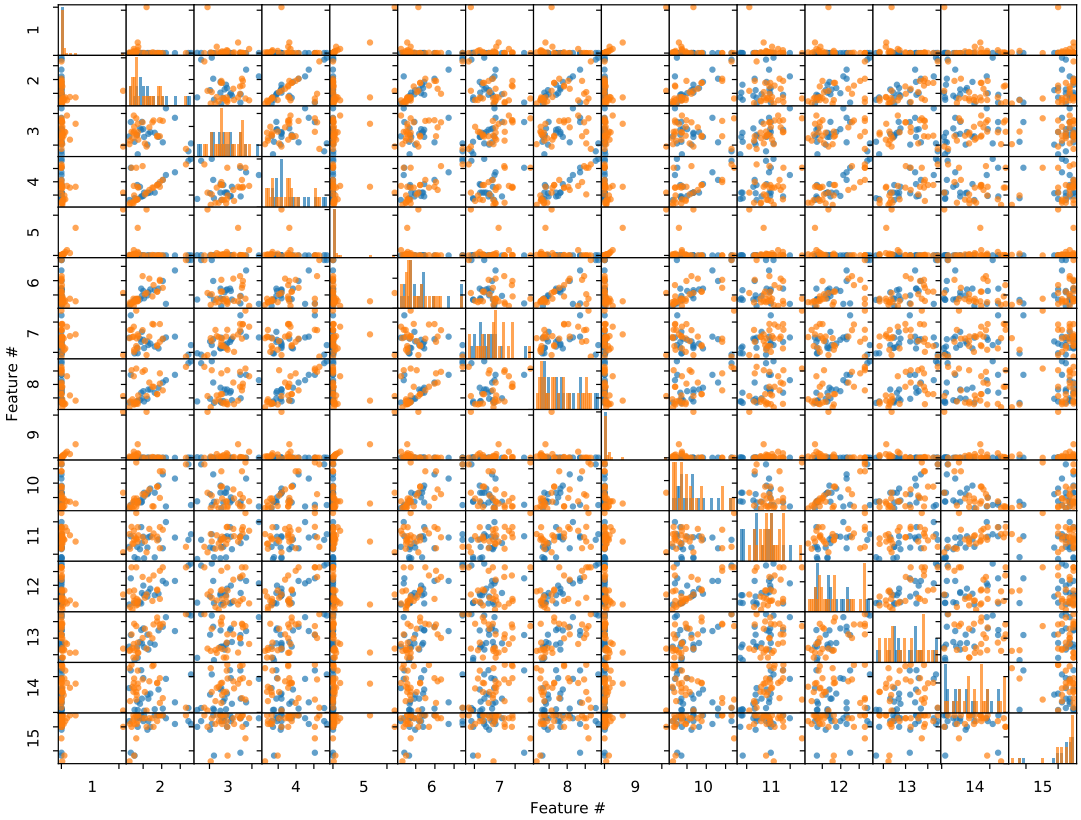

Figure A16. Scatter matrix of a selection of waveform attributes for dataset 3 as described in Section 4.1. On the off-diagonal subfigures, the row attribute i is plotted against the column attribute j, the diagonal subfigures show a histogram of the distribution for attribute i. The attribute numbers are explained in Table 4.1. Tectonic earthquakes are shown in blue, quarry blasts are shown in orange. The reduced feature space (PCA) of this dataset is shown in Figure 4.2.

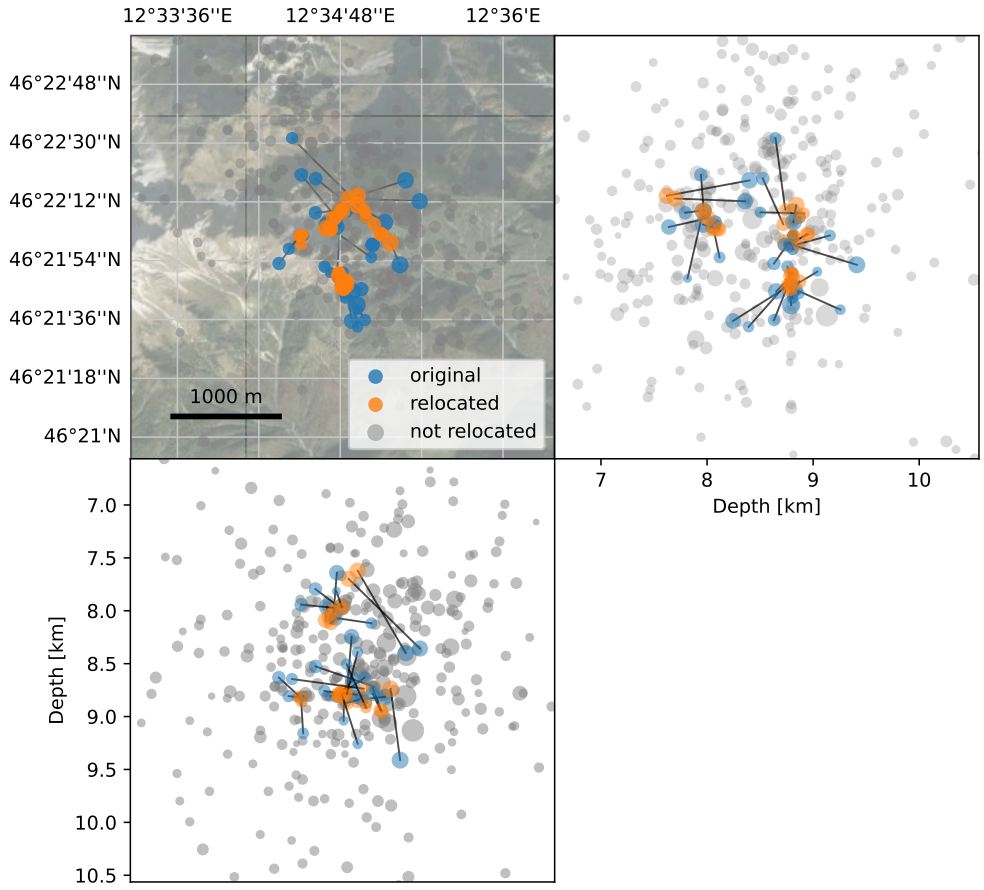

Figure A17. Result of the S-P differential travel time inversion of event cluster B (25 February 2018) in the Friuli region. The original event location are indicated by blue circles, the orange circles represent the relocated events. Events from the original cluster that could not be relocated are displayed as grey circles.

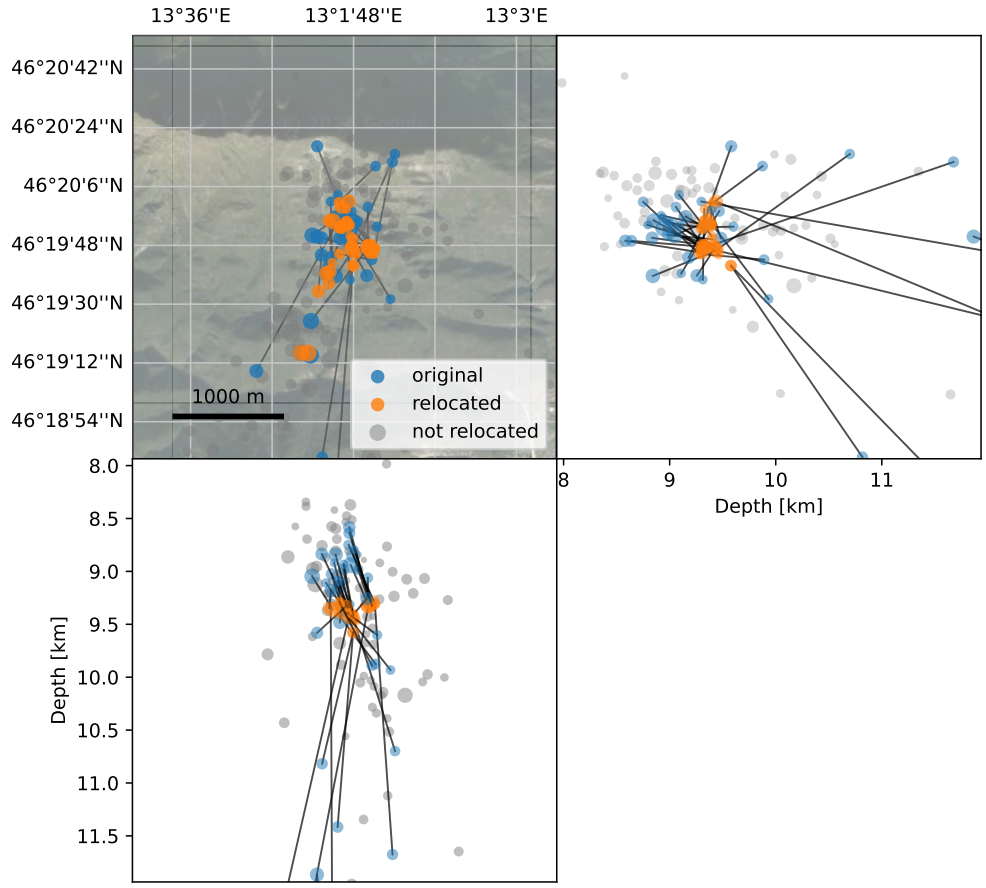

Figure A18. Result of the S-P differential travel time inversion of event cluster D (11 August 2018) in the Friuli region. The original event location are indicated by blue circles, the orange circles represent the relocated events. Events from the original cluster that could not be relocated are displayed as grey circles.

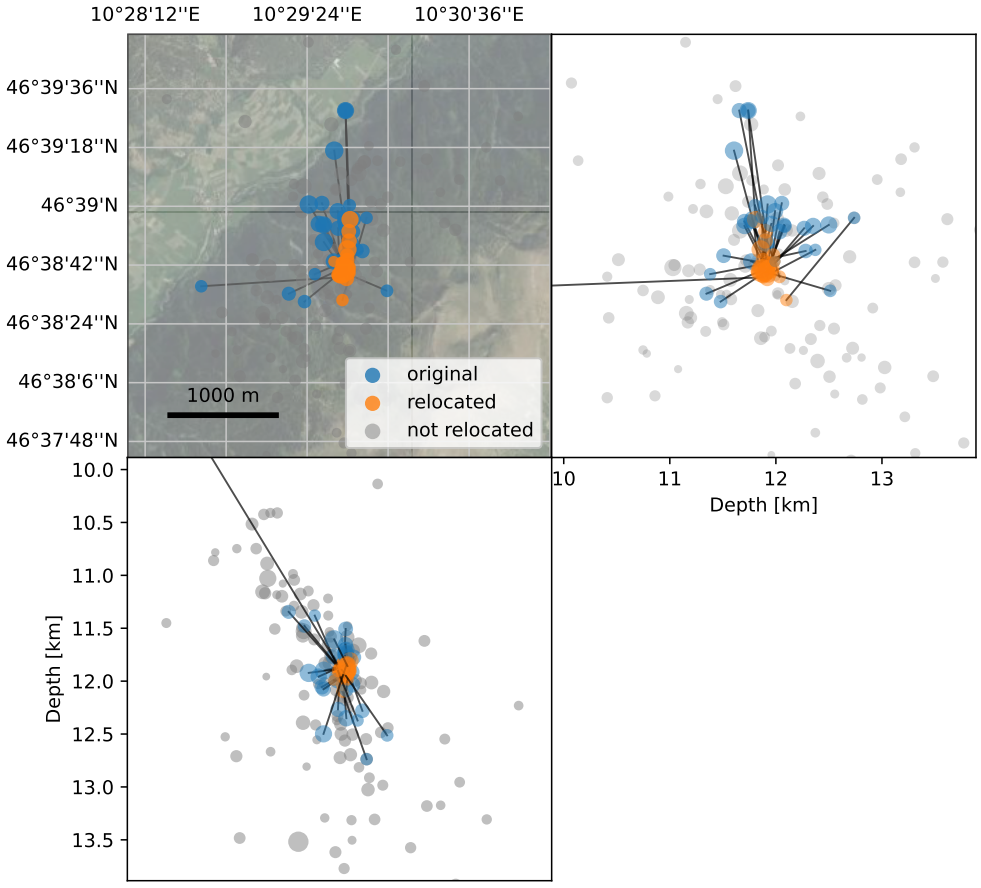

Figure A19. Result of the S-P differential travel time inversion of event cluster C (25 April 2018) in the Engadine and Ortler Alps region. The original event location are indicated by blue circles, the orange circles represent the relocated events. Events from the original cluster that could not be relocated are displayed as grey circles.

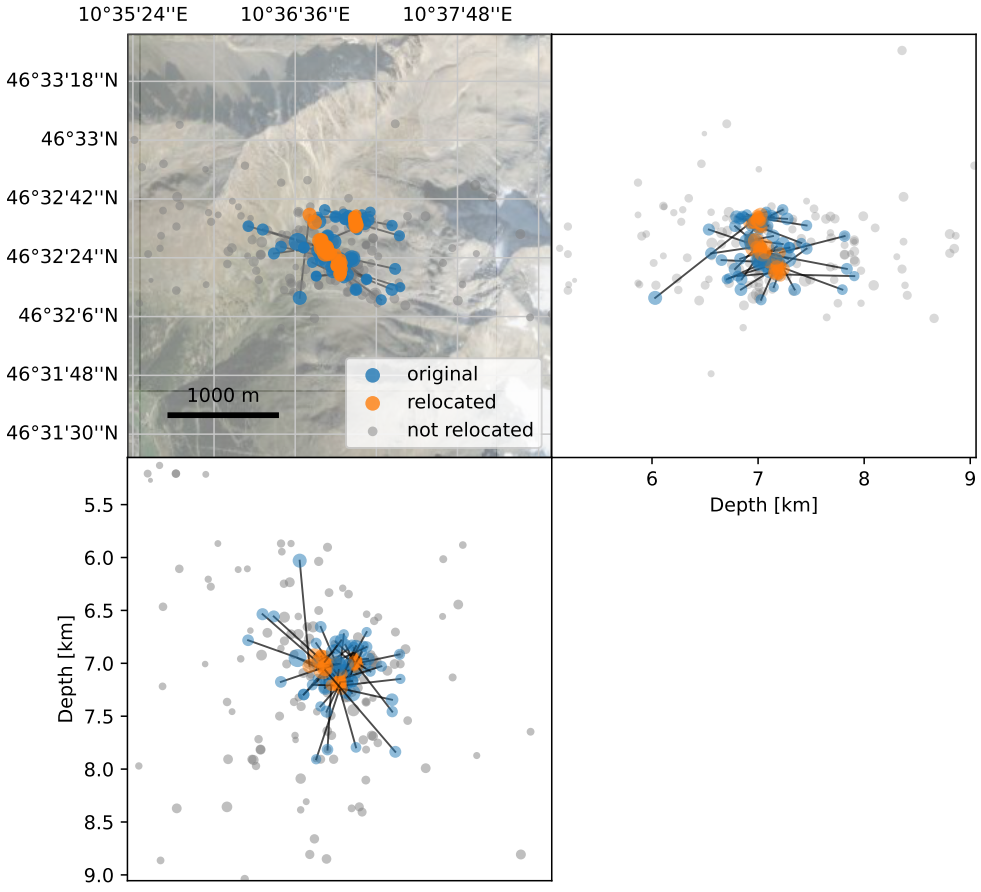

Figure A20. Result of the S-P differential travel time inversion of event cluster F (9 February 2019) in the Engadine and Ortler Alps region. The original event location are indicated by blue circles, the orange circles represent the relocated events. Events from the original cluster that could not be relocated are displayed as grey circles.

Appendix B: B Fitting the GR to the FMD

In this section I discuss the methods used for fitting the Gutenberg-Richter relation (GR) (Gutenberg and Richter, 1944) (Equation 5.2) to the frequency magnitude distribution (FMD). The most simple way to fit a linear trend to data is by using the least-squares method. This method is applied to fit the GR relation to the FMD by taking the logarithm of the frequency. However, the GR law in fact describes a power law and many authors have described the pitfalls of using the least-squares method to fit a power law (e.g. Goldstein et al., 2004; Clauset et al., 2009; Geffers et al., 2022). Aki (1965) proposed the maximum likelihood estimate for the b-value in the GR relations, which is often cited to be less biased compared to the least-squares method. However, after testing the maximum likelihood estimate using the code published by Goebel et al. (2017), I found the b-values not representative for my dataset. To demonstrate this, I show the results for the maximum likelihood estimate of the b-values for the five seismo-tectonic domains in Figure B1.

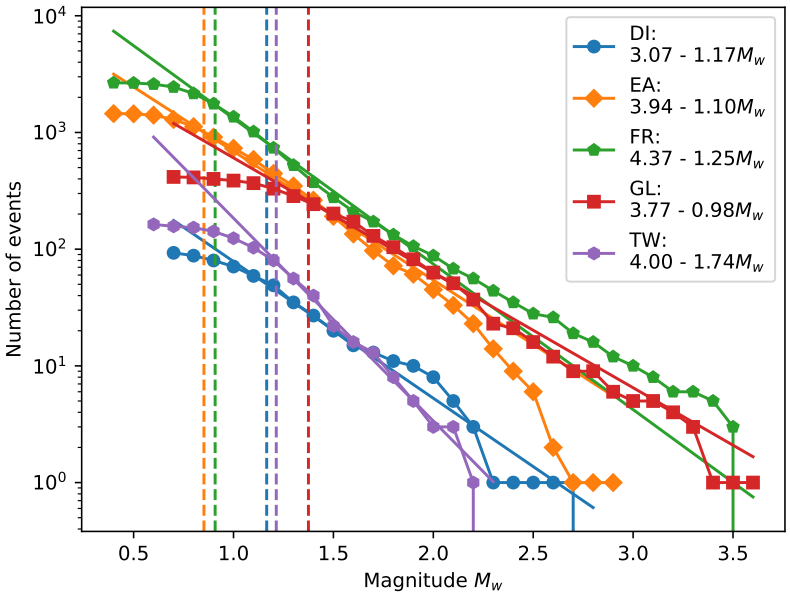

Figure B1. Magnitude frequency distributions for each of the seismo-tectonic domains as in Figure 6.8. Magnitudes are in the moment magnitude scale (M_w), estimated using the scaling relation (Equation 5.3) by Munafò et al. (2016). The GR fit is based on the maximum likelihood estimated using the code published by Goebel et al. (2017).

Compared to the least-squares fit of the GR relation as shown in Figure 6.8, much more weight is attributed to the lower end of the FMD. In general, this is

justified because the lower end of the FMD contains much more data than the upper end of the magnitude spectrum. However, this does make the estimate very strongly dependent on the completeness magnitude M_c. In the case of this dataset, the lower end of the FMD contains extremely small magnitudes. As also discussed in Section 5.2, I suspect that the lower end of the FMD is slightly biased because the earthquake signals approach the level of the background noise. As the local magnitude is calculated directly from the amplitude of the seismograph, interference with the background noise may lead to an overestimation of the local magnitude for very small earthquakes. I therefore prefer to apply more weight to the central part of the FMD, where the magnitudes are more reliable. Figure B1 shows the unsatisfactory results of the maximum likelihood method. The effect is especially clear in the Friuli region (FR) and the Engadine and Ortler Alps (EA), where the maximum likelihood fit does not reflect the behaviour of the $M_w > 1.5$ seismicity at all. I therefore decided to use the least-squares approach. I also emphasise that I only use the GR relation to compare the different parts of the study area by analysing the differences among the b-values.

Bibliography

Abe, S. and N. Suzuki (2012). "Dynamical evolution of the community structure of complex earthquake network". In: *EPL (Europhysics Letters)* 99.3, p. 39001. ISSN: 1286-4854. DOI: 10.1209/0295-5075/99/39001.

Aki, K. (1965). "Maximum likelihood estimate of b in the formula log N = a - bM and its confidence limits". In: *Bull. Earthquake Res. Inst., Tokyo Univ.* 43, pp. 237–239.

Albert, R. and A.-L. Barabási (2002). "Statistical mechanics of complex networks". In: *Reviews of Modern Physics* 74.1, pp. 47–97. ISSN: 1539-0756. DOI: 10.1103/revmodphys.74.47.

AlpArray Working Group (2014). *AlpArray Seismic Network: Eastern Alpine Seismic Investigation (EASI) – AlpArray Complimentary Experiment*. Swiss Seismological Service (SED) at ETH Zurich. DOI: 10.12686/alparray/xt_2014.

Amitrano, D. (2003). "Brittle-ductile transition and associated seismicity: Experimental and numerical studies and relationship with the b value". In: *Journal of Geophysical Research: Solid Earth* 108.B1. ISSN: 0148-0227. DOI: 10.1029/2001jb000680.

Anselmi, M., A. Govoni, P. De Gori, and C. Chiarabba (2011). "Seismicity and velocity structures along the south-Alpine thrust front of the Venetian Alps (NE-Italy)". In: *Tectonophysics* 513.1, pp. 37–48. DOI: 10.1016/j.tecto.2011.09.023.

Aoudia, A., A. Saraó, B. Bukchin, and P. Suhadolc (2000). "The 1976 Friuli (NE Italy) thrust faulting earthquake: A reappraisal 23 years later". In: *Geophysical Research Letters* 27.4, pp. 573–576. DOI: 10.1029/1999GL011071.

Arrowsmith, S. J. and L. Eisner (2006). "A technique for identifying microseismic multiplets and application to the Valhall field, North Sea". In: *GEOPHYSICS* 71.2, pp. V31–V40. ISSN: 1942-2156. DOI: 10.1190/1.2187804.

Bakun, W. H. and W. B. Joyner (1984). "The ML scale in central California". In: *Bulletin of the Seismological Society of America* 74.5, pp. 1827–1843. DOI: 10.1785/BSSA0740051827.

Beaucé, E., W. B. Frank, A. Paul, M. Campillo, and R. D. van der Hilst (2019). "Systematic Detection of Clustered Seismicity Beneath the Southwestern Alps". In: *Journal of Geophysical Research: Solid Earth* 124.11, pp. 11531–11548. DOI: 10.1029/2019JB018110.

Bethmann, F., N. Deichmann, and P. M. Mai (2011). "Scaling Relations of Local Magnitude versus Moment Magnitude for Sequences of Similar Earthquakes in Switzerland". In: *Bulletin of the Seismological Society of America* 101.2, pp. 515–534. ISSN: 0037-1106. DOI: 10.1785/0120100179. eprint: https://pubs.geoscienceworld.org/ssa/bssa/article-pdf/101/2/515/2652314/515.pdf.

Bethoux, N., G. Ouillon, and M. Nicolas (1998). "The instrumental seismicity of the western Alps: spatio—temporal patterns analysed with the wavelet transform". In: *Geophysical Journal International* 135.1, pp. 177–194. DOI: 10.1046/j.1365-246X.1998.00631.x.

Beyreuther, M., R. Barsch, L. Krischer, T. Megies, Y. Behr, and J. Wassermann (2010). "ObsPy: A Python Toolbox for Seismology". In: *Seismological Research Letters* 81.3, pp. 530–533. DOI: 10.1785/gssrl.81.3.530.

Bianchi, I., E. Ruigrok, A. Obermann, and E. Kissling (2021). "Moho topography beneath the European Eastern Alps by global-phase seismic interferometry". In: *Solid Earth* 12.5, pp. 1185–1196. DOI: 10.5194/se-12-1185-2021.

Bigi, G., A. Castellarin, M. Coli, G. Dal Piaz, R. Sartori, and P. Scandone (1990). *Structural Model of Italy, sheet 1, 1:500,000*. Consiglio Naz. Ricerche, Progetto Finalizzato Geodinamica, SELCA Firenze.

Bleibinhaus, F. and H. Gebrande (2006). "Crustal structure of the Eastern Alps along the TRANSALP profile from wide-angle seismic tomography". In: *Tectonophysics* 414.1, pp. 51–69. DOI: 10.1016/j.tecto.2005.10.028.

Blondel, V. D., J.-L. Guillaume, R. Lambiotte, and E. Lefebvre (2008). "Fast unfolding of communities in large networks". In: *Journal of Statistical Mechanics: Theory and Experiment* 2008.10, P10008. DOI: 10.1088/1742-5468/2008/10/p10008.

Bousquet, R., S. M. Schmid, G. Zeilinger, R. Oberhänsli, C. Rosenberg, G. Molli, C. Robert, M. Wiederkehr, and P. Rossi (2012). "Tectonic Framework of the Alps (1: 1,000,000)". In: *CCGM-CGMW Commission de la Carte Géologique du Monde*.

Bragato, P. L., P. Comelli, A. Saraò, D. Zuliani, L. Moratto, V. Poggi, G. Rossi, C. Scaini, M. Sugan, C. Barnaba, P. Bernardi, M. Bertoni, G. Bressan, A. Compagno, E. Del Negro, P. Di Bartolomeo, P. Fabris, M. Garbin, M. Grossi, A. Magrin, E. Magrin, D. Pesaresi, B. Petrovic, M. P. P. Linares, M. Romanelli, A. Snidarcig, L. Tunini, S. Urban, E. Venturini, and S. Parolai (2021). "The OGS–Northeastern Italy Seismic and Deformation Network: Current Status and Outlook". In: *Seismological Research Letters*. DOI: 10.1785/0220200372.

Bragato, P. L. and A. Tento (2005). "Local magnitude in northeastern Italy". In: *Bulletin of the Seismological Society of America* 95.2, pp. 579–591. DOI: 10.1785/0120040100.

Bressan, G., G. F. Gentile, R. Tondi, R. D. Franco, and S. Urban (2012). "Sequential Integrated Inversion of tomographic images and gravity data: an application to the Friuli area (north-eastern Italy)." In: *Bollettino di Geofisica Teorica ed Applicata* 53.2. DOI: 10.4430/bgta0059.

Brückl, E., F. Bleibinhaus, A. Gosar, M. Grad, A. Guterch, P. Hrubcová, G. R. Keller, M. Majdański, F. Šumanovac, T. Tiira, J. Yliniemi, E. Hegedűs, and H. Thybo (2007). "Crustal structure due to collisional and escape tectonics in the Eastern Alps region based on profiles Alp01 and Alp02 from the ALP 2002 seismic experiment". In: *Journal of Geophysical Research: Solid Earth* 112.B6. DOI: 10.1029/2006JB004687.

Caporali, A., F. Neubauer, L. Ostini, G. Stangl, and D. Zuliani (2013). "Modeling surface GPS velocities in the Southern and Eastern Alps by finite dislocations at crustal depths". In: *Tectonophysics* 590, pp. 136–150. DOI: 10.1016/j.tecto.2013.01.016.

Caracciolo, C. H., D. Slejko, R. Camassi, and V. Castelli (2021). "The eastern Alps earthquake of 25 January 1348: new insights from old sources". In: *Bulletin of Geophysics and Oceanography*. DOI: 10.4430/bgo00364.

Castellarin, A., R. Nicolich, R. Fantoni, L. Cantelli, M. Sella, and L. Selli (2006). "Structure of the lithosphere beneath the Eastern Alps (southern sector of the TRANSALP transect)". In: *Tectonophysics* 414.1, pp. 259–282. DOI: 10.1016/j.tecto.2005.10.013.

Cheloni, D., N. D'Agostino, and G. Selvaggi (2014). "Interseismic coupling, seismic potential, and earthquake recurrence on the southern front of the Eastern Alps (NE Italy)". In: *Journal of Geophysical Research: Solid Earth* 119.5, pp. 4448–4468. DOI: 10.1002/2014JB010954.

Chiarabba, C., L. Jovane, and R. DiStefano (2005). "A new view of Italian seismicity using 20 years of instrumental recordings". In: *Tectonophysics* 395.3, pp. 251–268. DOI: 10.1016/j.tecto.2004.09.013.

Clauset, A., C. R. Shalizi, and M. E. Newman (2009). "Power-law distributions in empirical data". In: *SIAM review* 51.4, pp. 661–703.

Deichmann, N. (2006). "Local Magnitude, a Moment Revisited". In: *Bulletin of the Seismological Society of America* 96.4A, pp. 1267–1277. ISSN: 0037-1106. DOI: 10.1785/0120050115.

Department Of Earth And Environmental Sciences, Geophysical Observatory, University Of München (2001). *BayernNetz*. DOI: 10.7914/SN/BW.

Dewey, J. F., W. C. Pitman III, W. B. F. Ryan, and J. Bonnin (1973). "Plate tectonics and the evolution of the Alpine system". In: *Geological society of America bulletin* 84.10, pp. 3137–3180. DOI: 10.1130/0016-7606(1973)84<3137:PTATEO>2.0.CO;2.

Diehl, T., S. Husen, E. Kissling, and N. Deichmann (2009). "High-resolution 3-D P-wave model of the Alpine crust". In: *Geophysical Journal International* 179.2, pp. 1133–1147. DOI: 10.1111/j.1365-246X.2009.04331.x.

Downey, A. (2018). *Think complexity: complexity science and computational modeling*. " O'Reilly Media, Inc."

Earle, P. S. and P. M. Shearer (1994). "Characterization of global seismograms using an automatic-picking algorithm". In: *Bulletin of the Seismological Society of America* 84.2, pp. 366–376. DOI: 10.1785/BSSA0840020366.

Folesky, J., C. N. Pennington, J. Kummerow, and L. J. Hofman (2024). "A Comprehensive Stress Drop Map From Trench to Depth in the Northern Chilean Subduction Zone". In: *Journal of Geophysical Research: Solid Earth* 129.1. ISSN: 2169-9356. DOI: 10.1029/2023jb027549.

Froitzheim, N., S. M. Schmid, and M. Frey (1996). "Mesozoic paleogeography and the timing of eclogite-facies metamorphism in the Alps: A working hypothesis". In: *Eclogae Geologicae Helvetiae* 89.1, pp. 81–110. DOI: 10.5169/seals-167895.

Geffers, G.-M., I. G. Main, and M. Naylor (2022). "Biases in estimating b-values from small earthquake catalogues: how high are high b-values?" In: *Geophysical Journal International* 229.3, pp. 1840–1855. ISSN: 1365-246X. DOI: 10.1093/gji/ggac028.

GFZ German Research Centre For Geosciences and Institut Des Sciences De L'Univers-Centre National De La Recherche CNRS-INSU (2006). *IPOC Seismic Network*. DOI: 10.14470/PK615318.

Gibbons, S. J. and F. Ringdal (2006). "The detection of low magnitude seismic events using array-based waveform correlation". In: *Geophysical Journal International* 165.1, pp. 149–166. DOI: 10.1111/j.1365-246X.2006.02865.x.

Goebel, T. H., G. Kwiatek, T. W. Becker, E. E. Brodsky, and G. Dresen (2017). "What allows seismic events to grow big?: Insights from b-value and fault roughness analysis in laboratory stick-slip experiments". In: *Geology* 45.9, pp. 815–818. ISSN: 0091-7613. DOI: 10.1130/g39147.1.

Goldstein, M. L., S. A. Morris, and G. G. Yen (2004). "Problems with fitting to the power-law distribution". In: *The European Physical Journal B* 41.2, 255â–258. ISSN: 1434-6036. DOI: 10.1140/epjb/e2004-00316-5.

Got, J.-L. and P. Okubo (2003). "New insights into Kilauea's volcano dynamics brought by large-scale relative relocation of microearthquakes". In: *Journal of Geophysical Research: Solid Earth* 108.B7. ISSN: 0148-0227. DOI: 10.1029/2002jb002060.

Grünthal, G. and R. Wahlström (2012). "The European-Mediterranean Earthquake Catalogue (EMEC) for the last millennium". In: *Journal of Seismology* 16.3, pp. 535–570. DOI: 10.1007/s10950-012-9302-y.

Gutenberg, B. and C. F. Richter (1944). "Frequency of earthquakes in California*". In: *Bulletin of the Seismological Society of America* 34.4, pp. 185–188. DOI: 10.1785/BSSA0340040185.

Hagberg, A. A., D. A. Schult, and P. J. Swart (2008). "Exploring Network Structure, Dynamics, and Function using NetworkX". In: *Proceedings of the 7th*

Python in Science Conference. Ed. by G. Varoquaux, T. Vaught, and J. Millman. Pasadena, CA USA, pp. 11–15.

Handy, M. R., J. Giese, S. M. Schmid, J. Pleuger, W. Spakman, K. Onuzi, and K. Ustaszewski (2019). "Coupled crust-mantle response to slab tearing, bending, and rollback along the Dinaride-Hellenide orogen". In: *Tectonics* 38.8, pp. 2803–2828. DOI: 10.1029/2019TC005524.

Handy, M. R., S. M. Schmid, R. Bousquet, E. Kissling, and D. Bernoulli (2010). "Reconciling plate-tectonic reconstructions of Alpine Tethys with the geological-geophysical record of spreading and subduction in the Alps". In: *Earth-Science Reviews* 102.3, pp. 121–158. ISSN: 0012-8252. DOI: 10.1016/j.earscirev.2010.06.002.

Handy, M. R., K. Ustaszewski, and E. Kissling (2015). "Reconstructing the Alps-Carpathians-Dinarides as a key to understanding switches in subduction polarity, slab gaps and surface motion". In: *International Journal of Earth Sciences* 104.1, pp. 1–26. DOI: 10.1007/s00531-014-1060-3.

Hanks, T. C. and H. Kanamori (1979). "A moment magnitude scale". In: *Journal of Geophysical Research: Solid Earth* 84.B5, pp. 2348–2350. ISSN: 0148-0227. DOI: 10.1029/jb084ib05p02348.

Harris Charles, R., J. K. K. Jarrod Millman, S. J. van der Walt, R. Gommers, P. Virtanen, D. Cournapeau, E. Wieser, J. Taylor, S. Berg, N. J. Smith, R. Kern, M. Picus, S. Hoyer, M. H. van Kerkwijk, M. Brett, A. Haldane, J. F. del Río, M. Wiebe, P. Peterson, P. Gérard-Marchant, K. Sheppard, T. Reddy, W. Weckesser, H. Abbasi, C. Gohlke, and T. E. Oliphant (2020). "Array programming with NumPy". In: *Nature* 585.7825, pp. 357–362. DOI: 10.1038/s41586-020-2649-2.

Heimann, S., M. Kriegerowski, M. Isken, S. Cesca, S. Daout, F. Grigoli, C. Juretzek, T. Megies, N. Nooshiri, A. Steinberg, H. Sudhaus, H. Vasyura-Bathke, T. Willey, and T. Dahm (2017). *Pyrocko - An open-source seismology toolbox and library*. Version 2018.1.29. DOI: 10.5880/GFZ.2.1.2017.001.

Heit, B., L. Cristiano, C. Haberland, F. Tilmann, D. Pesaresi, Y. Jia, H. Hausmann, S. Hemmleb, M. Haxter, T. Zieke, K.-H. Jaeckl, A. Schloemer, and M. Weber (2021). "The SWATH-D Seismological Network in the Eastern Alps". In: *Seismological Research Letters*. DOI: 10.1785/0220200377.

Hetényi, G., I. Molinari, J. C. Götz Bokelmann, I. Bondár, W. C. Crawford, J.-X. Dessa, C. Doubre, W. Friederich, F. Fuchs, D. Giardini, Z. Gráczer, M. R. Handy, M. Herak, Y. Jia, E. Kissling, H. Kopp, M. Korn, L. Margheriti, T. Meier, M. Mucciarelli, A. Paul, D. Pesaresi, C. Piromallo, T. Plenefisch, J. Plomerová, J. Ritter, G. Rümpker, V. Šipka, D. Spallarossa, C. Thomas, F. Tilmann, J. Wassermann, M. Weber, Z. Wéber, V. Wesztergom, and M. Živčić (2018). "The AlpArray Seismic Network: A Large-Scale European Experiment to Image the Alpine Orogen." In: *Surv Geophys* 39.5, pp. 1009–1033. DOI: 10.1007/s10712-018-9472-4.

Hetényi, G., J. Plomerová, I. Bianchi, H. Kampfová Exnerová, G. Bokelmann, M. R. Handy, and V. Babuška (2018). "From mountain summits to roots:

Crustal structure of the Eastern Alps and Bohemian Massif along longitude 13.3 °E". In: *Tectonophysics* 744, pp. 239–255. DOI: 10.1016/j.tecto.2018.07.001.

Hirata, T. (1989). "A correlation between the b value and the fractal dimension of earthquakes". In: *Journal of Geophysical Research: Solid Earth* 94.B6, pp. 7507–7514. ISSN: 0148-0227. DOI: 10.1029/jb094ib06p07507.

Hofman, L. J., J. Kummerow, and S. Cesca (2023). "A new seismicity catalogue of the eastern Alps using the temporary Swath-D network". In: *Solid Earth* 14.10, pp. 1053–1066. ISSN: 1869-9529. DOI: 10.5194/se-14-1053-2023.

Hofman, L. J., J. Kummerow, S. Cesca, and the AlpArray-Swath-D Working Group (2023). *Seismicity catalogue for the Eastern Alps (Swath-D)*. DOI: 10.5880/FIDGEO.2023.024.

Hua, Y., D. Zhao, and Y. Xu (2017). "P wave anisotropic tomography of the Alps". In: *Journal of Geophysical Research: Solid Earth* 122.6, pp. 4509–4528. DOI: 10.1002/2016JB013831.

INGV Seismological Data Centre (2006). *Rete Sismica Nazionale (RSN)*. DOI: 10.13127/SD/X0FXNH7QFY.

Istituto Nazionale di Oceanografia e di Geofisica Sperimentale (OGS) (2016). *North-East Italy Seismic Network*. DOI: 10.7914/SN/OX.

Jozi Najafabadi, A., C. Haberland, T. Ryberg, V. F. Verwater, E. Le Breton, M. R. Handy, M. Weber, and the AlpArray and AlpArray SWATH-D working groups (2021). "Relocation of earthquakes in the southern and eastern Alps (Austria, Italy) recorded by the dense, temporary SWATH-D network using a Markov chain Monte Carlo inversion". In: *Solid Earth* 12.5, pp. 1087–1109. DOI: 10.5194/se-12-1087-2021.

Jozi Najafabadi, A., C. Haberland, M. R. Handy, E. Le Breton, and M. Weber (2023). "Seismic wave attenuation (1/Qp) in the crust underneath the Eastern and eastern Southern Alps (Europe): imaging effects of faults, fractures, and fluids". In: *Earth, Planets and Space* 75.1. ISSN: 1880-5981. DOI: 10.1186/s40623-023-01942-0.

Jozi Najafabadi, A., C. Haberland, E. Le Breton, M. R. Handy, V. F. Verwater, B. Heit, M. Weber, and the AlpArray and AlpArray SWATH-D Working Groups (2022). "Constraints on Crustal Structure in the Vicinity of the Adriatic Indenter (European Alps) From Vp and Vp/Vs Local Earthquake Tomography". In: *Journal of Geophysical Research: Solid Earth* 127.2, e2021JB023160. DOI: 10.1029/2021JB023160.

Kamada, T. and S. Kawai (1989). "An algorithm for drawing general undirected graphs". In: *Information Processing Letters* 31.1, pp. 7–15. ISSN: 0020-0190. DOI: 10.1016/0020-0190(89)90102-6.

Kästle, E. D., I. Molinari, L. Boschi, E. Kissling, and the AlpArray Working Group (2021). "Azimuthal anisotropy from eikonal tomography: example from ambient-noise measurements in the AlpArray network". In: *Geophysical Journal International* 229.1, pp. 151–170. DOI: 10.1093/gji/ggab453.

Kästle, E. D., C. Rosenberg, L. Boschi, N. Bellahsen, T. Meier, and A. El-Sharkawy (2020). "Slab break-offs in the Alpine subduction zone". In: *International Journal of Earth Sciences* 109.2, pp. 587–603. DOI: 10.1007/s00531-020-01821-z.

Kästle, E. D., A. El-Sharkawy, L. Boschi, T. Meier, C. Rosenberg, N. Bellahsen, L. Cristiano, and C. Weidle (2018). "Surface Wave Tomography of the Alps Using Ambient-Noise and Earthquake Phase Velocity Measurements". In: *Journal of Geophysical Research: Solid Earth* 123.2, pp. 1770–1792. DOI: 10.1002/2017JB014698.

Kissling, E. and F. Schlunegger (2018). "Rollback Orogeny Model for the Evolution of the Swiss Alps". In: *Tectonics* 37.4, pp. 1097–1115. DOI: 10.1002/2017TC004762.

Kristeková, M., J. Kristek, and P. Moczo (2009). "Time-frequency misfit and goodness-of-fit criteria for quantitative comparison of time signals". In: *Geophysical Journal International* 178.2, pp. 813–825. ISSN: 1365-246X. DOI: 10.1111/j.1365-246x.2009.04177.x.

Kummerow, J., R. Kind, O. Oncken, P. Giese, T. Ryberg, K. Wylegalla, and F. Scherbaum (2004). "A natural and controlled source seismic profile through the Eastern Alps: TRANSALP". In: *Earth and Planetary Science Letters* 225.1, pp. 115–129. DOI: 10.1016/j.epsl.2004.05.040.

Kuyuk, H. S., E. Yildirim, E. Dogan, and G. Horasan (2011). "An unsupervised learning algorithm: application to the discrimination of seismic events and quarry blasts in the vicinity of Istanbul". In: *Natural Hazards and Earth System Sciences* 11.1, pp. 93–100. ISSN: 1684-9981. DOI: 10.5194/nhess-11-93-2011.

Lippitsch, R., E. Kissling, and J. Ansorge (2003). "Upper mantle structure beneath the Alpine orogen from high-resolution teleseismic tomography". In: *Journal of Geophysical Research: Solid Earth* 108.B8. DOI: 10.1029/2002JB002016.

Lomax, A., J. Virieux, P. Volant, and C. Berge-Thierry (2000). "Probabilistic Earthquake Location in 3D and Layered Models". In: *Advances in Seismic Event Location*. Ed. by C. H. Thurber and N. Rabinowitz. Dordrecht: Springer Netherlands, pp. 101–134. ISBN: 978-94-015-9536-0. DOI: 10.1007/978-94-015-9536-0_5.

Lu, Y., L. Stehly, R. Brossier, A. Paul, and the AlpArray Working Group (2020). "Imaging Alpine crust using ambient noise wave-equation tomography". In: *Geophysical Journal International* 222.1, pp. 69–85. DOI: 10.1093/gji/ggaa145.

Malusà, M. G., S. Guillot, L. Zhao, A. Paul, S. Solarino, T. Dumont, S. Schwartz, C. Aubert, P. Baccheschi, E. Eva, Y. Lu, C. Lyu, S. Pondrelli, S. Salimbeni, W. Sun, and H. Yuan (2021). "The Deep Structure of the Alps Based on the CIFALPS Seismic Experiment: A Synthesis". In: *Geochemistry, Geophysics, Geosystems* 22.3, e2020GC009466. DOI: 10.1029/2020GC009466.

McBrearty, I. W., J. Gomberg, A. A. Delorey, and P. A. Johnson (2019). "Earthquake Arrival Association with Backprojection and Graph Theory". In: *Bulletin*

of the Seismological Society of America 109.6, pp. 2510–2531. ISSN: 1943-3573. DOI: 10.1785/0120190081.

Métois, M., N. D'Agostino, A. Avallone, N. Chamot-Rooke, A. Rabaute, L. Duni, N. Kuka, R. Koci, and I. Georgiev (2015). "Insights on continental collisional processes from GPS data: Dynamics of the peri-Adriatic belts". In: *Journal of Geophysical Research: Solid Earth* 120.12, pp. 8701–8719. ISSN: 2169-9356. DOI: 10.1002/2015jb012023.

Mey, J., D. Scherler, A. D. Wickert, D. L. Egholm, M. Tesauro, T. F. Schildgen, and M. R. Strecker (2016). "Glacial isostatic uplift of the European Alps". In: *Nature Communications* 7.1. ISSN: 2041-1723. DOI: 10.1038/ncomms13382.

Mitterbauer, U., M. Behm, E. Brückl, R. Lippitsch, A. Guterch, G. R. Keller, E. Koslovskaya, E.-M. Rumpfhuber, and F. Šumanovac (2011). "Shape and origin of the East-Alpine slab constrained by the ALPASS teleseismic model". In: *Tectonophysics* 510.1, pp. 195–206. DOI: 10.1016/j.tecto.2011.07.001.

Mousavi, S. M., S. P. Horton, C. A. Langston, and B. Samei (2016). "Seismic features and automatic discrimination of deep and shallow induced–microearthquakes using neural network and logistic regression". In: *Geophysical Journal International* 207.1, pp. 29–46. ISSN: 1365-246X. DOI: 10.1093/gji/ggw258.

Mroczek, S., F. Tilmann, J. Pleuger, X. Yuan, and B. Heit (2023). "Investigating the Eastern Alpine–Dinaric transition with teleseismic receiver functions: Evidence for subducted European crust". In: *Earth and Planetary Science Letters* 609, p. 118096. DOI: 10.1016/j.epsl.2023.118096.

Munafò, I., L. Malagnini, and L. Chiaraluce (2016). "On the Relationship between Mw and ML for Small Earthquakes". In: *Bulletin of the Seismological Society of America* 106, pp. 2402–2408. DOI: 10.1785/0120160130.

Nakanishi, I. and K. Yamaguchi (1986). "A numerical experiment on nonlinear image reconstruction from first-arrival times for two-dimensional island arc structure." In: *Journal of Physics of the Earth* 34.2, 195â–201. ISSN: 0022-3743. DOI: 10.4294/jpe1952.34.195.

Newman, M. E. J. (2006). "Modularity and community structure in networks". In: *Proceedings of the National Academy of Sciences* 103.23, pp. 8577–8582. DOI: 10.1073/pnas.0601602103.

Nicolas, A., A. Hirn, R. Nicolich, and R. Polino (1990). "Lithospheric wedging in the western Alps inferred from the ECORS-CROP traverse". In: *Geology* 18.7, p. 587. ISSN: 0091-7613. DOI: 10.1130/0091-7613(1990)018<0587:lwitwa>2.3.co;2.

Nicolas, M., N. Bethoux, and B. Madeddu (1998). "Instrumental Seismicity of the Western Alps: A Revised Catalogue". In: *Pure and Applied Geophysics* 152.4, pp. 707–731. ISSN: 1420-9136. DOI: 10.1007/s000240050173.

NOAA National Centers for Environmental Information (2022). *ETOPO 2022 15 Arc-Second Global Relief Model*. DOI: 10.25921/FD45-GT74.

Nouibat, A., L. Stehly, A. Paul, S. Schwartz, T. Bodin, T. Dumont, Y. Rolland, R. Brossier, C. Team, and AlpArray Working Group (2021). "Lithospheric transdimensional ambient-noise tomography of W-Europe: implications for crustal-

scale geometry of the W-Alps". In: *Geophysical Journal International* 229.2, pp. 862–879. DOI: 10.1093/gji/ggab520.

Okuta, R., Y. Unno, D. Nishino, S. Hido, and C. Loomis (2017). "CuPy: A NumPy-Compatible Library for NVIDIA GPU Calculations". In: *Proceedings of Workshop on Machine Learning Systems (LearningSys) in The Thirty-first Annual Conference on Neural Information Processing Systems (NIPS)*.

Paffrath, M., W. Friederich, S. M. Schmid, M. R. Handy, and the AlpArray and AlpArray Swath-D Working Group (2021). "Imaging structure and geometry of slabs in the greater Alpine area – a P-wave travel-time tomography using AlpArray Seismic Network data". In: *Solid Earth* 12.11, pp. 2671–2702. DOI: 10.5194/se-12-2671-2021.

Paul, A. (2022). "What we (possibly) know about the 3-D structure of crust and mantle beneath the Alpine chain". In: *HAL open science* hal-03747864.

Pedregosa, F., G. Varoquaux, A. Gramfort, V. Michel, B. Thirion, O. Grisel, M. Blondel, P. Prettenhofer, R. Weiss, V. Dubourg, J. Vanderplas, A. Passos, D. Cournapeau, M. Brucher, M. Perrot, and E. Duchesnay (2011). "Scikit-learn: Machine Learning in Python". In: *Journal of Machine Learning Research* 12, pp. 2825–2830.

Peruzza, L., M. Garbin, A. Snidarcig, M. Sugan, S. Urban, G. Renner, M. Romano, et al. (2015). "Quarry blasts, underwater explosions, and other dubious seismic events in NE Italy from 1977 to 2013". In: *Bollettino di Geofisica Teorica e Applicata* 56.4, pp. 437–459. DOI: 10.4430/bgta0159.

Petersen, G. M., S. Cesca, S. Heimann, P. Niemz, T. Dahm, D. Kühn, J. Kummerow, T. Plenefisch, and the AlpArray and AlpArray-Swath-D working groups (2021). "Regional centroid moment tensor inversion of small to moderate earthquakes in the Alps using the dense AlpArray seismic network: challenges and seismotectonic insights". In: *Solid Earth* 12.6, pp. 1233–1257. DOI: 10.5194/se-12-1233-2021.

Petersen, G. M., S. Cesca, M. Kriegerowski, and the AlpArray Working Group (2019). "Automated Quality Control for Large Seismic Networks: Implementation and Application to the AlpArray Seismic Network". In: *Seismological Research Letters* 90.3, pp. 1177–1190. DOI: 10.1785/0220180342.

Pfiffner, O. A., W. Frei, P. Valasek, M. Stäuble, L. Levato, L. DuBois, S. M. Schmid, and S. B. Smithson (1990). "Grustal shortening in the Alpine Orogen: Results from deep seismic reflection profiling in the eastern Swiss Alps, Line NFP 20-east". In: *Tectonics* 9.6, pp. 1327–1355. DOI: 10.1029/TC009i006p01327.

Phillips, J. D., W. Schwanghart, and T. Heckmann (2015). "Graph theory in the geosciences". In: *Earth-Science Reviews* 143, pp. 147–160. ISSN: 0012-8252. DOI: 10.1016/j.earscirev.2015.02.002.

Piromallo, C. and A. Morelli (2003). "P wave tomography of the mantle under the Alpine-Mediterranean area". In: *Journal of Geophysical Research: Solid Earth* 108.B2. DOI: 10.1029/2002JB001757.

Qorbani, E., D. Zigone, M. R. Handy, G. Bokelmann, and the AlpArray-EASI working group (2020). "Crustal structures beneath the Eastern and Southern Alps from ambient noise tomography". In: *Solid Earth* 11.5, pp. 1947–1968. DOI: 10.5194/se-11-1947-2020.

Ratschbacher, L., W. Frisch, F. Neubauer, S. M. Schmid, and J. Neugebauer (1989). "Extension in compressional orogenic belts: the eastern Alps". In: *Geology* 17.5, pp. 404–407. DOI: 10.1130/0091-7613(1989)017<0404:EICOBT>2.3.CO;2.

Reinecker, J. and W. A. Lenhardt (1999). "Present-day stress field and deformation in eastern Austria". In: *International Journal of Earth Sciences* 88, pp. 532–550. DOI: 10.1007/s005310050283.

Reiter, F., C. Freudenthaler, H. Hausmann, H. Ortner, W. Lenhardt, and R. Brandner (2018). "Active Seismotectonic Deformation in Front of the Dolomites Indenter, Eastern Alps". In: *Tectonics* 37.12, pp. 4625–4654. DOI: 10.1029/2017TC004867.

Reynen, A. and P. Audet (2017). "Supervised machine learning on a network scale: application to seismic event classification and detection". In: *Geophysical Journal International* 210.3, pp. 1394–1409. ISSN: 1365-246X. DOI: 10.1093/gji/ggx238.

Richter, C. F. (1935). "An instrumental earthquake magnitude scale". In: *Bulletin of the seismological society of America* 25.1, pp. 1–32. DOI: 10.1785/BSSA0250010001.

Romano, M. A., L. Peruzza, M. Garbin, E. Priolo, and V. Picotti (2019). "Microseismic Portrait of the Montello Thrust (Southeastern Alps, Italy) from a Dense High-Quality Seismic Network". In: *Seismological Research Letters* 90.4, pp. 1502–1517. DOI: 10.1785/0220180387.

Ross, Z. E., D. T. Trugman, E. Hauksson, and P. M. Shearer (2019). "Searching for hidden earthquakes in Southern California". In: *Science* 364.6442, pp. 767–771. DOI: 10.1126/science.aaw6888.

Rovida, A., M. Locati, R. Camassi, B. Lolli, P. Gasperini, and A. Antonucci (2022). *Italian Parametric Earthquake Catalogue (CPTI15), version 4.0*. Istituto Nazionale di Geofisica e Vulcanologia (INGV). DOI: 10.13127/cpti/cpti15.4.

Sadeghi-Bagherabadi, A., A. Vuan, A. Aoudia, S. Parolai, the AlpArray and AlpArray-Swath-D Working Group, B. Heit, M. Weber, C. Haberland, and F. Tilmann (2021). "High-Resolution Crustal S-wave Velocity Model and Moho Geometry Beneath the Southeastern Alps: New Insights From the SWATH-D Experiment". In: *Frontiers in Earth Science* 9. DOI: 10.3389/feart.2021.641113.

Sánchez, L., C. Völksen, A. Sokolov, H. Arenz, and F. Seitz (2018). "Present-day surface deformation of the Alpine region inferred from geodetic techniques". In: *Earth System Science Data* 10.3, pp. 1503–1526. ISSN: 1866-3516. DOI: 10.5194/essd-10-1503-2018.

Santulin, M., A. Rebez, M. Riuscetti, G. B. Carulli, S. Grimaz, F. Cucchi, and D. Slejko (2018). "The legacy of the 1976 Friuli earthquake". In: *Bollettino di Geofisica Teorica e Applicata*. ISSN: 0006-6729. DOI: 10.4430/bgta0228.

Saraò, A., M. Sugan, G. Bressan, G. Renner, and A. Restivo (2021). "A focal mechanism catalogue of earthquakes that occurred in the southeastern Alps and surrounding areas from 1928–2019". In: *Earth System Science Data* 13.5, pp. 2245–2258. DOI: 10.5194/essd-13-2245-2021.

Schlömer, A., J. Wassermann, W. Friederich, M. Korn, T. Meier, G. Rümpker, C. Thomas, F. Tilmann, and J. Ritter (2022). "UNIBRA/DSEBRA: The German Seismological Broadband Array and Its Contribution to AlpArray—Deployment and Performance". In: *Seismological Research Letters* 93.4, pp. 2077–2095. DOI: 10.1785/0220210287.

Schmid, S. M., D. Bernoulli, B. Fügenschuh, L. Matenco, S. Schefer, R. Schuster, M. Tischler, and K. Ustaszewski (2008). "The Alpine-Carpathian-Dinaridic orogenic system: correlation and evolution of tectonic units". In: *Swiss Journal of Geosciences* 101.1, pp. 139–183. ISSN: 1661-8734. DOI: 10.1007/s00015-008-1247-3.

Schmid, S. M., B. Fügenschuh, E. Kissling, and R. Schuster (2004). "Tectonic map and overall architecture of the Alpine orogen". In: *Eclogae Geologicae Helvetiae* 97.1, pp. 93–117. ISSN: 1420-9128. DOI: 10.1007/s00015-004-1113-x.

Scholz, C. H. (1968). "The frequency-magnitude relation of microfracturing in rock and its relation to earthquakes". In: *Bulletin of the Seismological Society of America* 58.1, pp. 399–415. ISSN: 0037-1106. DOI: 10.1785/bssa0580010399.

Scholz, C. H. (2015). "On the stress dependence of the earthquake b value". In: *Geophysical Research Letters* 42.5, pp. 1399–1402. ISSN: 1944-8007. DOI: 10.1002/2014gl062863.

Schorlemmer, D., S. Wiemer, and M. Wyss (2005). "Variations in earthquake-size distribution across different stress regimes". In: *Nature* 437.7058, pp. 539–542. ISSN: 1476-4687. DOI: 10.1038/nature04094.

Scotto di Uccio, F., A. Scala, G. Festa, M. Picozzi, and G. C. Beroza (2022). "Comparing and integrating artificial intelligence and similarity search detection techniques: application to seismic sequences in Southern Italy". In: *Geophysical Journal International* 233.2, pp. 861–874. ISSN: 1365-246X. DOI: 10.1093/gji/ggac487.

Serpelloni, E., G. Vannucci, L. Anderlini, and R. A. Bennett (2016). "Kinematics, seismotectonics and seismic potential of the eastern sector of the European Alps from GPS and seismic deformation data". In: *Tectonophysics* 688, pp. 157–181. DOI: 10.1016/j.tecto.2016.09.026.

Shang, X., X. Li, A. Morales-Esteban, and G. Chen (2017). "Improving microseismic event and quarry blast classification using Artificial Neural Networks based on Principal Component Analysis". In: *Soil Dynamics and Earthquake Engineering* 99, pp. 142–149. ISSN: 0267-7261. DOI: https://doi.org/10.1016/j.soildyn.2017.05.008.

Shearer, P. M. (1997). "Improving local earthquake locations using the L1 norm and waveform cross correlation: Application to the Whittier Narrows, California, aftershock sequence". In: *Journal of Geophysical Research: Solid Earth* 102.B4, pp. 8269–8283. DOI: 10.1029/96JB03228.

Sippl, C., B. Schurr, J. Münchmeyer, S. Barrientos, and O. Oncken (2023). "The Northern Chile forearc constrained by 15 years of permanent seismic monitoring". In: *Journal of South American Earth Sciences* 126, p. 104326. ISSN: 0895-9811. DOI: 10.1016/j.jsames.2023.104326.

Skoumal, R. J., M. R. Brudzinski, and B. S. Currie (2015). "Distinguishing induced seismicity from natural seismicity in Ohio: Demonstrating the utility of waveform template matching". In: *Journal of Geophysical Research: Solid Earth* 120.9, pp. 6284–6296. DOI: 10.1002/2015JB012265.

Slejko, D., L. Peruzza, and A. Rebez (1998). *Seismic hazard maps of Italy.*

Slejko, D. (2018). "What science remains of the 1976 Friuli earthquake?" In: *Bollettino di Geofisica Teorica ed Applicata* 59, pp. 327–350. DOI: 10.4430/bgta0224.

Spada, M., I. Bianchi, E. Kissling, N. P. Agostinetti, and S. Wiemer (2013). "Combining controlled-source seismology and receiver function information to derive 3-D Moho topography for Italy". In: *Geophysical Journal International* 194.2, pp. 1050–1068. DOI: 10.1093/gji/ggt148.

Swiss Seismological Service (SED) at ETH Zurich (1983). *National Seismic Networks of Switzerland.* DOI: 10.12686/sed/networks/ch.

TRANSALP Working Group, H. Gebrande, E. Lüschen, M. Bopp, F. Bleibinhaus, B. Lammerer, O. Oncken, M. Stiller, J. Kummerow, R. Kind, K. Millahn, H. Grassl, F. Neubauer, L. Bertelli, D. Borrini, R. Fantoni, C. Pessina, M. Sella, A. Castellarin, R. Nicolich, A. Mazzotti, and M. Bernabini (2002). "First deep seismic reflection images of the Eastern Alps reveal giant crustal wedges and transcrustal ramps". In: *Geophysical Research Letters* 29.10, p. 92. DOI: 10.1029/2002GL014911.

Ustaszewski, M. and O. A. Pfiffner (2008). "Neotectonic faulting, uplift and seismicity in the central and western Swiss Alps". In: *Geological Society, London, Special Publications* 298.1, pp. 231–249. DOI: 10.1144/SP298.12.

Van Rossum, G. and F. L. Drake Jr (1995). *Python tutorial.* Centrum voor Wiskunde en Informatica Amsterdam, The Netherlands.

Viganò, A., D. Scafidi, G. Ranalli, S. Martin, B. Della Vedova, and D. Spallarossa (2015). "Earthquake relocations, crustal rheology, and active deformation in the central–eastern Alps (N Italy)". In: *Tectonophysics* 661, pp. 81–98. DOI: 10.1016/j.tecto.2015.08.017.

Virtanen, P., R. Gommers, T. E. Oliphant, M. Haberland, T. Reddy, D. Cournapeau, E. Burovski, P. Peterson, W. Weckesser, J. Bright, S. J. van der Walt, M. Brett, J. Wilson, K. J. Millman, N. Mayorov, A. R. J. Nelson, E. Jones, R. Kern, E. Larson, C. J. Carey, İ. Polat, Y. Feng, E. W. Moore, J. VanderPlas, D. Laxalde, J. Perktold, R. Cimrman, I. Henriksen, E. A. Quintero, C. R. Harris, A. M. Archibald, A. H. Ribeiro, F. Pedregosa, P. van Mulbregt,

and SciPy 1.0 Contributors (2020). "SciPy 1.0: Fundamental Algorithms for Scientific Computing in Python". In: *Nature Methods* 17, pp. 261–272. DOI: 10.1038/s41592-019-0686-2.

Vuan, A., M. Sugan, G. Amati, and A. Kato (2018). "Improving the Detection of Low-Magnitude Seismicity Preceding the Mw 6.3 L'Aquila Earthquake: Development of a Scalable Code Based on the Cross Correlation of Template Earthquakes". In: *Bulletin of the Seismological Society of America* 108.1, pp. 471–480. DOI: 10.1785/0120170106.

Wiemer, S. and M. Baer (2000). "Mapping and Removing Quarry Blast Events from Seismicity Catalogs". In: *Bulletin of the Seismological Society of America* 90.2, pp. 525–530. ISSN: 0037-1106. DOI: 10.1785/0119990104. eprint: https://pubs.geoscienceworld.org/ssa/bssa/article-pdf/90/2/525/2710876/525_ssa99104.pdf.

Wiemer, S. and M. Wyss (2000). "Minimum magnitude of completeness in earthquake catalogs: Examples from Alaska, the western United States, and Japan". In: *Bulletin of the Seismological Society of America* 90.4, pp. 859–869. DOI: 10.1785/0119990114.

Withers, M., R. Aster, C. Young, J. Beiriger, M. Harris, S. Moore, and J. Trujillo (1998). "A comparison of select trigger algorithms for automated global seismic phase and event detection". In: *Bulletin of the Seismological Society of America* 88.1, pp. 95–106. DOI: 10.1785/BSSA0880010095.

Woollam, J., J. Münchmeyer, F. Tilmann, A. Rietbrock, D. Lange, T. Bornstein, T. Diehl, C. Giunchi, F. Haslinger, D. Jozinović, A. Michelini, J. Saul, and H. Soto (2022). "SeisBench—A Toolbox for Machine Learning in Seismology". In: *Seismological Research Letters* 93.3, pp. 1695–1709. ISSN: 1938-2057. DOI: 10.1785/0220210324.

ZAMG-Zentralanstalt Für Meterologie Und Geodynamik (1987). *Austrian Seismic Network*. DOI: 10.7914/SN/OE.

Zhao, L., A. Paul, S. Guillot, S. Solarino, M. G. Malusà, T. Zheng, C. Aubert, S. Salimbeni, T. Dumont, S. Schwartz, R. Zhu, and Q. Wang (2015). "First seismic evidence for continental subduction beneath the Western Alps". In: *Geology* 43.9, pp. 815–818. DOI: 10.1130/G36833.1.

Acknowledgements

Danksagung

I would like to express my deepest gratitude to Prof. Dr. Serge A. Shapiro for affording me the opportunity to write my PhD thesis at the Freie Universität Berlin. I greatly appreciate the support and guidance provided, as well the freedom entrusted to me to pursue my own interests. I am also very grateful to Prof. Dr. Frederik Tilmann for assuming the role of second reviewer for this thesis.

Very special thanks to Dr. Jörn Kummerow for his invaluable guidance, insightful discussions, and constructive feedback throughout the course of my research. His mentorship and support were instrumental. Also thanks to our other project members, especially Simone and Gesa for the many helpful project meetings.

This research was funded by the Deutsche Forschungsgemeinschaft (DFG, German Research Foundation) – project numbers KU 2484/5-1 and KU 2484/5-2.

Thanks to all colleagues from our department: Nepomuk, Stine, William, Cornelius, Mohammad, Jörg, and Christian, as well as all former colleagues and students. Last but not least, special thanks to my colleague and friend, Jonas, for both the scientific endeavours in our shared office, and the non-scientific endeavours outside of our office.

Many thanks to the AlpArray community for facilitating this research, and for the many well organised conferences, which were always very inspiring and motivating. A special thanks to Ben Heit for the memorable times during the field deployment of the Swath-D network. This was a great experience in many ways.

I am grateful to my parents for teaching me to love nature and the mountains. I am also very thankful to my dear sister, and to all friends and family, both in the Utrecht and in Berlin, for their support.

Finally, most special thanks to my wife Lisa and to my daughter Lana. You have been the greatest support and inspiration. Thank you for the wonderful time we have had together. I look forward to all the things that are still to come.

Curriculum Vitae

Work Experience

Freie Universität Berlin, Berlin (Germany) **11/2017 – 04/2024**

Research Assistant in the Geophysics department

- deployment of seismic stations over multiple field trips in the Alps
- detection and location of low-magnitude seismicity in the Eastern Alps
- development of high-performance GPU codes for waveform processing
- teaching of Python programming course and administration of exercise server

Ludwig-Maximilians-Universität, München (Germany) **01/2017 – 07/2017**

Erasmus Trainee at the Geophysical Observatory

Continuous deformation monitoring in seismically active areas of Bavaria using seismic background noise

- investigation of earthquake swarms in the Hochstaufen range, Bavaria
- calculation and analysis of temporal variation in seismic noise correlations
- correlation of changes in velocity structure to hydrological processes

Royal Dutch Meteorological Institute (KNMI), de Bilt (Netherlands) **03/2016 – 08/2016**

Research intern for MSc project

A shallow seismic velocity model for the Groningen area in the Netherlands

- calculation of instrument corrections and borehole geophone orientations
- development of a shallow seismic velocity model by seismic interferometry

Royal Dutch Meteorological Institute (KNMI), de Bilt (Netherlands) **03/2014 – 10/2016**

Research assistant at ORFEUS Data Center

- data processing and quality control
- development and improvement of web tools and services
- database management

Education

Freie Universität Berlin, Berlin (Germany) **11/2017 – present**

PhD in SPP programme Mountain Building Processes in 4 Dimensions

PhD thesis: *Detection and analysis of seismicity in the Eastern Alps using waveform based methods*

Universiteit Utrecht, Utrecht (Netherlands) **02/2015 – 07/2017**

Master Earth Structure and Dynamics, Faculty of Geosciences

MSc thesis: *A shallow seismic velocity model for the Groningen area in the Netherlands*

- combined tracks geology + geophysics
- additional Erasmus+ traineeship at LMU München

Universiteit Utrecht, Utrecht (Netherlands) **09/2011 – 01/2015**

Bachelor Earth Sciences, Faculty of Geosciences

BSc thesis: *Comparison of the checkerboard test and spike test to assess the quality of tomographic inversions*

- combined tracks solid earth geology + earth dynamics
- additional courses in physics and computer science

Field Experience

Expedition Summit Station (Greenland) **08/2019**

Maintenance of GEOFON station SUMG on Summit research station — 2 weeks

Deployment of the AlpArray Swath-D network **09/2017 – 03/2018**

Installation of seismic stations in the Eastern Alps — 13 weeks total

Excursion Mt. Hochstaufen (Germany) **05/2017**

Maintenance seismic station Staufenhaus (RTSH) — 1 day

Excursion Tabernas desert, Andalusia (Spain) **05/2015 – 06/2015**

Geological fieldwork — 8 weeks

Excursion Pyrenees (Spain) **05/2013 – 06/2013**

Geological fieldwork — 6 weeks

Computer Skills

programming, parallell computing, GPU computing, machine-learning, database handling, web-development, system administration

Programming languages: Python, Matlab, FORTRAN90, Bash, Perl C#, LaTeX
Python-packages: NumPy, SciPy, SKlearn, ObsPy, Pyrocko, MSNoise, CuPy, Pandas, ...
Web-development: HTML, CSS, JavaScript, PHP
Other software: ArcGIS, SQL, Office

Languages

Dutch: Native
English: Fluent
German: Fluent
French: Intermediate

Publications and Conference Abstracts

Folesky, J., Pennington, C.N., Kummerow, J., and **Hofman, L.J.** (2024). A comprehensive stress drop map from trench to depth in the northern Chilean subduction zone. Journal of Geophysical Research: Solid Earth, 129, e2023JB027549. DOI: 10.1029/2023JB027549

Hofman, L. J., Kummerow, J., Cesca, S., and the AlpArray–Swath-D Working Group (2023). A new seismicity catalogue of the eastern Alps using the temporary Swath-D network, Solid Earth, 14, 1053–1066, DOI: 10.5194/se-14-1053-2023

Hofman, L. J., Kummerow, J., Cesca, S., and the AlpArray-Swath-D Working Group. (2023). Seismicity catalogue for the Eastern Alps (Swath-D), GFZ Data Services [data set]. DOI: 10.5880/fidgeo.2023.024

Hofman, R., Petersen, G., Kummerow, J., and Cesca, S. and the The AlpArray Swath-D Working Group (2024). Seismicity clusters in the Eastern Alps: New insights from the large-N Swath-D seismic network. EGU General Assembly 2024, Vienna, Austria, 14–19 Apr 2024, EGU24-16584. DOI: 10.5194/egusphere-egu24-16584, 2024.

Petersen, G., **Hofman, L.J.**, Cesca, S., Kummerow, J., Plenefisch, T., and Wassermann, J. (2023). Seismotectonics of the Eastern Alps: New insights from earthquake studies within 4D-MB. AlpArray & 4D-MB SPP Meeting Bad Hofgastein, Austria. DOI: 10.17169/refubium-41070

Hofman, R., Kummerow, J., Petersen, G., and Cesca, S. (2023). Waveform based cluster analysis of seismicity in the Eastern Alps. XXVIII General Assembly of the International Union of Geodesy and Geophysics (IUGG), Berlin, Germany. DOI: 10.57757/IUGG23-3596.

Petersen, G.M., Cesca, S., **Hofman, R.**, and Kummerow, J. (2023). Shedding light on the rupture mechanism of small earthquakes in the Alps and Dinarides: Stacked-waveform MT Inversion. XXVIII General Assembly of the International Union of Geodesy and Geophysics (IUGG), Berlin, Germany. DOI: 10.57757/IUGG23-2463

Folesky, J., Kummerow, J., and **Hofman, R.** (2023). Repeating earthquakes in Northern Chile, from true repeaters to deep repeaters. XXVIII General Assembly of the International Union of Geodesy and Geophysics (IUGG), Berlin, Germany. DOI: 10.57757/IUGG23-3201

Hofman, R., Kummerow, J., and Cesca, S. and the AlpArray Working Group (2023). Spatial and Temporal Patterns in Eastern-Alpine Seismicity. EGU General Assembly 2023, Vienna, Austria, 24–28 Apr 2023, EGU23-12921. DOI: 10.5194/egusphere-egu23-12921

Folesky, J., **Hofman, R.**, and Kummerow, J. (2023). Stress Drop Segmentation in the Northern Chilean Subduction Zone: from Interface to Deep Seismicity. EGU General Assembly 2023, Vienna, Austria, 24–28 Apr 2023, EGU23-8901. DOI: 10.5194/egusphere-egu23-8901

Hofman, L.J., Kummerow, J., Cesca, S., Wassermann, J., Plenefisch, T., and the AlpArray Working Group (2022). Distribution of Seismicity in the Eastern Alps Using Swath-D. AlpArray Scientific Meeting, Prague, Czech Republic.

Hofman, R., Kummerow, J., Cesca, S., Wassermann, J., and Plenefisch, T. and the AlpArray Working Group (2022). Distribution of Active Seismic Deformation in the Eastern Alps from the Recent Swath-D Experiment. EGU General Assembly 2022, Vienna, Austria, 23–27 May 2022. EGU22-11358, DOI: 10.5194/egusphere-egu22-11358

Folesky, J., **Hofman, R.**, and Kummerow, J. (2022). On Repeating Earthquakes in the Northern Chilean Subduction Zone. EGU General Assembly 2022, Vienna, Austria, 23–27 May 2022, EGU22-7316. DOI: 10.5194/egusphere-egu22-7316

Hofman, L.J., Kummerow, J., Cesca, S., Wassermann, J., Plenefisch, T., and the AlpArray Working Group (2021). Seismicity in the Eastern Alps: Preliminary Results From the Swath-D Network. AlpArray & 4DMB Scientific Meeting, online.

Hofman, R., Kummerow, J., Cesca, S., Wassermann, J., and Plenefisch, T. and the AlpArray Working Group (2021). Microseismicity in the Eastern Alps: Preliminary Results From the Swath-D Network. EGU General Assembly 2021, online, 19–30 Apr 2021, EGU21-9829. DOI: 10.5194/egusphere-egu21-9829

Folesky, J., **Hofman, R.**, and Kummerow, J. (2021). Stress Drops from Trench to Depth in the Northern Chilean Subduction Zone. EGU General Assembly 2021, online, 19–30 Apr 2021, EGU21-16514. DOI: 10.5194/egusphere-egu21-16514

Hofman, L.J., Kummerow, J., Cesca, S., Wassermann, J., Plenefisch, T., and the AlpArray Working Group (2020). Local Seismicity Patterns in the Eastern Alps. Joint AlpArray & 4D-MB SPP Meeting 2020, online.

Hofman, R., Kummerow, J., Cesca, S., Wassermann, J., and Plenefisch, T. and the AlpArray Working Group (2020). Local Seismicity in the Eastern Alps From GPU-Based Template Matching. EGU General Assembly 2020, Online, 4–8 May 2020, EGU2020-18781. DOI: 10.5194/egusphere-egu2020-18781

Hofman, L.J., Kummerow, J., Cesca, S., Wassermann, J., Plenefisch, T. (2019) Microseismic Event Detection in the Eastern Alps (Swath-D). Joint AlpArray & 4D-MB SPP Meeting, Frankfurt, Germany.

Hofman, L.J., Petersen, G., Kummerow, J., Cesca, S., Wassermann, J., Plenefisch, T. (2019). From Top to Bottom- Seismicity, Motion Patterns & Stress Distribution in the Alpine Crust. AlpArrayCollaborative Meeting, Trieste, Italy.

Hofman, R., Kummerow, J., Cesca, S., Wassermann, J., Plenefisch, T. (2019). Spatial and Temporal Patterns in Microseismicity in the Eastern Alps. EGU General Assembly 2019, Vienna, Austria. Geophysical Research Abstracts Vol. 21, EGU2019-11122.

Hofman, L.J., Kummerow, J., Cesca, S., Wassermann, J., Plenefisch, T. (2018). Seismicity, Motion Patterns and Stress Distribution in the Alpine Crust: Detecting Microseismicity in the Eastern Alps Using the Swath-D Network. Annual 4D-MB SPP Meeting 2018. Frankfurt, Germany.

Hofman, L.J., Kummerow, J., Cesca, S., Wassermann, J., Plenefisch, T. (2018) Detecting Microseismicity in the Eastern Alps using the Swath-D Network. EGU General Assembly 2018, Vienna, Austria. Geophysical Research Abstracts Vol. 20, EGU2018-7693.